Generation of harmonic radiation in self-guided filaments in gaseous media

Von der Fakultät für Mathematik und Physik
der Gottfried Wilhelm Leibniz Universität Hannover
zur Erlangung des Grades

Doktor der Naturwissenschaften

- Dr. rer. nat. -

genehmigte Dissertation

von

Dipl.-Phys. Tobias Vockerodt

geboren am 14.10.1982 in Hannover

2012

Abstract

Tobias Vockerodt

Generation of harmonic radiation in self-guided filaments in gaseous media

The peak intensity of ultrashort laser pulses today reaches the *strong-field regime* without difficulty, i.e. a local electric field strength that significantly influences the atomic potential. As a result, many non-linear effects manifest themselves in laser pulse propagation, such as plasma-channel formation and self-guiding inside a filament. Such a filament consists of a hot white-light core and a surrounding reservoir.

In this work, filaments of a femtosecond laser pulse are tracked along their propagation axis. Due to truncation of the filament by use of one or several pinholes and removal of the non-linear medium and reservoir, access is gained to pulse properties otherwise unreachable because of high intensity in the hot core.

Inside a filament, third-order harmonic generation occurs, which is greatly enhanced by the truncation method. The spectral evolution of this radiation along the filament's propagation is analysed with respect to formation of a short ultraviolet pulse. A transient grating frequency-resolved optical gating device is developed, capable to characterise few-femtosecond pulses in spectral ranges from infrared to ultraviolet.

Additionally, extreme ultraviolet radiation is emitted by a filament. Generation of high-order harmonics directly inside filaments in air, argon and neon is detected. Due to its strongly non-linear dependence on intensity, high-order harmonic radiation is used as a probe to the on-axis intensity inside a filament, a value otherwise inaccessible.

As an application of coherent extreme ultraviolet radiation, diffraction imaging of nanometric structures is used. Since this imaging technique requires a high photon flux, experiments have been conducted at a beamline of the *Laserlab Europe* network. By recording diffraction patterns from different angles, a three-dimensional image of the object is reconstructed via iterative phase retrieval.

Key words: Strong-field regime, self-guiding, filamentation, third-order harmonic generation (THG), high-order harmonic generation (HHG), transient grating frequency resolved optical gating (TG-FROG), coherent diffraction imaging (CDI)

Kurzfassung

Tobias Vockerodt

Erzeugung harmonischer Strahlung in selbstgeführten Filamenten in gasförmigen Medien

Die Spitzenintensität ultrakurzer Laserimpulse erreicht heute problemlos das *Starkfeld-Regime*, d. h. ein lokales elektrisches Feld, welches ein Atompotential signifikant beeinflusst. In der Folge manifestieren sich zahlreiche nichtlineare Effekte bei der Propagation eines intensiven Laserimpulses, wie z. B. Plasmakanalformung und Selbstführung in einem Filament. Ein solches Filament besteht aus einem intensiven Weißlichtkern und einem umgebenden Reservoir.

Im Rahmen dieser Arbeit werden Filamente eines Femtosekunden-Laserimpulses entlang ihrer Propagationsrichtung untersucht. Durch Abschneiden des Filaments mit Hilfe einer oder mehrerer Lochblenden und Entfernung des nichtlinearen Mediums und des Reservoirs ist der Zugang zu Eigenschaften der Strahlung innerhalb des Weißlichtkerns möglich, der andernfalls durch zu hohe Intensität verhindert wird.

Innerhalb des Filaments entsteht die dritte Harmonische der Laserstrahlung. Der Prozess wird durch die Abschneide-Methodik erheblich verstärkt. Die spektrale Evolution dieser Strahlung wird entlang der Filamentpropagation mit besonderem Augenmerk auf die Erzeugung eines Ultraviolett-Laserimpulses analysiert. Eine Messapparatur, die in der Lage ist, Laserimpulse mit Dauern weniger Femtosekunden im infraroten bis ultravioletten Wellenlängenbereich zu analysieren, wird entwickelt.

Ferner emittiert ein Filament extrem ultraviolette Strahlung, die auf die Erzeugung hoher Harmonischer zurückzuführen ist. Diese Strahlung wird in Filamenten in Luft, Argon und Neon nachgewiesen und untersucht. Durch die hohe Nichtlinearität dieses Prozesses kann er als Indikator für die auf anderem Wege unzugängliche Intensität im Filament verwendet werden.

Als Anwendung kohärenter, extrem ultravioletter Strahlung dient die Diffraktions-Mikroskopie an nanometrischen Strukturen. Da dieses Abbildungsverfahren einen großen Photonenfluss benötigt, finden die Experimente an einer Strahlquelle des *Laserlab Europe*-Netzwerkes statt. Durch die Aufnahme von Beugungsbildern aus verschiedenen Winkeln wird ein drei-dimensionales Realbild rekonstruiert.

Schlagwörter: Starkfeld-Regime, Selbstführung, Filamentation, Erzeugung dritter Harmonischer (THG), Erzeugung hoher Harmonischer (HHG), transient grating frequency resolved optical gating (TG-FROG), Diffraktions-Mikroskopie (CDI)

Contents

Abbreviations

Notation	Description
2PP	two-photon polymerisation
ADK	AMMOSOV, DELONE and KRAINOV
APT	attosecond pulse train
ATI	above-threshold ionisation
BK7	borosilicate glass
CaF_2	calcium fluoride
CDI	coherent diffraction imaging
CEA	Commissariat à l'énergie atomique et aux énergies alternatives
CEP	carrier-envelope offset phase
DCM	double-chirped mirror
DFWM	degenerated four-wave mixing
DSLR	digital single-lens reflex
FFT	fast fourier transform
FIB	focussed ion beam
FLASH	free-electron laser in Hamburg
FROG	frequency-resolved optical gating
FWHM	full width at half maximum
FWM	four-wave mixing
GHIO	guided hybrid input-output
HHG	high-order harmonic generation
HIO	hybrid input-output
HOKE	higher order KERR effect
IAP	isolated attosecond pulse
IS	intensity spike
LLG	Laser-Laboratorium Göttingen e. V.
LZH	Laser Zentrum Hannover e. V.
MPI	multiphoton ionisation
NIR	near infrared
OTBI	over-the-barrier ionisation
PG	polarisation gating
PID	proportional integral derivative
PPT	PERELOMOV, POPOV and TERENT'EV
SD	self-diffraction
SHG	second harmonic generation
Si_3N_4	silicon nitride
SIGC	semi-infinite gas cell
SPAM	Service des Photons, Atomes et Molécules

Notation	Description
SPIDER	spectral phase interferometry for direct electric-field reconstruction
SPM	self-phase modulation
TDSE	time-dependent SCHRÖDINGER equation
TG	transient grating
TG-FROG	transient grating frequency-resolved optical gating
THG	third harmonic generation
TOF	time-of-flight
UV	ultraviolet
VIS	visible
XUV	extreme ultraviolet

1

Introduction

Studying the interaction of matter with intense laser fields has provided numerous interesting phenomena, such as self-phase modulation, generation of coherent and incoherent extreme ultraviolet radiation as well as x-rays and pulses with sub-femtosecond duration. Within this interaction, non-linear effects act on both, matter and laser field. These studies have been made possible by development of ultrafast laser amplifiers, providing laser pulses in the *strong-field* regime, which, when focused, generate electric field strengths above that of inner-atomic binding fields ($\sim 5 \cdot 10^{11}\,\text{V/m}$), resulting in laser-induced non-linear ionisation.

When weakly focused into a suitable non-linear medium, i.e. a noble gas, a powerful laser pulse will self-focus up to the point of plasma generation. In proper conditions, a dynamic equilibrium between self-focusing and plasma-induced defocusing is established, leading to self-guiding of the laser pulse in a plasma channel. Such a *filament* persists over a distance significantly larger than the RAYLEIGH length, from 50 cm up to several kilometres. The pulse energy is confined within a narrow core, in which white light is generated due to self-phase modulation and plasma generation. It is surrounded by a *reservoir* of fundamental light, co-propagating and interacting with the white light core.

A precise look into the dynamics of a filament is limited. Any measurement equipment is either destroyed due to high intensity damage, or likely to modify the laser pulse properties significantly. This work utilises a newly developed technique to truncate a filament at a specific position during its self-guided propagation. Removing the reservoir and the non-linear medium ensures undisturbed linear propagation from the point of truncation to the detection and opens a view to spectral and temporal evolution of laser pulses inside a filament.

Filaments emit radiation in many ranges of the electromagnetic spectrum, such as ultraviolet, the complete visible spectrum, infrared and even terahertz radiation. In this work, generation of ultraviolet radiation by means of third-order harmonic generation is revealed with enhanced on-axis conversion efficiency and unprecedented beam profile quality. The spectral width of this emission is large enough to form a 5 fs pulse centred at ultraviolet wavelengths. Furthermore, high-order harmonic generation is observed inside filaments in air, argon and neon. Absorption after short propagation distances prevented these effects from showing up in previous studies. Being highly non-linear, the generation process contains valuable information on the on-axis intensity, inaccessible by conventional measurement techniques. We identify the dynamic formation of spikes in intensity as the origin of high-order harmonic generation and enhanced ultraviolet spectral broadening. These spikes originate from off-axis pulse parts undergoing spatio-temporal refocusing cycles and exceed the filament's clamping intensity.

Due to a short single cycle duration of the electric field at ultraviolet (UV) wavelength, broadband third harmonic generation (THG) prospects generation of a sub-femtosecond pulse. However, only low order non-linear effects are involved, resulting in high photon numbers compared to conventional single attosecond pulse generation (see Section 2.6.2 for details). Analysis of the temporal structure of UV radiation emerging from a filament and its subsequent compression is, therefore, of high scientific relevance. For temporal characterisation of the visible and ultraviolet output of a filament, we develop a pulse measurement device based on a four-wave mixing process included in a frequency-resolved optical gating set-up. This guarantees ultraviolet compatibility down to 180 nm and an ability to resolve few-femtosecond pulses. A compression scheme for this radiation requires control of higher order dispersion and is discussed as well.

As an application of laser-generated coherent extreme ultraviolet (XUV) radiation, we use a lens-less microscopy technique, namely *coherent diffraction imaging*. Harmonic radiation generates diffraction patterns from a sample with nanometre-sized structures, which are used to iteratively reconstruct a real image via phase-retrieval. In the scope of this work, several types of samples are developed for this imaging method to be able to obtain a three-dimensional real image. Diffraction patterns are generated and image reconstruction is done, supported by national (Laser Zentrum Hannover e. V.) and international cooperation (*Laserlab Europe* network).

Organisation of this Thesis

This document is organised as follows. In Chapter 2 I present some background to the work described in the later chapters, especially a discussion of filamentation's basic principles and the processes involved, as well as historical progress on this topic. Selected applications of filamentation and high-order harmonic generation are discussed as well. In Chapter 3 I describe the experimental approach to filamentation analysis along the propagation axis, as well as the results obtained in the visible, ultraviolet and extreme ultraviolet part of the electromagnetic spectrum. Chapter 4 is a discussion of the temporal characterisation set-up as well as the underlying physical processes and the results obtained with this set-up. This chapter also includes a brief discussion on ultraviolet pulse compression. In Chapter 5, I describe experiments and results concerning coherent diffraction imaging, including the design and fabrication of three-dimensional samples and real image reconstruction. In Chapter 6, I will conclude the work presented, and finally, in Chapter 7, I will give an outlook on possible future work and work currently in progress.

2

Basic Principles

Laser filamentation describes the phenomenon of an intense laser pulse guiding itself inside a non-linear medium. A filament is formed if the beam is confined in a small spatial area for significantly longer distances than its RAYLEIGH length. Depending on laser parameters and the used medium, filaments can reach lengths of centimetres to metres [Bra95; Cou07]. In atmospheric experimental studies, ranges of several kilometres have been realised [Wös97; Rod04; Méc04; Méc05].

This chapter describes laser pulses used for filamentation as well as principal effects involved in it, i.e. non-linear ionisation in Section 2.1 and electrooptic effects in Section 2.2. A dynamic balance between these processes leads to self-guiding and filamentation and their theoretical description as presented in Section 2.3. Other non-linear effects can occur inside a filament, in particular harmonic generation, which is discussed in Section 2.4. Section 2.5 describes a method to characterise ultrashort pulses before, inside and after the filament. Selected applications of filamentation and high-order harmonic radiation are summarised in Section 2.6.

Ultrashort laser pulses

Within this work, the following notations are used. An electric field E describing an ultrashort laser pulse is given by

$$E(z,t) = E_0(z,t)\,e^{i(\omega t - kz + \phi_{CE})} = E_0(z,t)\,e^{i\phi(z,t)} \tag{2.1}$$

where z is the propagation coordinate, $k = \frac{2\pi n}{\lambda}$ the wavenumber, E_0 the pulse envelope and the carrier-envelope offset phase (CEP) is denoted ϕ_{CE}. The time dependence of the

exponential term is summarised in a temporal phase $\phi(z,t)$. Spatial dimensions concerning the laser beam in x and y directions are not considered at this point. The instantaneous frequency of the pulse carrier wave is then given by

$$\omega(z,t) = -\frac{\partial}{\partial t}\phi(z,t). \tag{2.2}$$

For sufficiently high input pulse energy and low pulse duration, high-field effects are acting on the instantaneous frequency. At an intensity above $1 \cdot 10^{13}$ W/cm^2, an incident laser pulse centred at $\lambda = 780$ nm even starts to ionise transparent media such as noble gases.

2.1 Non-linear Photo-Ionisation

If a single photon with the energy $\hbar\omega$ exceeds the ionisation threshold of an atom, it can be absorbed and the atom is ionised. The absorption rate is linear in the number of photons. For a photon energy smaller than this threshold and far from any atomic resonance, the medium appears transparent and linear absorption is not possible.

However, high-power laser systems deliver ultrashort laser pulses sufficiently intense to ionise otherwise transparent media. This is achieved by the simultaneous absorption of several photons exceeding the ionisation threshold, which is called multiphoton ionisation (MPI) and is sketched in figure 2.1(a). An intensity above $1 \cdot 10^{13}$ W/cm^2 is needed to observe such an effect in e.g. a noble gas. Further increase in intensity leads to absorption of more photons than necessary for ionisation. In this case of above-threshold ionisation (ATI), all ionised fragments carry additional kinetic energy, visible as peaks in electron time-of-flight
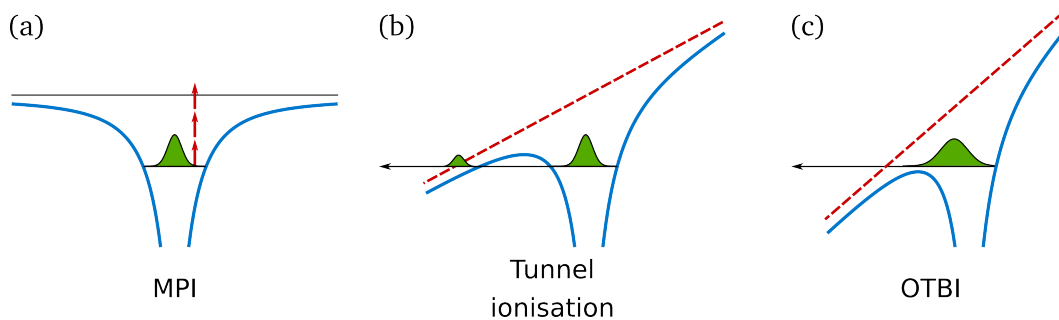

Figure 2.1: Ionisation of atoms by **(a)** multiphoton ionisation, **(b)** tunnel ionisation and **(c)** over-the-barrier ionisation. Blue solid lines represent the atomic potential, red dashed lines display the external electric field. The horizontal black line in (a) shows the atomic ionisation threshold.

(TOF) spectroscopy [Ebe91; Fre91]. If the electric field strength of the laser pulse reaches the regime of inner-atomic fields, the electron's binding potential is deformed by the laser field and tunnel ionisation is the main ionisation channel, as depicted in figure 2.1(b) [Pro97]. Even further increase in field strength can lower the binding potential of the atom in such a way, that the electron is ionised without tunneling. Figure 2.1(c) shows this scenario of over-the-barrier ionisation (OTBI).

2.1.1 Theory of Non-linear Ionisation

The concepts of multiphoton and tunnel ionisation are descriptions of the same physical phenomenon under different limits, namely the ratio of photon energy and ionisation energy on one hand and laser field strength and binding field strength on the other hand. A brief overview of the three theories most commonly used in literature to describe the ionisation probability is given in the following. More detailed descriptions can be found in the appendix in chapter A.

Keldysh Theory

A primary theory of photo-ionisation in strong fields is the general KELDYSH theory [Kel65]. Given that the tunnelling time τ of an electron through the barrier of a coulomb potential is small compared to the changing of the electric field, the tunnel effect is determined by the instantaneous electric field value. KELDYSH introduces an adiabaticity parameter γ, called the KELDYSH parameter, which is the ratio of the electric field oscillation period to the electron tunnelling time.

The resulting expression for the ionisation rate w is

$$w = A\omega \cdot \left(\frac{I_{\mathrm{P}}}{\hbar\omega}\right)^{3/2} \cdot \left(\frac{\gamma}{\sqrt{1+\gamma^2}}\right)^{5/2} S\left(\gamma, \frac{I_\omega}{\hbar\omega}\right)$$
$$\cdot \exp\left(-\frac{2I_\omega}{\hbar\omega}\left(\mathrm{arsinh}(\gamma) - \gamma \cdot \frac{\sqrt{1+\gamma^2}}{1+2\gamma^2}\right)\right), \quad (2.3)$$

where I_{P} and I_ω respectively denote the atomic and effective ionisation potential. Details of the atomic species are incorporated in the numerical factor A in equation (2.3), which often serves as a fitting parameter. The KELDYSH parameter is often used to discriminate between

tunnel ionisation and MPI. Such an interpretation needs to be tested carefully, as the physical process in both cases is essentially the same, and typical properties for experiments, e.g. high-order harmonic generation, often lead to values for γ in the order of one.

PPT Theory

PERELOMOV, POPOV and TERENT'EV (PPT) improved the general KELDYSH theory by taking atomic details [Per66] and Coulomb interaction [Per67] into account. Ionisation rates calculated numerically by PPT theory show a very good agreement with experimental data [Lar98]. This calculation method is therefore well-established and often used in literature. An expression for the ionisation rate is the following:

$$
w_{\mathrm{PPT}}(E,\omega) = \frac{I_{\mathrm{P}}}{\hbar} \left| C_{n^*,\ell^*} \right|^2 \sqrt{\frac{6}{\pi}} \cdot f(\ell,m) \left(1+\gamma^2\right)^{n^*} \left(\frac{2E_0}{E}\sqrt{1+\gamma^2}\right)^{2n^*-|m|-3/2}
$$
$$
\cdot A_m(\omega,\gamma) \cdot \exp\left(-\frac{2E_0}{3E}\cdot g(\gamma)\right) \quad , \quad (2.4)
$$

for a bound electronic state with quantum numbers n, ℓ and m. Details are given in appendix A.

ADK Theory

In contrast to KELDYSH and PPT theories, the approach developed by AMMOSOV, DELONE and KRAINOV (ADK) [Amm86] concentrates on tunnel ionisation of a complex atom in an arbitrary state. ADK theory eliminates the remaining free parameter from the expressions of photo-ionisation from KELDYSH and PPT theories. It is often used, because its explicit form for the ionisation rate w is easily implemented:

$$
w_{\mathrm{ADK}}(E) = \frac{I_{\mathrm{P}}}{\hbar} \left| C_{n^*\ell^*} \right|^2 \sqrt{\frac{6}{\pi}} f(\ell,m) \left(\frac{2E_0}{E}\right)^{2n^*-|m|-3/2} \exp\left(-\frac{2E_0}{3E}\right) , \quad (2.5)
$$

However, omitting the influence of MPI, calculations are only valid for sufficiently high field strengths.

2.1.2 Ionisation Rates

All three theoretical approaches enable us to calculate ionisation rates. Equation (2.5) from ADK theory and equation (2.4) from PPT result in averaged rates over one oscillation period of the electric field. Instantaneous values are accessible by division of equation (2.5) by $\sqrt{3E/(\pi E_0)}$ in case of ADK theory (for details, see eq. (7) in [Per66]). In the other two cases, the only results are non-adiabatic ionisation rates [Yud01; Pop08].

In figure 2.2, ionisation rates have been calculated according to KELDYSH, PPT and ADK theory at a wavelength of 780 nm. Values originating from KELDYSH theory lack the coefficient A (see also appendix A). Tunnel ionisation is dominating in the high intensity regime reaching $1 \cdot 10^{16}\,\mathrm{W/cm^2}$. Therefore, the parameter A as been determined to fit the KELDYSH curves to the others at high intensities. Fitting values for A are 40, 30 and 15 for helium, neon and argon respectively.

Clearly visible in figure 2.2 is the underestimation of the ionisation rate when using ADK theory. Since it only includes tunnel ionisation, it is inaccurate in the multiphoton-dominated intensity regime below $5 \cdot 10^{14}\,\mathrm{W/cm^2}$.

Numerical models for filamentation include non-linear ionisation by either one or a combination of several of the mentioned theories. ADK theory has the advantage of easy implementation and calculation but suffers from inaccuracy in the multi-photon regime.
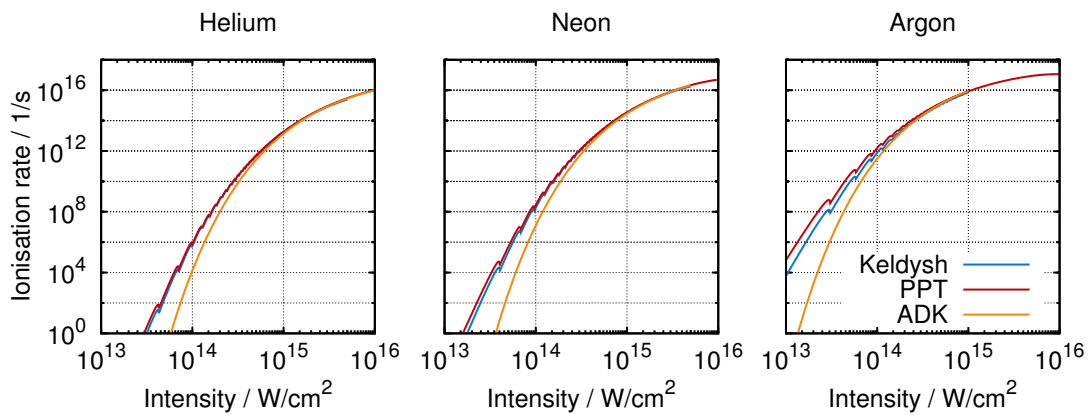

Figure 2.2: Calculated ionisation rates from three different theoretical approaches [Kel65; Per66; Amm86] for the noble gases helium (left), neon (center) and argon (right). The curves from the KELDYSH theory have been fitted with the parameter A using values 40 (helium), 30 (neon) and 15 (argon).

A disadvantage of the KELDYSH theory is the free parameter A, impeding *ab initio* calculations. Since this limitation is resolved by PPT theory and a good experimental agreement is reported in literature [Lar98], it is widely used and highly recommendable.

2.2 Kerr Effect

The presence of an electric field changes the optical properties of transparent media. A linear change of refractive index is known as the POCKELS effect, which is dependent on the medium's anisotropy. In isotropic media such as gases, liquids and centrosymmetric crystals, the linear electrooptic coefficient is zero. Instead, the refractive index is subjected to the KERR effect, a quadratic dependence on electric field strengths. [Trä07]

Considering a laser beam with an intensity profile $I(\mathbf{x}, t)$, the KERR effect can be expressed as

$$n\big(I(\mathbf{x}, t)\big) = n_0 + n_2 I(\mathbf{x}, t),\tag{2.6}$$

where n_0 and n_2 respectively are the linear and non-linear refractive indices. n_2 is related to the third-order susceptibility $\chi^{(3)}$,

$$n_2 = \frac{3\chi^{(3)}}{4\varepsilon_0 c n_0^2}\tag{2.7}$$

From the intensity's spatial and temporal dependence, two major consequences of the KERR effect arise, namely self-focusing and self-phase modulation, discussed in the following sections.

Values for n_2 in this work are calculated according to [Leh85], accounting for pressure and temperature of a gas. Calculated values for noble gases and nitrogen at 1 bar are given in table 2.1.

Table 2.1: Non-linear refractive indices for noble gases and nitrogen, calculated as described in [Leh85]. Parameters are $\lambda_{\text{centre}} = 795\,\text{nm}$, $p = 1\,\text{bar}$ and $\vartheta = 20\,°\text{C}$.

He	Ne	Ar	Kr	Xe	N$_2$	
$3.77 \cdot 10^{-12}$	$6.75 \cdot 10^{-21}$	$9.14 \cdot 10^{-20}$	$2.54 \cdot 10^{-19}$	$7.69 \cdot 10^{-19}$	$8.20 \cdot 10^{-20}$	$\frac{\text{cm}^2}{\text{W}}$

2.2.1 Self-Focusing

Equation (2.6) couples the spatial intensity distribution to a refractive index modulation. As n_2 is usually positive, a Gaussian intensity profile results in an index profile similar to a focusing lens, as shown in figure 2.3. Therefore, the spatial aspect of the KERR effect is *self-focusing* of an intense laser beam through a *Kerr-lens*.

Self-focusing does only appear, if the KERR effect overcomes natural diffraction, which is always acting on a laser beam [Cou07]. For instance, the width of a Gaussian beam with flat spatial phase propagating in vacuum will increase by a factor of $\sqrt{2}$ after propagating the distance L_R,

$$L_\mathrm{R} = \frac{\pi n_0 w_0^2}{\lambda_0}, \tag{2.8}$$

which is the RAYLEIGH length. Here, λ_0 denotes the vacuum laser wavelength and w_0 is the beam waist, i.e. the radius at which the electric field strength's absolute square drops to $1/e^2$ of the peak value. For a 780 nm beam with $w_0 = 100\,\mu\mathrm{m}$ in vacuum, the RAYLEIGH length is 40 mm.

The characteristic length for self-focusing L_sf is defined as a function of the peak intensity I_peak:

$$L_\mathrm{sf} = \frac{\lambda_0}{2\pi n_2 I_\mathrm{peak}}. \tag{2.9}$$

However, the significant parameter for self-focusing is not the initial intensity of the beam,
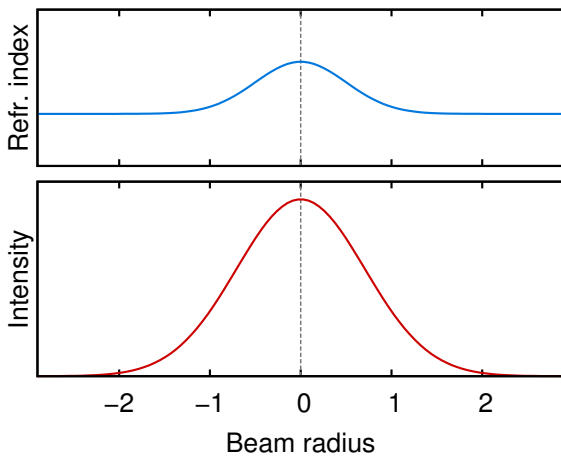

Figure 2.3: A Gaussian intensity distribution induces a change in the refractive index due to the KERR effect. The intensity distribution along the radial coordinate is shown in the lower part of the figure. Depicted in the upper part is the resulting index profile, which is similar to a focusing lens. Both ordinate axes have arbitrary units.

but rather the input peak power P_{in}, which has to exceed the *critical power* P_{cr} for self-focusing to appear. It differs from the combination of equations 2.8 and 2.9 only by a numerical form factor [Mar75]:

$$P_{\text{cr}} = 3.72 \cdot \frac{\lambda_0^2}{8\pi n_0 n_2} \, . \tag{2.10}$$

The validity of equation (2.10) is limited to a specific beam shape (the TOWNES beam [Chi64]), for which diffraction and self-focusing are balanced [Cou07]. For other shapes the critical power is usually larger, although equation (2.10) is a good estimate [Fib00]. A semi-empirical formula for the propagation length L_{c} of a beam until it collapses is given by DAWES and MARBURGER [Daw69]:

$$L_{\text{c}} = 0.367 \cdot L_{\text{Rayleigh}} \left[\left(\sqrt{P_{\text{in}}/P_{\text{cr}}} - 0.852 \right)^2 - 0.0219 \right]^{-1/2} \tag{2.11}$$

The expression breaks down for input powers of the order of $100\,P_{\text{cr}}$ or higher. At this point, modulational instabilities, i.e. imperfections of the beam profile, lead to formation of hot spots and multiple filaments. [Cou07]

2.2.2 Self-Phase Modulation

When we consider an intense laser pulse, the intensity is also varying in time and induces a temporal change in the refractive index. In the laser pulse description in equation (2.1), the time dependent index of refraction appears in the temporal phase $\phi(z,t) = \omega t - k \cdot n(t) \cdot z$.
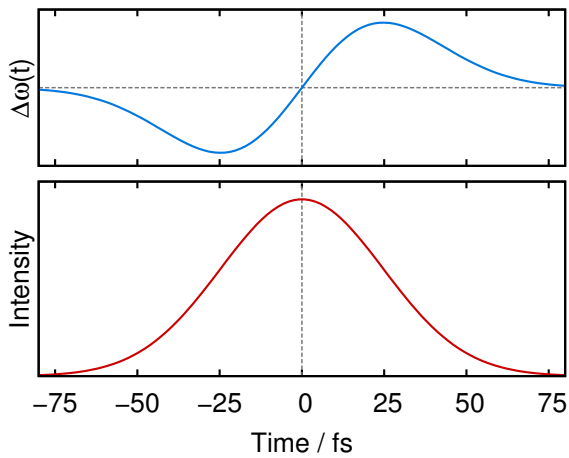

Figure 2.4: A refractive index varying in time affects the instantaneous frequency of the electric field. The lower graph shows the intensity profile of a Gaussian laser pulse in time. In the upper graph, the difference of the instantaneous frequency is depicted. Both ordinate axes have arbitrary units.

As a result, the instantaneous frequency is now given by

$$\omega_{\mathrm{SPM}}(t) = \omega - \frac{\omega n_2 z}{c} \frac{\partial}{\partial t} I(z,t).$$

(2.12)

Figure 2.4 depicts the change in instantaneous frequency $\Delta\omega(t)$ due to the temporal KERR effect, called self-phase modulation (SPM). While the leading edge of the pulse encounters a red-shifting of its frequency, the trailing edge is blue-shifted. This generates new frequencies at the edges of the pulse spectrum with a characteristic modulation. The frequency generation depends on the slope $\partial I / \partial t$ of the pulse. [Trä07; Rob06; Cou07]

SPM is the main source of spectral broadening in filamentation and therefore responsible for its primary application.

2.2.3 Higher Order Kerr Effect

Equation (2.6) is a series expansion of n up to the quadratic order in $I = |E|^2$ with the coefficient n_2. The following terms, corresponding to the higher order susceptibilities $\chi^{(j)}$, are usually omitted due to their minor influence.

In 2009, LORIOT *et al.* performed measurements of the non-linear refractive index n_2 using 90 fs, 800 nm laser pulses [Lor09; Lor10]. The experiments show deviations from previous results [Nib97] and are interpreted as experimental evidence of higher order $n(I)$ terms, that can be quantified via fitting of the measurement signal with an expansion of the non-linear KERR index of refraction,

$$\Delta n_{\mathrm{Kerr}} = n_2 I + n_4 I^2 + n_6 I^3 + n_8 I^4 + n_{10} I^5,$$
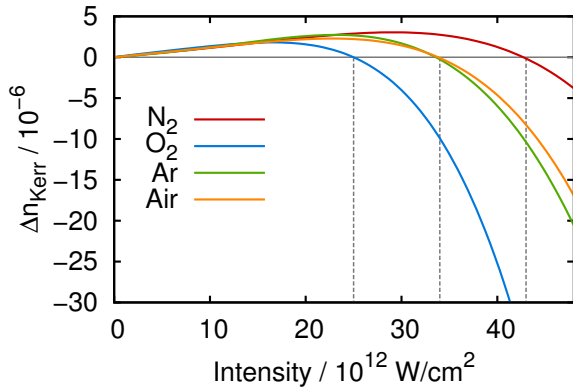
(2.13)

Figure 2.5: Intensity dependence of the non-linear index of refraction according to [Lor10]. For intensities above $10\,\mathrm{TW/cm^2}$, saturation and sign inversion of the Kerr effect is quantified. The curves show the refractive index variation according to equation (2.13) with values listed in table 2.2.

Table 2.2: Measured values for the higher order KERR coefficients for the gases N_2, O_2, Ar and Air. Measurement conditions have been 100 mbar pressure at room temperature [Lor10].

n_j		N_2	O_2	Ar	Air
n_2	$10^{-7}\,\mathrm{cm}^2/\mathrm{TW}$	1.1 ± 0.2	1.60 ± 0.35	1.00 ± 0.09	1.2 ± 0.3
n_4	$10^{-9}\,\mathrm{cm}^4/\mathrm{TW}^2$	-0.53 ± 0.26	-5.16 ± 0.53	-0.36 ± 1.03	-1.5 ± 3.0
n_6	$10^{-10}\,\mathrm{cm}^6/\mathrm{TW}^3$	1.40 ± 0.15	4.75 ± 0.50	4.0 ± 0.5	2.10 ± 0.22
n_8	$10^{-11}\,\mathrm{cm}^8/\mathrm{TW}^4$	-0.44 ± 0.04	-2.10 ± 0.14	-1.72 ± 0.10	-0.80 ± 0.06
n_{10}	$10^{-14}\,\mathrm{cm}^{10}/\mathrm{TW}^5$	–	–	8.83 ± 0.50	–

where n_j are the non-linear KERR coefficients and I denotes the laser intensity. The retrieved values of n_j are presented in table 2.2. These findings are named the higher order KERR effect (HOKE).

Implications for the physical process of filamentation arise from the saturation and sign change of $n(I)$ with increasing intensity. The role of HOKE for filamentation as well as the controversial debate flaring up about it are discussed in Section 2.3.3.

2.3 Filamentation

Guiding of laser pulses by a refractive index profile in gaseous media has been realised in 1993 by DURFEE and MILCHBERG [Dur93]. By creating a plasma induced refractive index channel in air with a strong laser pulse, guiding of a second, counter-propagating pulse has been observed. Two years later, BRAUN *et al.* showed the first self-guiding of a femtosecond laser pulse in a filament, reaching lengths of 20 m in which the pulse remains contained in a small spatial area. A background energy reservoir surrounding the plasma channel as well as conical emission from the filament have been observed, although both are not yet investigated in detail. [Bra95; Cou07]

Later, NIBBERING *et al.* formulated filamentation as a leaky waveguide consisting of 'a weakly ionised core surrounded by Kerr cladding'. Taking into account the surrounding energy reservoir and being able to explain the conical emission observed previously, the *self-guiding model* emerged (see Section 2.3.1). [Nib96]

However, this static model neglects all effects that occur on a laser pulse timescale. Inspired by numerical calculations, the dynamic spatial replenishment model describes the dynamics inside filaments as shown in Section 2.3.2.

A currently controversial discussion is inspired by the HOKE (Section 2.2.3), opening the possibility of ionisation-free filamentation by saturation of KERR self-focusing. This topic is discussed in Section 2.3.3.

2.3.1 Self-Guiding Model

The formation of a filament is accounted to self-focusing (see section 2.2.1), occurring when the critical power (equation (2.10)) is exceeded. For a stable guiding mechanism, the quadratic KERR effect needs a counteracting effect, preventing the beam from collapsing into an optical breakdown.

In the self-guiding model, the onset of plasma formation is stabilising the laser pulse propagation. Due to self-focusing, the on-axis intensity reaches the threshold for non-linear ionisation and generates free charges. The refractive index n_{el} due to free electrons is [Bra95; LHu91]

$$n_{el} = \sqrt{1 - \frac{\omega_p^2}{\omega^2}} \quad \text{and} \quad \omega_p = \frac{e^2}{m_e \cdot \varepsilon_0} \cdot N_e(I), \quad (2.14)$$

with the plasma frequency ω_p and the plasma density $N_e(I)$. From the spatial intensity profile, a refractive index profile is formed in the same way as a KERR lens, but with an opposite sign. Consequently, this leads to *plasma defocusing*. According to BRAUN *et al.*, stable filamentation of a femtosecond laser pulse is attributed to a balance between self-focusing and plasma-induced defocusing, as sketched in figure 2.6. In contrast to a widespread view of the self-guiding model, BRAUN *et al.* do not assume this balance to be dynamic [Bra95]. The surrounding energy reservoir of non-filamented light counteracts losses by natural diffraction and multiphoton absorption [Nib96]. It is a vital part of the filament and should
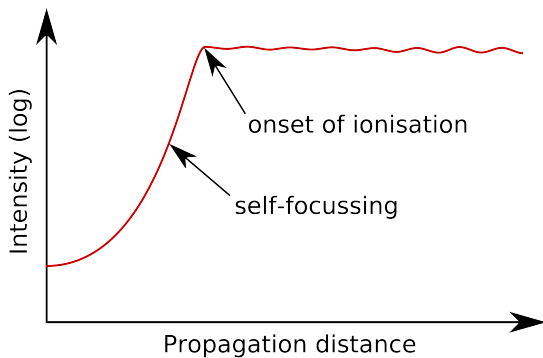

Figure 2.6: Simplified sketch of the on-axis intensity according to the first proposal of the self-guiding model by BRAUN *et al.*. After a steep raise due to self-focusing, the onset of plasma generation results in intensity clamping. [Bra95]

not be understood as a loss mechanism itself. As a result, the intensity inside the filament is clamped to a value near the ionisation threshold, which cannot be exceeded.

However, a direct measurement of the on-axis intensity and its evolution inside a filament has not been performed. Access to this value is very limited due to technical limitations at high intensities. CHIN *et al.* propose to compare the fluorescence of two nitrogen lines at 337 nm and 391 nm, which increase with laser intensity at different orders of non-linearity [Xu12]. The experiments presented in this work grant access to the on-axis intensity via harmonic generation processes (see Chapter 3).

2.3.2 Dynamic Spatial Replenishment Model

The self-guiding picture is very intuitive and simple, but static at the same time. To understand the involved dynamics, numerical simulations performed by MLEJNEK *et al.* in 1998 include self-focusing, multiphoton absorption, group-velocity dispersion and plasma defocusing. In the dynamic picture, the leading edge of the pulse is self-focused and generates a plasma tail behind. The trailing part of the pulse is defocused by this plasma while the leading peak intensity is decreased by multiphoton absorption. Due to the intensity decrease, plasma generation is reduced, raising the influence of self-focusing again. The model emerging from these simulations shows absorption of parts of the laser pulse and its subsequent replenishment by new pulses [Mle98]. Figure 2.7 displays a simplified sketch of this model of *dynamic spatial replenishment*, omitting the temporal aspect for the sake of clarity. MLEJNEK *et al.* encourage the view that the balance between focusing and defocusing consists of dynamic spikes in both intensity and plasma formation, leading to re-focusing cycles occurring aperiodically along the filament. These spikes can exceed the clamping intensity and overcome the threshold for high-order harmonic generation [Gaa09; Ste11b]. They will be discussed in detail in Section 2.4.3. [Cou07]
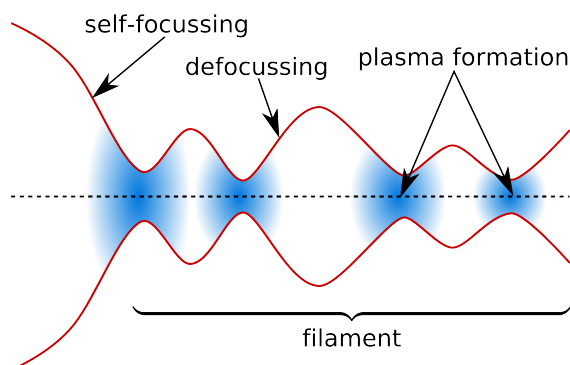

Figure 2.7: Simplified sketch of an extended filamentation model. The trailing part of the pulse experiences defocusing due to plasma generated from the leading edge of the pulse. Such dynamics lead to aperiodic refocusing cycles inside the filament.

2.3.3 Ionisation-Free Filamentation

The role of ionisation in the formation of filaments is discussed periodically in the history of filamentation, although, until recently, there was no alternative defocusing mechanism. First estimations of ionisation rates appear to mismatch with measured values by orders of magnitude [Kas00]. In 2004, a long-range filamentation regime is observed, in which only a minimum of ionisation is involved [Méc04]. The intensity in the filament core is below the MPI threshold, and nevertheless, the energy is confined to a small spatial area for ranges of kilometres. Studies by STIBENZ *et al.* reveal, that if a balance between self-focusing and plasma contribution is responsible for filamentation, it implies a strongly asymmetric pulse shape [Sti06]. Absence of asymmetry in experimental data suggests a minor role of ionisation.

Measurements presented in Section 2.2.3 contain measured values for the higher-order non-linear index of refraction [Lor09; Lor10; Lor11]. Since some of the values are negative, the change in the non-linear refractive index experiences a saturation and an inversion at high intensities. With these values, new filamentation calculations are performed, including the HOKE into the existing models. As a result, self-focusing can be counteracted by the saturation of the KERR effect, expressed in terms of the HOKE [Béj10]. Depending on the parameters, ionisation is still present, but it is not required under all circumstances. This revision of already widely accepted models caused a considerable amount of controversy [Köh12; Kol10b; Kol10a; Che10; Bré11; Béj11b; Kos11; Bor12; Kol12].

BÉJOT *et al.* interpreted experimental findings from 2011 as two distinguishable regimes of filamentation [Béj11a]. The measurement method is a pump-probe filamentation setup with a pulse separation of one and two picoseconds, being below the plasma recombination time. For pulses in the order of a picosecond duration, plasma induces a significant portion of defocusing, whereas ultrashort pulses of 70 fs are found to propagate with negligible plasma effect. Current studies conclude on one hand that HOKE has only a minor role even for ultra-short input pulses [Köh12]. On the other hand, experimental observations from four-wave mixing (FWM) experiments are well explained by HOKE-based theory [Bor12]. Ionisation-free filamentation therefore remains a topic of research and the role of HOKE is uncertain until further investigation.

2.4 Principles of Harmonic Generation

Generation of optical harmonics is known almost since the invention of the laser 1960 [Mai60]. By frequency conversion of fundamental laser light to its second harmonic, FRANKEN *et al.* called the research field of *non-linear optics* to existence [Fra61]. The laser field induced polarisation $\mathscr{P}$ is developed in terms of the electric field, resulting in a power series,

$$\mathscr{P} = \varepsilon_0 \chi^{(1)} E + \mathscr{P}_{\mathrm{nl}} = \varepsilon_0 \left(\chi^{(1)} E + \chi^{(2)} E^2 + \chi^{(3)} E^3 + \ldots \right) , \qquad (2.15)$$

with the non-linear polarisation $\mathscr{P}_{\mathrm{nl}}$ and the non-linear susceptibilities $\chi^{(j)}$. From equation (2.15), an electric field can be calculated for different orders of non-linearity, showing a broad variety of frequency-mixing effects, among which are second harmonic generation (SHG), THG [War69], parametric down-conversion, stimulated RAMAN scattering and SPM [Trä07]. In general, the order of the non-linear process has a strong influence on the conversion efficiency, described by perturbation theory.

The available laser peak power has increased and the number and order of non-linear effects has grown ever since. In 1987, high-order harmonic generation (HHG) has been observed for the first time [McP87; Fer88]. HHG features a plateau of harmonic orders with comparable conversion efficiency, an effect which cannot be explained in terms of perturbation theory. This highly non-perturbative process results in spatially and temporally coherent radiation in the XUV and soft x-ray region, extending to shorter and shorter wavelengths [Mac93; Pre96; Cha97; Spi97]. An intuitive semi-classical model of high-order harmonic generation is presented in Section 2.4.1. For an exact calculation, a time-consuming numerical solution of the time-dependent SCHRÖDINGER equation (TDSE) is usually used. To circumvent this extensive task, a quantum-mechanical description by the LEWENSTEIN model is given in Section 2.4.2.

2.4.1 Three Step Model of High-Order Harmonic Generation

A simple and semi-classical model for HHG is the *three step model* by CORKUM [Cor93]. It describes the response of a single atom to a strong laser field. While the laser field itself and a free electron inside is handled in a classical way, the atom is described quantum-mechanically. The process is divided into three steps, depicted in figure 2.8(a).
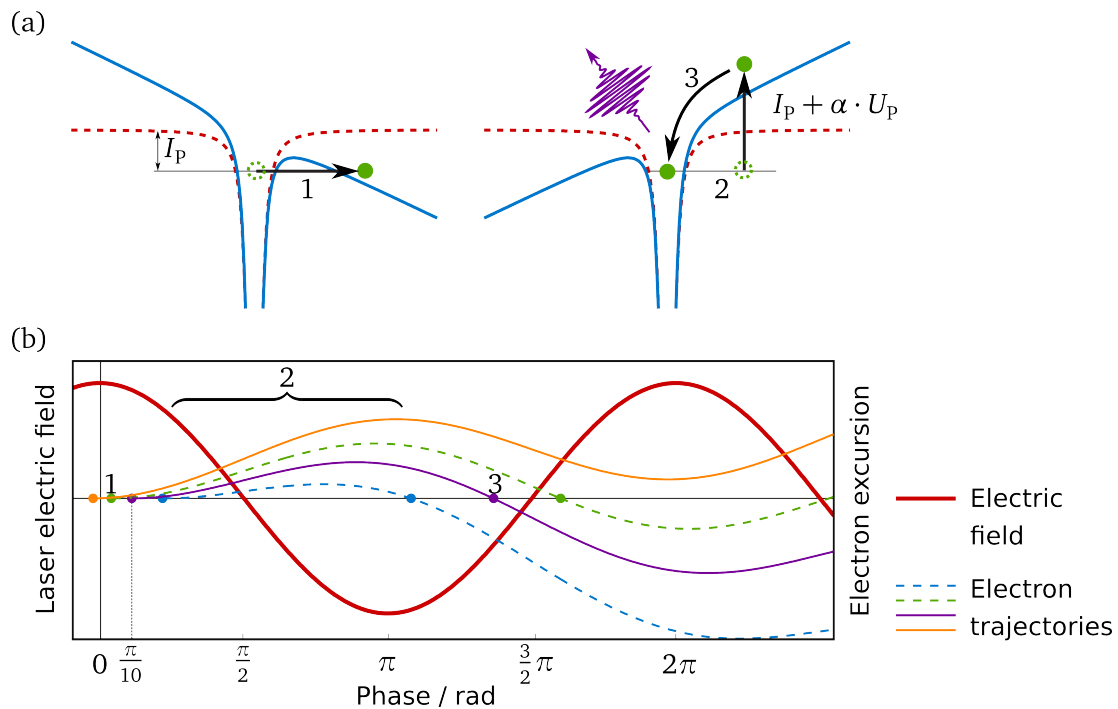
(a)

(b)

Figure 2.8: The three step model by CORKUM [Cor93]. **(a)** left: in step 1, the bound electron tunnels through the binding potential (blue line) which is bend due to the electric field. Right: the alternating field accelerates the electron (step 2). Upon re-collision with the residual ion, the kinetic energy $\alpha \cdot U_P$ plus the ionisation potential I_p is released as a photon (step 3). **(b)** electric field (red thick line) and electronic trajectories (thin solid and dashed lines). The violet line represents a trajectory with the maximum kinetic energy, released at a phase of $\pi/10$ of the laser field. Marked by the blue and green dashed line, respectively, is the short and long trajectory. The orange line depicts the trajectory of a non-returning electron. The three steps from (a) are noted at the corresponding phases.

At first, an electron is excited to the continuum via tunnel ionisation. The probability for this process is dependent on the laser field strength and therefore varies with the phase of the field (see Section 2.1). In figure 2.8(b), the birth and excursion of a free electron is marked for four different times near phase zero, which is a field maximum with highest ionisation probability.

The electric field accelerates the free electron, adding kinetic energy. To keep the model simple, the residual ion's static electric field is neglected. The electron's kinetic energy is expressed in terms of the average kinetic energy or ponderomotive potential U_P (equation A.3).

After a quarter of an optical cycle, the electric field changes its direction, reversing the electron's acceleration. It is driven back to its origin and has a non-vanishing probability to re-collide with the ion. In case of a recombination, the total energy $\hbar\omega = I_p + \alpha \cdot U_P$
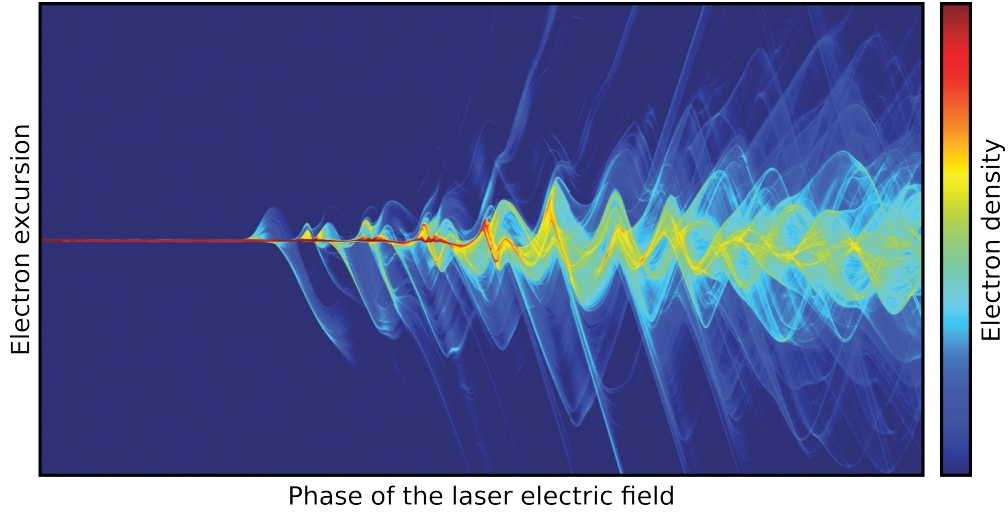
Figure 2.9: Electron density calculations in case of HHG from a thin metal foil target (by LOCH [Loc09]). The electrons ejected with the corresponding ionisation probability evolve on classical trajectories. The logarithmic color scale denotes a high (red) to low (blue) electron density.

consisting of the ionisation potential and the electron's kinetic energy, is released in form of a photon. The emission can be calculated from the expectation value of the dipole operator $\hat{d} = e\hat{r}$, which is oscillating at high frequencies. The maximum photon energy emitted by this oscillating dipole determines the end of the non-perturbative plateau region. It is estimated by

$$E_{\mathrm{max}} = 3.17 \cdot U_{\mathrm{p}} + I_{\mathrm{p}} \, . \tag{2.16}$$

$\alpha = 3.17$ is a value directly calculated from the electronic movement and is associated with an electron released at an electric field phase of $\pi/10$ (see the violet trajectory in figure 2.8(b)). Both earlier and later released electrons have a smaller re-collision energy. The earlier one (dashed green line) takes a longer time to return to the ion and has therefore been named the long trajectory. The blue dashed line belongs to an electron ionised at a later time, also known as the short trajectory. A calculation of trajectories can be seen in figure 2.9.

Returning after less than an optical cycle, the re-colliding electrons cause a series of harmonic radiation bursts with a half-cycle periodicity. These APTs are sketched in figure 2.10(a) and (b) for multi-cycle driving pulses. If the driving pulse contains only few electric field oscillations (see fig. 2.10(c)), high photon energies stem exclusively from the field maximum. High-energy filtering can extract an IAP from the output as figure 2.10(d) displays. Further details of HHG for attosecond pulse generation are described in Section 2.6.
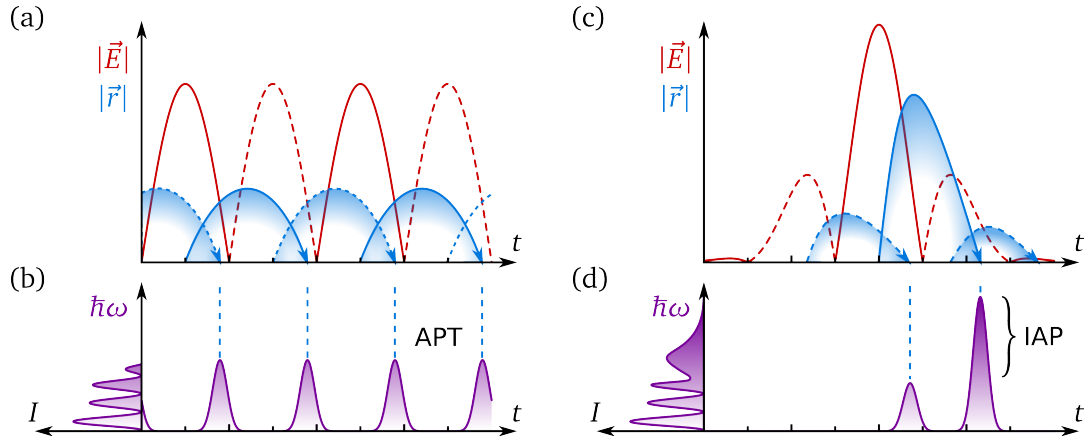
Figure 2.10: HHG in case of multi- and few-cycle driving pulses. Electric field oscillations (red lines) and corresponding electron excursions (blue line) are depicted in (a), (c), harmonic intensity spectra and time-resolved emission are sketched in (b), (d). **(a)** Electrons are accelerated and re-collide every half optical cycle. **(b)** This results in regular bursts of harmonic radiation, an APT (right) and a modulated harmonic spectrum (left). **(c)** In case of few cycle driving pulses, the field maximum changes on a sub-cycle time scale. **(d)** From the most intense cycle, a continuum is created in the high energy part (left) containing an IAP (right).

2.4.2 Lewenstein Model

The LEWENSTEIN model describes the HHG process in a quantum-mechanical manner. Although it is less time-consuming than a direct solution of the TDSE, it sill includes effects such as quantum diffusion and quantum interference, which are absent in the semi-classical model. The description given here follows [Lew94].

In the HHG intensity regime, ionisation is dominated by tunnel ionisation and OTBI. For the validity of the LEWENSTEIN model, it is assumed that time evolution of the system depends only on the electronic ground state and is independent of any other electronic bound states. Furthermore, depletion of the electronic ground state as well as the potential of the residual ion is neglected.

The TDSE for the electron in length gauge[1]:

$$\mathrm{i}\frac{\partial}{\partial t}\left|\psi(t)\right\rangle = \left(-\frac{1}{2}\nabla^2 + V(\mathbf{x}) - E\cdot\cos(t)\,x\right)\left|\psi(t)\right\rangle . \tag{2.17}$$

---

1   Throughout the quantum-mechanical model, atomic units $\hbar = 1$, $m_\mathrm{e} = 1$, $e = 1$ are used. Additionally, frequencies are taken in units of the laser frequency $\omega_0 = 1$.

The time-dependent electronic wave function $\psi(t)$ is

$$\left|\psi(t)\right\rangle = e^{iI_p t}\left(a(t)\left|0\right\rangle + \int d^3\mathbf{v}\, b(\mathbf{v},t)\left|\mathbf{v}\right\rangle\right),\tag{2.18}$$

with the electronic ground state $\left|0\right\rangle$, its amplitude $a(t)$ and the continuum states $\left|\mathbf{v}\right\rangle$ with their amplitudes $b(\mathbf{v},t)$ discriminated by the kinetic energy of the corresponding ejected electrons. This yields the SCHRÖDINGER equation in velocity gauge:

$$i\frac{\partial}{\partial t}\left|\psi(t)\right\rangle = \left[-\frac{\mathbf{v}^2}{2} - E\cdot\cos(t)\cdot i\frac{\partial}{\partial v_x}\right]\left|\psi(t)\right\rangle,\tag{2.19}$$

from which the SCHRÖDINGER equation of the amplitudes can be deduced:

$$\left\langle\mathbf{v}\right|i\frac{\partial}{\partial t}\left|\psi(t)\right\rangle = \left\langle\mathbf{v}\right|\left[-\frac{\mathbf{v}^2}{2} - E\cdot\cos(t)\cdot i\frac{\partial}{\partial v_x}\right]\left|\psi(t)\right\rangle\tag{2.20}$$

$$\Rightarrow\quad \dot{b}(\mathbf{v},t) = -i\left(\frac{\mathbf{v}^2}{2} + I_p\right)b(\mathbf{v},t) - E\cos(t)\frac{\partial b(\mathbf{v},t)}{\partial v_x} + iE\cos(t)d_x(\mathbf{v})\tag{2.21}$$

Here, $i\partial/\partial v_x = \mathbf{x}$ is the position operator in velocity gauge. The ground state amplitude $a(t) = 1$ is set to unity according to the assumption of negligible depopulation. The atomic dipole matrix element for a transition from bound to continuum states $\mathbf{d}(\mathbf{v}) = \left\langle\mathbf{v}\right|\mathbf{x}\left|0\right\rangle$ has a part $d_x(\mathbf{v}) = \left\langle\mathbf{v}\right|i\frac{\partial}{\partial v_x}\left|0\right\rangle$ parallel to the polarisation axis of the laser field.

Equation (2.21) is now solvable and can be expressed in a closed from:

$$b(\mathbf{v},t) = i\int_0^t dt'\left[E\cos(t')d_x(\mathbf{v}+\mathbf{A}(t)-\mathbf{A}(t'))\right.$$

$$\left.\cdot\exp\left[-i\int_{t'}^t dt''\left((\mathbf{v}+\mathbf{A}(t)-\mathbf{A}(t''))^2/2 + I_p\right)\right]\right].\tag{2.22}$$

Here, $\mathbf{A}(t) = (-E\sin(t),0,0)$ is the laser field vector potential. When the time-dependent dipole moment is expressed in terms of equations (2.18) and (2.22), we gain access to the component $x(t)$ of the dipole moment.

$$x(t) = \left\langle\psi(t)\right|x\left|\psi(t)\right\rangle \approx \int d^3\mathbf{v}\, d_x^*(\mathbf{v})\, b(\mathbf{v},t) + \text{c.c.}\tag{2.23}$$

At this point, continuum-continuum transitions are neglected. With the canonical impulse $\mathbf{p} = \mathbf{v} + \mathbf{A}(t)$, a physically meaningful expression is gained:

$$x(t) = \mathrm{i} \int_0^t \mathrm{d}t' \int \mathrm{d}^3\mathbf{p}\, E \cos(t')\, d_x\big(\mathbf{p} - \mathbf{A}(t')\big) \exp\big(-\mathrm{i}S(\mathbf{p},t,t')\big)\, d_x^*(\mathbf{p} - \mathbf{A}(t)) + \mathrm{c.c.} \quad (2.24)$$

Here, $S(\mathbf{p},t,t')$ is the quasi-classical action,

$$S(\mathbf{p},t,t') = \int_{t'}^t \mathrm{d}t'' \left(\frac{(\mathbf{p} - \mathbf{A}(t''))^2}{2} + I_\mathrm{p} \right) . \qquad (2.25)$$

Equation (2.24) can be understood as a sum of probability amplitudes for different processes. The first term of the integrand, $E\cos(t')\,d_x(\mathbf{p} - \mathbf{A}(t'))$, describes the excitation of an electron to the continuum at time t' with the canonical impulse $\mathbf{p}$. Subsequently, the electronic wave packet propagates until time t, accumulating the phase $-\mathrm{i}S(\mathbf{p},t,t')$ of a free electron in a laser field with a constant canonical impulse. The probability amplitude for recombination of the electron at time t is given by the last term $d_x^*(\mathbf{p} - \mathbf{A}(t))$.

Furthermore, substantial contributions of the $\mathbf{p}$-integral in equation (2.24) stem from stationary points of the quasi-classical action (2.25) [Bal97], which means that $\nabla_\mathbf{p} S(\mathbf{p},t,t') = 0$ Considering the difference of the locations $\mathbf{r}(t)$ and $\mathbf{r}(t')$ of the electron at times t and t', one gains

$$\mathbf{r}(t) - \mathbf{r}(t') = \nabla_\mathbf{p} S(\mathbf{p},t,t') \quad . \qquad (2.26)$$

Consequently, stationary points of S are associated with those impulses $\mathbf{p}$, at which the electron excited at t' returns to exactly the same location at time t. Hereby, the LEWENSTEIN model justifies the essential assumption of the semi-classical model, that only electrons returning to their parent ion contribute to HHG. Additionally, the mainly contributing electrons have initial velocities near to zero.

Considering the Fourier components of equation (2.24) shows that even terms cancel out due to the central symmetry of atomic gases. As a result, only odd harmonic orders are included in HHG spectra.

In contrast to the semi-classical model, the electron's maximum kinetic energy is diffuse due to a non-vanishing size of the electronic wave packet. Although the factor $\alpha = 3.17$ is the

same as in the three step model, there is an additional correction factor F depending on the ratio $I_\mathrm{p}/U_\mathrm{P}$ between ionisation potential and ponderomotive potential.

$$E_\mathrm{max} = 3.17 \cdot U_\mathrm{P} + F\left(I_\mathrm{P}/U_\mathrm{P}\right) \cdot I_\mathrm{p} \tag{2.27}$$

In general, $F \approx 1.32$ and converges for large values of $I_\mathrm{p}/U_\mathrm{P}$ against unity.

2.4.3 Harmonic Generation Inside Filaments

Third harmonic generation in gaseous media by a focused laser beam is known since WARD *et al.* [War69]. In 2002, AKÖTZBEK *et al.* noticed THG also inside a femtosecond laser pulse filament in air [Akö02]. Both the fundamental and third harmonic pulse show radial confinement over a range larger than the RAYLEIGH length. This was interpreted as the result of a non-linear phase-locking mechanism. The findings are supported by several experimental reproductions and theoretical studies of two-colour filamentation [Akö03; Yan03; Ber05; Thé07b; Xi09].

The conversion efficiency to the third harmonic from filamentation was first addressed by YANG *et al.* [Yan03]. However, the UV emission in air has a complicated spatial distribution, and a high conversion efficiency does not necessarily yield a usable beam profile [Ale05; Pea98]. THÉBERGE *et al.* discovered that there is a weak central spot of THG radiation from a filament, surrounded by one or several rings containing $\sim 85\,\%$ of the energy [Thé05a; Thé07a]. Conical emission originates from the unguided propagation of UV radiation in the filament, accumulating a phase-mismatch with respect to the guided laser pulse [Cou07].

The use of differential pumping has enabled KOSMA *et al.* to suppress conical emission in the UV part of a filament's super-continuum [Kos08b]. Considerable enhancement in THG was achieved by crossing two filaments [Yan09; Liu11], or disturbing the filament with a non-collinear propagating strong pulse generating a plasma string [Sun09; Sun10]. A similar increase in conversion efficiency is induced by a thin metal fibre placed perpendicular to the filament [Zha10] or an aluminium foil with a pinhole [Liu11]. Using three filament beams in a non-collinear geometry, THG enhancement is observed due to a plasma grating formed by two filaments [Liu12]. By introducing a pinhole to truncate the filament and simultaneously creating a pressure gradient, we enhanced the on-axis conversion efficiency by several orders of magnitude, maintaining a clean beam profile, as shown in Section 3.3 and [Sch11d].

The phenomenological interpretation of this enhancement is demonstrated by LIU *et al.* as a destructive interference of THG in the first and second half of the filament due to a GOUY phase-shift [Liu11]. However, this interpretation is only valid for short filaments, as the authors note. In case of an additional pressure gradient, considerable influence on THG is attributed to adiabatic phase-matching [Sch11d], detailed in Section 3.3.

Significant spectral broadening during filamentation has been observed many times in the visible (VIS) and UV spectral range (see e.g. [Thé05b; Méj06]). This opens the attractive possibility of sub-femtosecond pulse generation, as the optical cycle of a pulse at 265 nm is as short as 0.85 fs. Furthermore, the conversion efficiency to low-order harmonics is in the perturbative regime and, therefore, several orders of magnitude above the efficiency of HHG. Although the spectral bandwidth is suitable for the generation of ultrashort UV pulses, recent experiments generate the UV light before entering a filament [Gho11]. Alternatively, the generation is done by FWM of different input wavelengths inside filaments, resulting in UV pulses with 50 fs [Beu10] and 10 fs [Kid10] duration. REITER *et al.* exploited THG in neon, reaching a pulse duration of 3 fs [Rei10]. Nevertheless, the input pulse duration in this experiment is as low as 4 fs, so that neither filamentation nor spectral broadening is necessary in the conversion process.

Generation of third harmonic radiation directly inside a filament, as discussed in Chapter 3, results in broadband UV emission with prospects on a sub-femtosecond pulse duration at a record-breaking pulse energy. An approach of temporal characterisation capable to resolve few-cycle UV pulses is presented in Chapter 4. However, dispersion compensation and pulse compression remain crucial in this wavelength region, as discussed in Section 4.4.

High-Order Harmonic Generation

Although the simple filamentation models do not predict it, GAARDE and COUAIRON showed by numerical calculations the possibility of intensity spikes (ISs) in an argon filament [Gaa09]. Figure 2.11 shows a sketch of the IS generation. The complex spatio-temporal dynamics inside a filament lead to self-focusing and self-compression of the pulse until substantial ionisation occurs (fig. 2.11(a)). A radially varying electron density is generated, causing defocusing and therefore different propagation speeds for the on-axis (faster) and off-axis (slower) parts of the pulse (fig. 2.11(b)). Self-steepening and SPM lead to an accumulation of energy in the trailing part of the pulse (fig. 2.11(c)), together with high-energy frequency parts trailing behind the main peak because of dispersion. At a sufficiently high intensity,
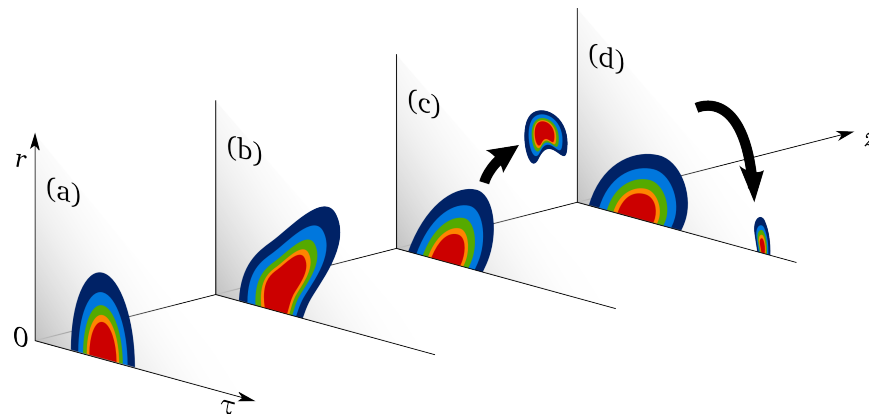
Figure 2.11: Formation of an on-axis intensity spike. The schematic diagram shows four spatio-temporal graphs of the pulse local time τ versus the beam radius r at four propagation distances z in the filament. Intensity is encoded in colours. **(a)** The pulse at the onset of ionisation; **(b)** the trailing edge of the pulse defocuses; **(c)** a sub-pulse forms off-axis and gains energy; **(d)** the sub-pulse self-compresses and refocuses rapidly.

the trailing part refocuses to form a short sub-pulse, exceeding the clamping intensity by more than a factor of three (fig. 2.11(d)). [Gaa09; Ste11a]

The presence of an IS is beneficial for the generation of high-order harmonics at that specific position inside the filament. However, absorption in the high-pressure regime of a filament is strong (see figure 2.12) and the harmonic radiation is not easily accessible. Using a method described in detail in Chapter 3 and reference [Sch11a], the filament is truncated at variable positions and the spectral evolution and generated radiation is tracked along the propagation axis. The theoretical prediction of ISs in an argon filament is thus experimentally observed by STEINGRUBE *et al.* [Ste11b]. In air filaments, simultaneous generation of third and high-order harmonics has been studied using the same method [Voc12c]. The experiments and results are discussed in Chapter 3.
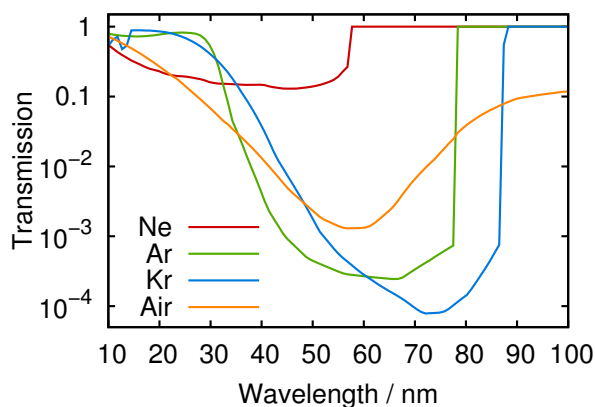

Figure 2.12: Transmission data for argon, krypton, neon and air at 900 mbar pressure for the XUV spectral range. The transmission is calculated for a length of 100 μm propagation in the gas. [Hen93]

2.5 Frequency-Resolved Optical Gating

Generation of ultrashort laser pulses in the few-femtosecond domain, as possible by fila-mentation, raises the question of measurement methods for such ultrashort process. Two elaborate methods evolved out of laser development with several improved, specialised or generalised derivatives. Frequency-resolved optical gating (FROG) [Kan93; Tre00] is, simply spoken, a spectrally resolved non-linear auto-correlation. From the spectrogram, the pulse envelope and phase is iteratively reconstructed. There are many different FROG geometries using SHG, non-linear polarisation rotation, THG or even HHG as a non-linear process.

An alternative approach to temporal pulse characterisation is spectral phase interferometry for direct electric-field reconstruction (SPIDER) [Iac98]. No iterative reconstruction is needed for this method, where two replicas of the input pulse generate the sum frequency with different spectral parts of a long, chirped pulse, generating a spectral shear. The interference in the recorded spectrum contains all necessary information to retrieve the pulse phase and envelope.

Both principal methods have their advantages. For the characterisation of laser pulses from filamentation, we look for a set-up working for ultrashort pulses with broad spectra, including the complete VIS and UV range. A common disadvantage for many realisations of both, FROG and SPIDER, is the use of frequency up-conversion processes, as the absorption of the generated radiation puts an upper limit to the input frequency. Additionally, material dispersion has a strong influence in the UV spectral region and disqualifies the use of transmissive optics, e.g. polarisation optics.

A measurement method fulfilling these restrictions is transient grating frequency-resolved optical gating (TG-FROG), a FROG derivative developed and used within this work. While the basic theory of FROG is discussed in the following section, the details on the used TG-FROG set-up can be found in Chapter 4.

2.5.1 Third-Order Frequency-Resolved Optical Gating

Most prominent among the FROG geometries is SHG-FROG, generating a signal in the second harmonic with high sensitivity, signal-to-noise ratio and low input energy requirement. Although easy to realise, a frequency-resolved second-order auto-correlation always contains a time-directional ambiguity. This is caused by the nature of a second-order non-linearity

to yield the same SHG-FROG-trace for a complex field amplitude $E(t)$ and its complex conjugate $E^*(t)$. Furthermore, second-order FROG-traces are unintuitive and not very expressive. For these reasons, a third-order non-linearity is preferable to use whenever applicable. [Tre00]

A FROG-trace is a spectrogram of the form

$$S_g^E(\omega,\tau) = \left| \int_{-\infty}^{\infty} E(t) \cdot g(t-\tau) \cdot e^{-i\omega t} \, dt \right|^2 , \tag{2.28}$$

where $g(t-\tau)$ denotes a variable-delay gate function, which is in most cases a time-delayed replica of the electric field itself. Considering a third-order non-linearity, three replicas of the electric field are used, one of which acts as a gate function:

$$S_E^{E^2}(\omega,\tau) = \left| \int_{-\infty}^{\infty} E_1(t) E_2(t) E_3^*(t-\tau) e^{-i\omega t} \, dt \right|^2 \tag{2.29}$$

Depending on the geometrical direction of the signal and which of the signal beams is delayed, the FROG-trace is either a self-diffraction (SD)- or polarisation gating (PG)-type.

$$S_E^{SD}(\omega,\tau) = \left| \int_{-\infty}^{\infty} E^2(t) E^*(t-\tau) e^{-i\omega t} \, dt \right|^2 \qquad \text{self-diffraction FROG-trace} \tag{2.30}$$

$$S_E^{PG}(\omega,\tau) = \left| \int_{-\infty}^{\infty} |E(t-\tau)|^2 E(t) e^{-i\omega t} \, dt \right|^2 \qquad \text{polarisation-gating FROG-trace} \tag{2.31}$$

For both SD and PG traces, a phase-retrieval algorithm is readily available, e.g. in Femtosoft Technologies' *Frog3* software [Fem12]. It results in a time-dependent pulse envelope (and therefore full width at half maximum (FWHM) pulse duration) and phase reconstruction and a retrieved FROG-trace to be compared with the input trace to check for accuracy. [Tre00]

2.6 Applications

A large interaction length and absence of a damage threshold shape the application field of filamentation. With a range of several kilometres [Wös97; Rod04; Méc04; Méc05], long-

range filaments are used for remote sensing [Rai00], spark and lightning triggering [LaF00] and LIDAR [Ste04; Méj04]. Spectral broadening via SPM is used to reduce pulse durations down to the few-cycle regime (see section 2.6.1). Generation of high-order harmonics connects filamentation to the field of attosecond physics (see section 2.6.2) and nanoscale imaging (see section 2.6.3).

2.6.1 Pulse Compression

Additional frequency generation due to SPM and plasma generation enables further compression of intense femtosecond pulses. As compression after a gas-filled hollow-core fibre is common practise [Bra00], omitting the fibre and using filamentation for spectral broadening and compression with double-chirped mirrors (DCMs) becomes an elaborate method in the VIS range [Ste09a; Eck08; Kos08a]. Even the few-cycle regime can be reached using multi-cycle driver pulses and spectral broadening in a filament [Gou08].

Although residual chirp has to be removed by pulse compressors or DCMs, there is theoretical and experimental evidence for a self-compression effect in filamentation [Cou05; Cou06; Mys08]. By carefully adjusting the input pulse parameters, self-compression without the need of a post-compression stage has been shown [Sti06; Sku06]. The effect depends critically on modulational instabilities [Cou07], so that Brée *et al.* implemented a cascaded scheme of several filamentation stages to achieve self-compression with a reduced non-linearity [Bré10].

In recent years, pulse compression capabilities of filamentation are in most cases used in addition to DCMs, prism or grating compressors. The near infrared (NIR) spectral range is already described by theoretical studies [Ber08]. However, for UV wavelengths, dispersion properties seem to limit the self-compression ability. Since DCMs are a challenging task in this spectral region due to absorption, classical pulse compression has to be applied to broad UV spectra from filamentation. A more detailed discussion can be found in Section 4.4.

2.6.2 Attosecond Pulse Generation

The generation and verification of attosecond pulse trains (APTs) from the process of HHG [Pap99; Pau01] is a fast growing research field of strong-field physics that has brought up its own variety of applications. For several ultrafast atomic and molecular investigations, i.e. the recording of a *molecular movie* [Cor07], the generation of isolated attosecond pulses (IAPs)

is necessary. IAP generation requires a fast gate for HHG to occur only at a singular event, which can be realised by few-cycle driving pulses and spectral filtering of the high-energy range[Hen01; Bal03], polarisation gating [Cor94; San06] or double-optical gating [Gou08]. The forming of an ultrashort sub-pulse in filamentation (see Section 2.4.3) and resulting HHG from within the filament (see Section 3.4) prospects direct IAP generation without the need of CEP stabilisation [Ste11b]. Experimental verification of this IAP is work in progress.

2.6.3 Coherent Diffraction Imaging

The use of x-rays to record the diffraction pattern of periodic nano-scale structures is a well known method in crystallography [Ash76]. Miao *et al.* extended this method to non-crystalline objects by recording the x-ray diffraction pattern of arranged gold spheres of 100 nm diameter on a silicon nitride (Si_3N_4) membrane [Mia99]. Using the method of phase-retrieval by oversampling, a real image can be reconstructed from such a diffraction pattern [Mia03]. With a resolution of 70 nm and x-ray wavelengths, the coherent diffraction imaging (CDI) method is ideally suited for biological samples. However, long-time x-ray exposure is necessary and presents a damage hazard for samples such as a cell, a virus or a macroscopic bio-molecule.

If an ultrashort and very bright coherent XUV or x-ray pulse is applied to a biological sample, theory predicts the emergence of a single diffraction pattern before the sample turns into a plasma [Neu00; Jur04; Hau04; Ber04]. The first experiment of this kind has been realised with a high intensity coherent x-ray pulse at the free-electron laser in Hamburg (FLASH), resulting in a successful reconstruction of a pattern on a gold-coated Si_3N_4 membrane [Cha06b]. Since the sample is destroyed in the process of imaging, three-dimensional information can only be obtained by imaging of multiple identical samples, which again excludes most biological material.

Ravasio *et al.* demonstrated CDI using a laser-based HHG setup and broke the limitation of this imaging method to free-electron laser facilities [San07; San08]. For reconstruction of the images, single-shot diffraction patterns were sufficient. Furthermore, multi-shot imaging without signs of destruction was demonstrated with high-order harmonic pulses, opening the way for three-dimensional imaging with a unique sample, yet keeping the overall exposure time comparatively low.

In 2010, RAINES *et al.* proposed a method entitled *ankylography* to reconstruct a three-dimensional real image from a single diffraction pattern. However, certain additional requirements are introduced for the method to work and to avoid ambiguities. It is described in detail and used for experimental data in Chapter 5.

3

Harmonic Generation in Filaments

This chapter is dedicated to the generation and investigation of third harmonic generation (THG) and high-order harmonic generation (HHG) within the high-intensity core of a filament. Generation of third harmonic order radiation of an incident laser inside a filament has been reported in 2002 for the first time [Akö02; Yan03] (see also Section 2.4). However, generation of high-order harmonics is difficult due to technical limitations, e.g. high absorption of XUV radiation at atmospheric pressures. For the scientific work presented in this chapter, a new characterisation method for filaments is used, enabling the tracking of the spectral and temporal pulse evolution along the propagation axis of the filament. Section 3.1 discusses this method in detail. Investigations pursued in the VIS and UV spectral region are presented in Sections 3.2 and 3.3 respectively. In Section 3.4 the occurrence of HHG and the detection of XUV radiation is presented. Section 3.5 discusses the modification of the method for use with high-pressure filamentation in up to five bar of a noble gas.

3.1 Tracking of the Pulse Evolution

Diagnostic access to the physical properties in the hot core of a filament is difficult for several reasons. First of all, the pressure regime for filamentation is not compatible with the propagation of XUV radiation due to the limited transmission. As stated in Section 2.4, high-order harmonics are quickly absorbed and cannot be detected in the far field.

Secondly, the intensity reaches the vicinity of the ionisation threshold of air or a rare gas. Consequently, most optical materials and measurement equipment does not survive in these conditions. For this reason, many studies on filamentation are based upon the

far-field characterisation of the output pulses. The complicated dynamics inside the non-linear interaction zone are mostly known only from complex numerical simulations [Lor12; Kol04].

Existing experimental approaches to put diagnostics inside a filament are based on a time-resolved shadowgraphic technique [Min08; Min09], allowing for the retrieval of pulse dynamics [Pap08]. Another method is the use of impulsive vibrational RAMAN scattering and measurement of power spectra along the propagation axis [Odh10]. Other approaches stop the filament by means of a pinhole, but continue to guide the pulse in argon afterwards [Ury10]. These methods are all either indirect or bear a risk of modifying the pulse properties due to subsequent propagation in a medium.

The method used in the present work circumvents these limitations [Sch11a]. It is based on a semi-infinite gas cell (SIGC) geometry [Pap01; Ste09c] with two differential pumping stages separated by laser-drilled pinholes, as detailed in Section 3.1.1. While the non-linear medium is removed by vacuum pumps, the filament's energy reservoir is stopped by the pinhole, efficiently terminating all non-linear propagation effects and, therefore, the filament.

It is now possible to extract radiation from different positions in the filament and therefore track its evolution along the self-guided propagation. Section 3.1.2 describes measurement methods that are common for all experiments based on this tracking set-up. Analysis and visualisation of recorded data, as performed throughout this work, is specified in Section 3.1.3.

3.1.1 Experimental Set-Up

The set-up for filament analysis along the propagation axis is depicted in figure 3.1. It has emerged from a standard filamentation set-up consisting of an input aperture, a focusing mirror with a radius of curvature of 4 m and a glass tube with an uncoated 1 mm-thick calcium fluoride (CaF_2) entrance window. If the entrance window is used at the Brewster angle, a change of gas or pressure inside the glass tube results in a gas prism. To avoid angular dispersion from this prism, the window is only marginally tilted with respect to the incident beam. The incoming beam passes an aperture before hitting the curved mirror, focusing it into the glass tube and forming a filament. To gain access to pulse properties inside the filament, we truncate it at a certain position. This is done by placing a stainless steel plate of 0.5 mm thickness and 33 mm diameter in the beam, as displayed in figure 3.2.
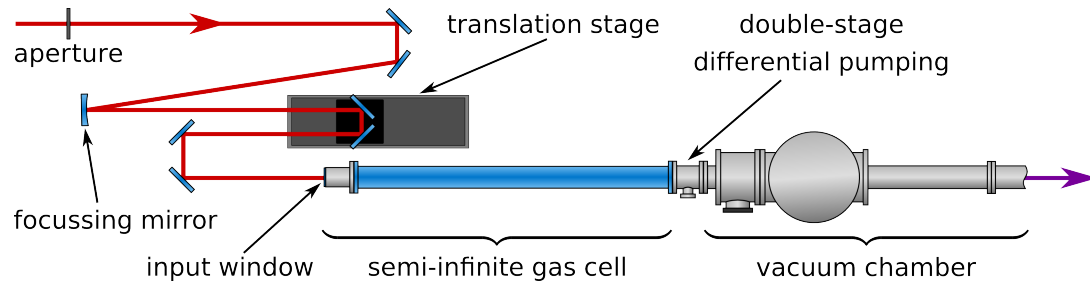
Figure 3.1: Experimental set-up for tracking the pulse evolution along a filament. The incident beam (solid red line) passes through a variable input aperture and is focused by a concave mirror with a radius of curvature of 4 m into a SIGC. A translation stage allows to change the distance between the focusing mirror and the input window. The end of the gas-filled cell is formed by a differential pumping stage (see figure 3.2). After the propagation in vacuum, different set-ups are used depending on the spectral region of the investigated radiation.

The glass tube is now forming a SIGC with the entrance window and the steel plate. Due to high intensity, the steel plate is subject to laser-ablation, producing a hole with a typical diameter of 0.8 mm. The pinhole diameter is not constant, but starts up small and increases slightly over the experiment time due to pointing instability of the beam and slow heat dissipation on the plate. Therefore, it does not represent the filament's diameter.

To be able to quickly switch to a fully propagating filament, a second glass tube is available by moving a flip mirror. It has an identical entrance window at the same distance to the focusing optics and shares the same gas supply as the SIGC. The full filament is used to optimise for initial chirp of the input laser pulse and to check for multiple filament formation.

Behind the first pinhole of the SIGC, the gas pressure is lowered by an oil-sealed double-stage rotary vane pump. To prevent oil vapour from contaminating the vacuum chamber, foreline oil traps are used at every pump. A gas jet is inevitably emerging from the pinhole, quickly expanding into the subsequent vacuum chamber. This creates a steep pressure gradient on the optical axis, down to a pressure below 10 mbar. In several pressure regimes and focusing conditions, it has been observed that the gas flow through the pinhole increases slightly if the laser beam is blocked. Although not investigated quantitatively, the effect appears to be more pronounced in cases of strong plasma generation. Nevertheless, this effect favours a low pressure after the first pinhole.

A second steel plate is placed approximately 1 cm behind the first pinhole. The second laser-drilled pinhole is to some extent smaller than the first one (about 0.5 mm in diameter). Both pinholes are produced directly in the set-up, where the pressure in the vacuum chamber permits information on the progress.
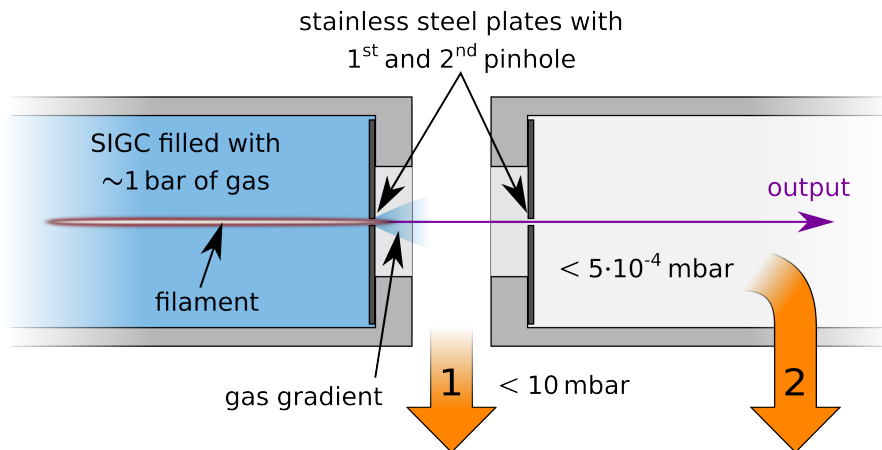
Figure 3.2: Differential pumping in two stages: The filamentation process is abruptly stopped by blocking the surrounding energy reservoir at the first pinhole. Due to rough vacuum pumping, the non-linear medium is removed, leaving only a strong pressure gradient in direct vicinity of the pinhole. A typical pressure reached in this stage for 1 bar of air or argon in the SIGC is below 10 mbar. The second pinhole is at a distance of roughly 1 cm to the first one. Turbo-molecular pumps lower the pressure to less than $5 \cdot 10^{-4}$ mbar in the second stage to grant absorption-free propagation.

The vacuum chamber behind the second pinhole is evacuated by a turbo-molecular pump, reaching a pressure below $5 \cdot 10^{-4}$ mbar. Radiation can propagate virtually free of absorption, dispersion and non-linear effects in this area.

To be able to extract the filament pulses at different positions, we change the distance between the focusing mirror and the entrance window by means of a 150 mm motorised translation stage. Care has to be taken to minimise the distance between the focusing mirror and subsequent dielectric mirrors in order to stay below the damage threshold. If the entrance window is to close to the focus, white-light generation is initiated. This can also be caused by hot spots in the beam profile or diffraction patterns from apertures. Therefore, the spectral width has been checked for the complete range of positions with an evacuated gas cell to ensure the absence of non-linear effects in the entrance window.

3.1.2 Measurement Methods

The pressure inside the SIGC is influenced by a gas inlet valve and the exit pinhole size, which is changing with the exposure time. A four-channel proportional integral derivative (PID) controller measures the actual pressure using a *Baratron* absolute pressure gauge and regulates the gas flow to maintain a set value.

The translation stage is controlled by a computer, alternating movement steps and data acquisition. Data recording devices are spectrometers for the VIS, UV and XUV spectral range, all accessed by the same self-developed software. Up to two spectrometers can be used simultaneously to record data.

3.1.3 Data Analysis

From the recorded spectral power densities, false colour representations are plotted. Since no absolute power calibration of the used spectrometers and detectors is available, the spectral power density and all subsequently calculated values are displayed normalised. The reference for the position axis is the distance L between the focusing mirror and the first pinhole, measured with an accuracy of ± 1 cm. Since the 'start' of a filament is neither easily defined nor measured, we use L to represent the truncation point and estimate the filament's length.

Unless otherwise noted, the data is corrected for the detector sensitivity curve. Integration along the spectral axis for each truncation position gives rise to a value proportional to the pulse energy. Spectral widths are taken at the FWHM after background and noise subtraction. In some cases with low signal-to-noise ratio, adjacent data points have been smoothed carefully to remove the influence of noise on the FWHM. The Fourier-limit of the FWHM pulse duration is calculated directly from the spectra by means of a fast fourier transform (FFT) in assumption of a flat spectral phase.

3.2 Spectral Broadening in the Visible Range

Additionally to the experimental set-up displayed in figure 3.1, an output window is placed at a distance of 1 m from the exit pinhole. It is a 2 mm-thick CaF_2 window tilted by 10°. An optical fibre has been used to record the spectra, using an Avantes USB spectrometer. Figure 3.3 shows experimental results from a filament in air at 1 bar. The distance between the focusing mirror and the first pinhole is denoted on the horizontal axis. It represents the truncation point of the filament and, therefore, it's length, offset by the distance between focusing mirror and the filament's start. At the leftmost position, a spectrum is measured after a short filament propagation (fig. 3.3(a)). The corresponding spectral width (blue curve in fig. 3.3(b)) is about 40 nm. Note that the spectrum appears broader in fig. 3.3(a) due to logarithmic scaling of the colour palette. A longer propagation of the filament results
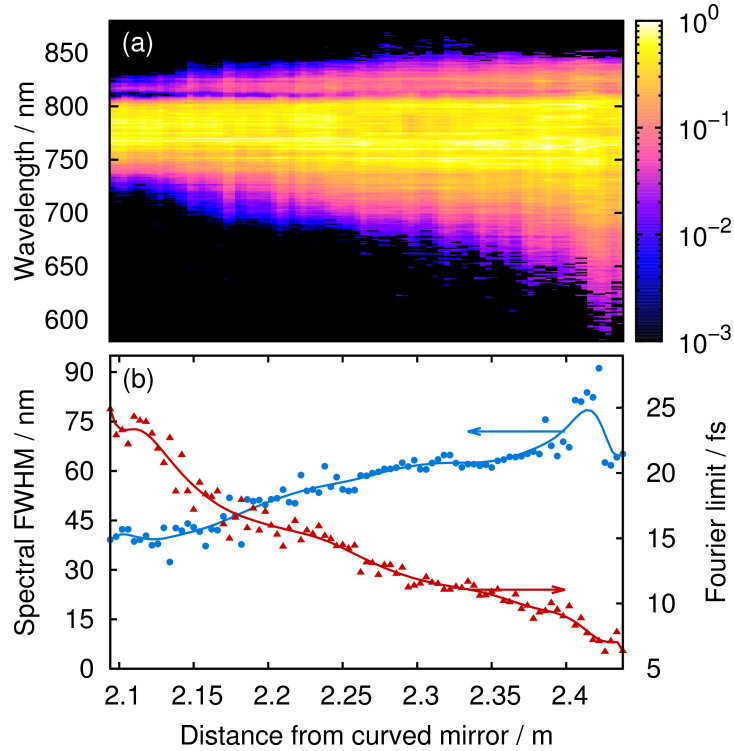
Figure 3.3: Spectral broadening imposed on the VIS spectrum in an air filament, depending on the truncation position in terms of the distance from the focusing mirror. **(a)** normalised recorded spectral power density. **(b)** spectral FWHM and Fourier limit calculated from the data presented in (a). Experimental conditions: 1 bar of air, input power 1.1 mJ, aperture diameter 6.5 mm. The solid lines represent a moving average over four data points.

in monotonic increase of the spectral width. Consequently, the theoretical Fourier limit (red curve in fig. 3.3(b)) is reduced towards 6 fs. The input pulse energy is limited to 1.1 mJ behind a 6.5 mm input aperture, transmitting 73 % of the beam energy.

In 1 bar of argon, the pulse energy is reduced to 0.9 mJ in order to avoid multiple filaments. Compared to air, the spectral broadening in argon is more pronounced in figure 3.4, reaching an octave at a distance of 2.2 m. As a result, a Fourier limit of 2.6 fs is calculated (see red curve in fig. 3.4(b)). An equally broad spectrum has been compressed with several bounces on DCMs after the filament. The compressed pulse duration was measured to 7 fs using SPIDER, as published in [Ste09a].

3.2.1 Aperture, Energy and Multiple Filaments

An input aperture is used in most filamentation experiments to compensate for an imperfect spatial energy distribution in the beam profile, which is responsible for the formation of
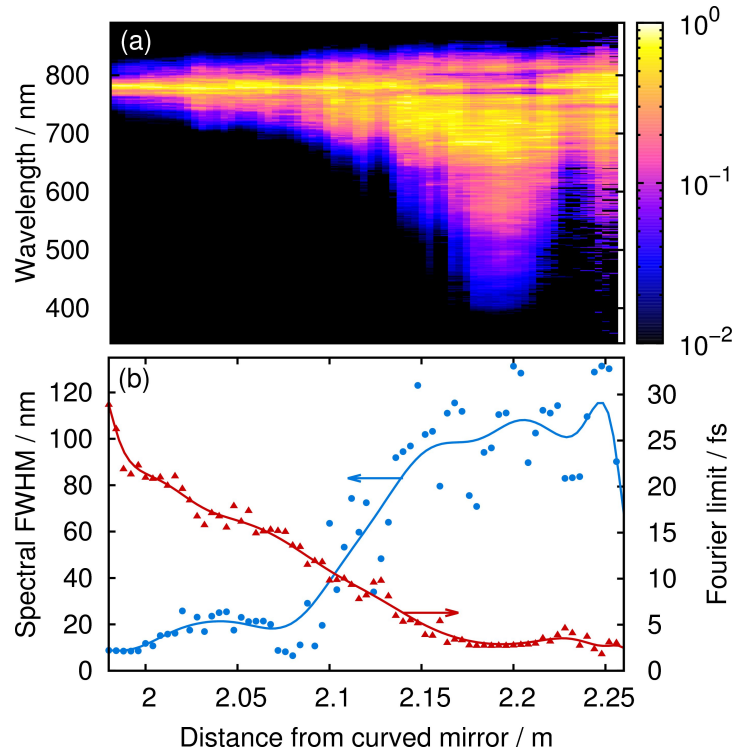
Figure 3.4: Filamentation in argon showing spectral broadening in the VIS range, depending on the truncation position in terms of the distance from the focusing mirror. **(a)** normalised recorded spectral power density. **(b)** spectral FWHM and Fourier limit calculated from the data presented in (a). Experimental conditions: 1 bar of argon, input power 0.9 mJ, aperture diameter 5.5 mm.

multiple filaments [Cou07]. The result, however, depends on the current beam profile and diameter, which may differ due to laser re-adjustment or modification. Furthermore, adjustment of the aperture diameter couples major parameters, namely the input pulse energy, spatial distribution and the focusing conditions. Of these three, only the input energy can be set independently.

Imaging the filament's output into a spectrometer often prevents a view of the beam profile to detect the onset of multiple filaments. To identify a regime leading to a single filament in argon, the beam profile of a fully propagated filament is displayed on a screen in the far field during parameter variation. Multiple filament formation is identified by the appearance of multiple white light spots, often accompanied by pointing instabilities. If this situation is found, the input pulse energy before the aperture is reduced until a single filament is formed. The maximum input pulse energy for four aperture diameters in dependence of the argon pressure is displayed in figure 3.5, under the restriction of single filamentation. Clearly, a combination of high pressure and input energy leads to multiple filaments and a high value
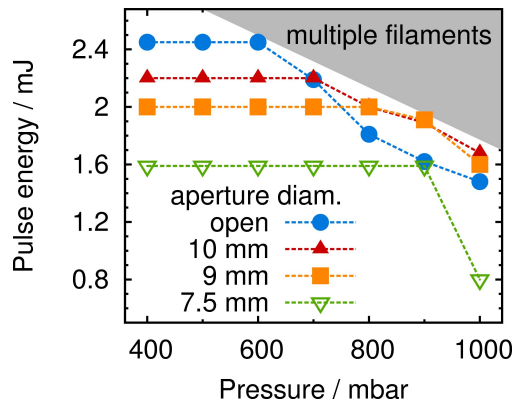
Figure 3.5: Avoiding multiple filaments in argon by choice of pressure and input energy. For four different aperture settings, the existence of a single filament core has been checked on a screen in the far field of a full filament. The pressure is raised to see the onset of multiple filamentation. An attenuator is used to lower the input pulse energy until a single filament is obtained again. The broken lines are only guides to the eye.

of the input power to critical power ratio. Although fine-adjustment of the input aperture can lead to increased filament stability or improved spectral broadening, figure 3.5 shows a grey area where multiple filaments arise independently of the input aperture. Therefore, changing the aperture diameter has a major influence due to a change in transmitted energy, while modification of the focusing conditions is less influential.

3.3 Third-Order Harmonic Generation

Inside the white light core of a filament, the intensity is high enough to trigger THG, as introduced in Section 2.4.3. In an undisturbed filament, phase-matching is only achieved off-axis, leading to conical emission. However, the tracking method used in this work truncates the filament and facilitate on-axis phase-matching. Additionally, a steep pressure gradient at the point of truncation positively influences the on-axis generation of third-order harmonic radiation.

This section consists of two parts. First, the spatial properties of the generated UV radiation is analysed, as well as the conversion efficiency of the THG process. The second part describes its spectral evolution along the filament's propagation axis.
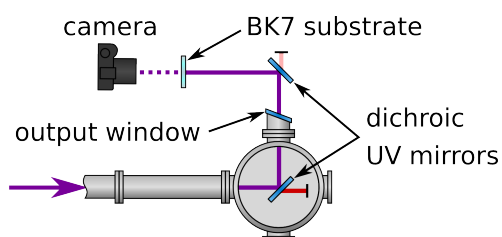

Figure 3.6: Additional set-up for analysis of spatial beam properties inside a filament. Visible spectral parts are separated via two dichroic mirrors highly reflective for UV radiation. The THG light induces fluorescence in a BK7 substrate, which is recorded with a DSLR camera.

3.3.1 Beam Profile Analysis and Enhanced Emission

The set-up for beam profile analysis is attached to the previous set-up for tracking of filaments, detailed in Section 3.1 and figure 3.1. Joined at the vacuum output, about 1 m after the differential pumping stage, is the arrangement shown in figure 3.6. Two dichroic UV mirrors are used to separate the VIS and UV spectral parts, whereof one is placed inside the vacuum. An output window of 2 mm CaF_2 terminates the chamber. Outside the vacuum, the THG signal induces linear fluorescence in a BK7 substrate. It is imaged by a standard digital single-lens reflex (DSLR) camera and analysed by taking exclusively the blue signal channel of the recorded image, effectively eliminating residual driving laser light.

In case of a fully propagating filament, conical emission of third-order harmonic light is shown in figure 3.7(a). The intense cone contains 99.6 % of the overall UV intensity. Previous studies have shown that disturbing the filament propagation with a plasma string [Sun09; Yan09; Sun10], a second [Liu11] and third filament [Liu12] or a thin metal fibre [Zha10] influences the energy distribution between cone and central part. In disturbing the filament by imposing a pressure gradient and stopping its non-linear propagation with a pinhole, we observe a bright THG beam on axis, displayed in figure 3.7(b). Visible from the lineout graphs in fig. 3.7(b), the profile is nearly Gaussian-shaped. Note that it cannot be concluded that conical emission is suppressed, as it would be blocked by the pinhole in this arrangement.

Comparison of the fluorescence intensity distributions is shown in figure 3.8. The useful signal in the central spot is increased by roughly three orders of magnitude (28 dB), outperforming previously published enhancements. Possible detector saturation may conceal an even larger enhancement, as the Gaussian fit (broken blue line) suggests. By removing the pressure gradient (by switching of the vacuum pumps) it is evident, that the gradient enhances the conversion efficiency to the third-order harmonic to 0.2 ‰. However, using the pinhole without pressure gradient still improves the on-axis efficiency.

Source of the enhanced on-axis emission of THG in this experiment is an improved phase-matching condition [Sch11d]. In the fully propagating filament, a match of phase-front curvature of the fundamental and UV field is limited to the start of the filament. Since the UV part is not guided, this match is soon lost, preventing efficient on-axis THG. The phase-front mismatch is geometrically compensated in off-axis direction, leading to intense conical emission. Disturbing the filament with a pinhole stops guiding of the fundamental beam, allowing on-axis phase-matching beyond the non-linear focus. Additional increase of
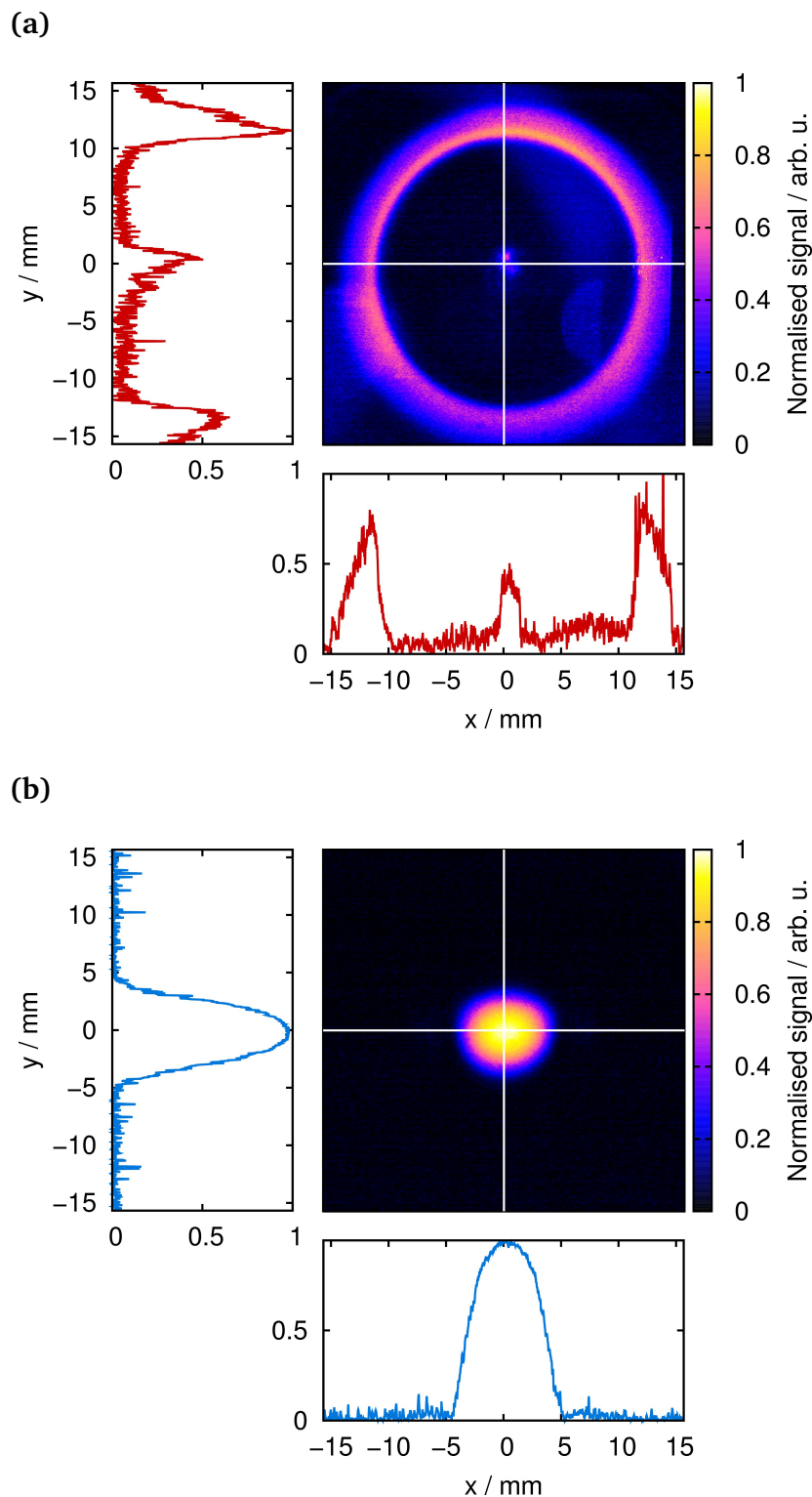
(a)

(b)

Figure 3.7: Conical and on-axis emission of THG light from an air filament. Both images are taken with a digital camera from the UV induced fluorescence in BK7. The blue curve shows line-out graphs along the axes, indicated by white lines. **(a)** beam profile in the far field behind an undisturbed filament with a pronounced conical emission ring. **(b)** output profile of a truncated filament with a rapid vacuum transition and a pressure gradient. Only the blue channel of the full colour picture is used in (a) to reduce noise from stray fundamental light.
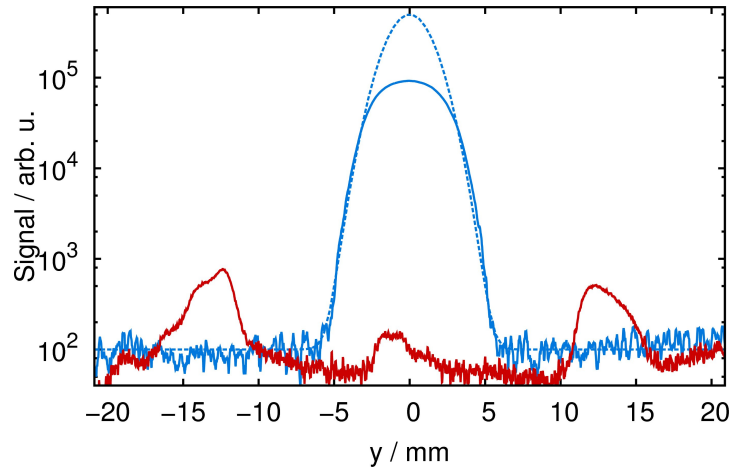
Figure 3.8: Beam profile and signal strength comparison of THG signals from a truncated (blue solid curve) and undisturbed (red curve) filament. The broken blue line represents a Gaussian fit, assuming a detector saturation in the centre peak.

conversion efficiency could be attributed to adiabatic change of phase-matching conditions [Suc08; Suc09]. Due to a rapid density modification in vicinity of the pinhole, ideal phase-matching of THG and a high amount of conversion is accomplished in a narrow spatial area within the pressure gradient. After short propagation, the change in pressure induces a phase-mismatch, efficiently suppressing back-conversion, yielding an increase in conversion efficiency.

3.3.2 Spectral Analysis

For spectral analysis of THG, a common method is used to remove the visible part of the spectrum. As sketched in figure 3.9, a prism sequence splits the beam in its spectral components. A razor blade is used to block part of the spectrum in the Fourier plane. Unblocked radiation is back-reflected with a slight change in beam height and sent to a spectrometer with a U-shaped mirror.
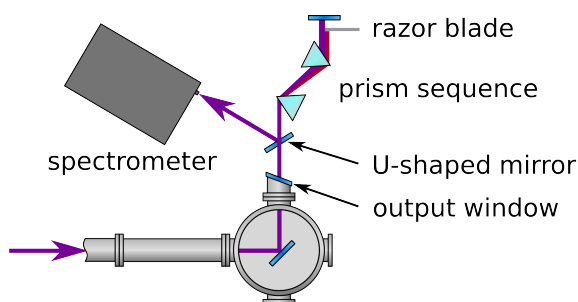

Figure 3.9: To track the evolution of THG spectra inside a filament, the set-up displayed in figure 3.1 is extended. The laser beam leaves the vacuum chamber via a CaF$_2$ window after one reflection on an aluminium mirror. A prism sequence splits the spectrum into its components where the VIS part is blocked. The UV part is reflected back and into a spectrometer.
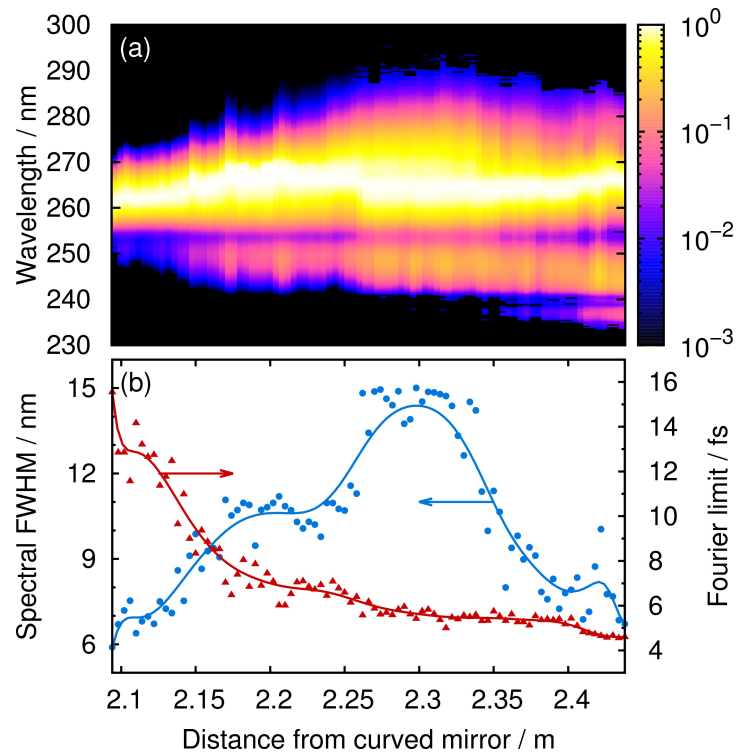
Figure 3.10: Broadband THG spectrum in a truncated air filament, depending on the truncation position in terms of the distance from the focusing mirror. **(a)** normalised recorded spectral power density. **(b)** spectral FWHM and Fourier limit calculated from data displayed in (a). Experimental conditions: 1 bar of air, input power 1.5 mJ before a 6.5 mm-diameter aperture.

Recording the spectrum along an air filament results in a spectral evolution displayed in figure 3.10(a) [Voc12c]. The spectral power density is normalised for each spectrum. At 255 nm and 240 nm, spectral minima are visible, independent of the point of truncation. Most likely, they are caused by absorption of vacuum impurities, e.g. oil vapour deposited on the mirror surface.

Figure 3.10(b) shows the spectral FWHM of THG (blue curve) and the calculated Fourier limit of the pulse duration (red curve). The spectral width increases continuously up to a distance of 2.3 m. For longer propagation distances, the central peak of the spectrum becomes very pronounced and causes a misleading decrease in spectral width, as the spectral wings have less than half of the peak's spectral power density. Taking the full spectrum with a flat phase into account, the pulse duration's Fourier limit is monotonically decreasing towards longer propagation and ends up below 5 fs.

The spectrum of these pulses contains only minor modulations, which positively affects compressibility. Prisms and gratings are available in this spectral region. Concepts for
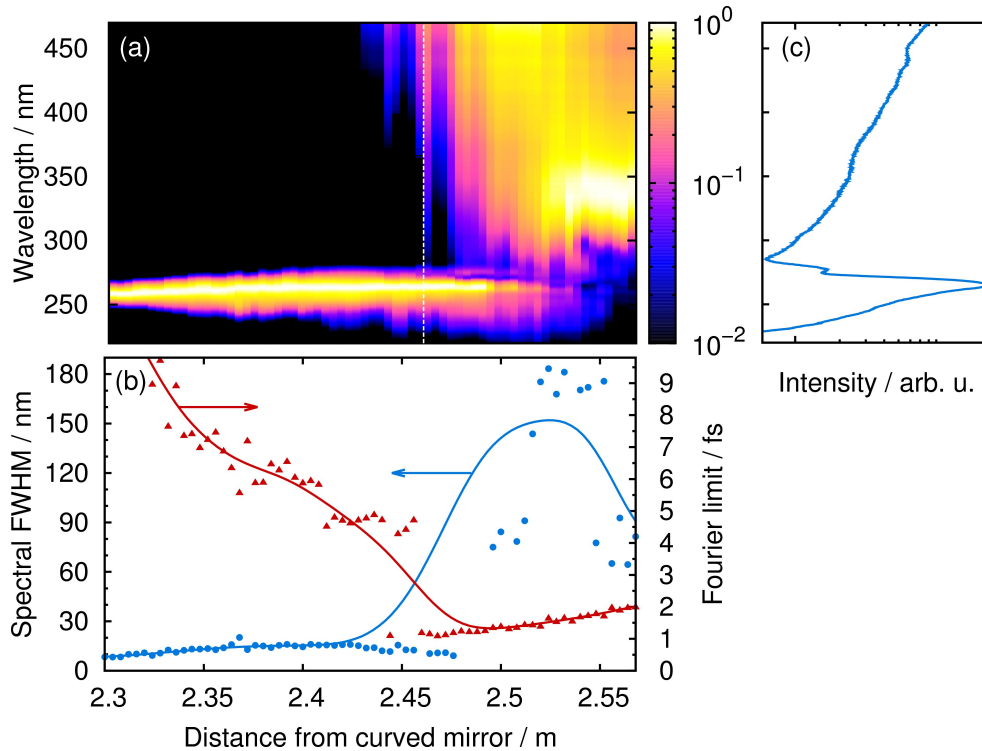
Figure 3.11: Broadband THG spectrum in a truncated argon filament, depending on the truncation position in terms of the distance from the focusing mirror. **(a)** normalised recorded spectral power density. **(b)** spectral FWHM and Fourier limit calculated from data displayed in (a). **(c)** Lineout graph of the M-shaped spectrum at the white broken line in (a). Experimental conditions: 0.9 bar of argon, input power 0.9 mJ, aperture diameter 5.5 mm.

compression of UV pulses are discussed in Section 4.4.

Unlike filamentation in air, the results in argon contain the high-frequency wing of the fundamental part of the spectrum, as shown in figure 3.11(a). Note that the spectral range shown is from 220 nm to 470 nm, while the filament's spectrum extends continuously from NIR to about 270 nm. For propagation distances larger than 2.5 m, the spectrum's visible wing contains more energy than the third-harmonic part.

Spectral width (blue curve) and Fourier limit (red curve) are displayed in Figure 3.11(b). The calculated spectral FWHM consequently increases to form a maximum near 2.5 m. Before that maximum, the Fourier limit develops similar to measurements in air, reaching a saturation of sub-5 fs in the range of 2.4 m to 2.45 m. For larger distances, the spectrum is cut by the spectrometer's long wavelength limit. Calculation of the spectral FWHM depends on this limit and is not always useful. However, calculation of the pulse duration's Fourier limit is not affected by this issue, since it relies on the full spectral power densities.

The visible wing has considerable influence on the Fourier transformation. At a propagation distance of 2.46 m, the two spectral parts result in a Fourier limit of about 1 fs. The spectral shape is displayed as a lineout graph in figure 3.11(c). Due to the spectrometer's upper wavelength limit, the spectrum consists of two peaks at its edges with a minimum in between. Such an M-shaped spectrum is known from positively chirped pulse oscillators for both its low theoretical pulse duration's Fourier limit and its low compressibility due to higher order dispersion. Compression of such pulses is discussed in Section 4.4, using both a grating and prism pair. Limitation of the VIS spectral parts according to the given set-up can be directly incorporated into the compressor set-up, generating an M-shaped spectrum with an adjustable high-wavelengths wing.
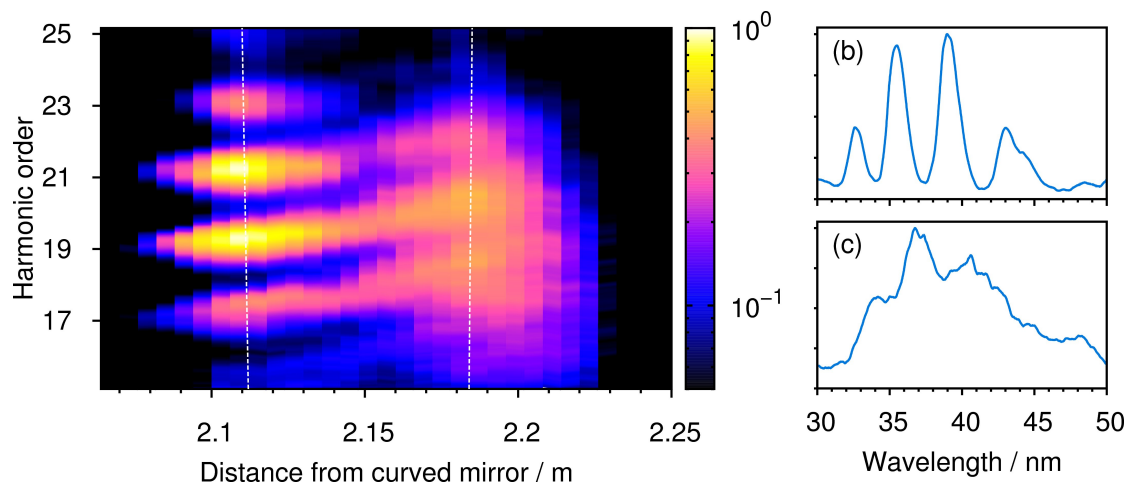

Figure 3.12: (a) HHG spectrum versus the truncation position by means of the distance from the curved mirror. Lineout graphs are shown in (b) and (c) at positions indicated by white broken lines. **(b)** At 2.112 m, the harmonic spectrum is modulated and harmonic orders are well separated. **(c)** In contrast, a continuum is found at 2.185 m distance. Experimental conditions are 700 mbar of argon with 21 GW input pulse power after an aperture of 7.5 mm. [Ste11b]

3.4 High-Order Harmonic Generation

In 1998, LANGE *et al.* observed ATI electrons generated in a xenon gas cell by a laser pulse undergoing filamentation in air [Lan98]. Although the ATI spectra are not directly recorded from the filament but a subsequent xenon gas cell, their experimental observations are indicators of high-order non-linear processes in filaments.

The *Dynamic Spatial Replenishment* model for filamentation (see section 2.3.2) already indicates that on-axis intensity inside a filament is a dynamical value. As detailed in Section 2.4.3, the clamping intensity can be exceeded by spatio-temporal pulse dynamics and focusing, leading to an intensity spike (intensity spike (IS)). The generation of high-order harmonics due to ISs within a filament has been proposed, substantiated by numerical calculations [Gaa09]. Using the method described above (Section 3.1), STEINGRUBE *et al.* showed the existence of ISs in an argon filament by means of HHG [Ste11b].

A high-order harmonic spectrum of a filament in 700 mbar argon is shown in figure 3.12(a). For short propagation distances, the intensity is high enough to trigger HHG. Well separated harmonic orders are observed in the range of 2.08 m to 2.15 m. The modulation depth is visible in a single spectrum lineout graph in figure 3.12(b). With further propagation, a shift of harmonic orders towards short wavelengths is visible, accompanied by a broadening of the harmonic orders. Finally, at 2.185 m, a continuous harmonic spectrum is formed, shown
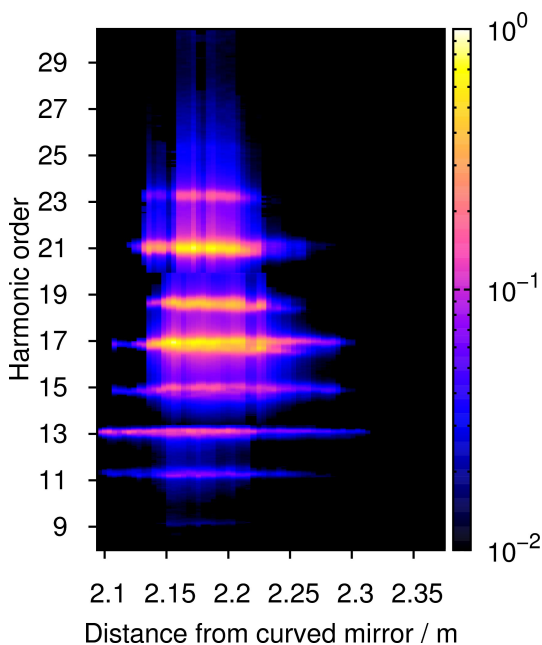

Figure 3.13: Generated harmonic orders inside an air filament, depending on the point of truncation by means of the distance from the focusing mirror. This image consists of three consecutive measurements. Fluctuations in experimental parameters lead to a small mismatch between the three vertical axes.

as a lineout spectrum in figure 3.12(c). Between these two areas, the overall signal intensity decreases.

HHG serves as a probe for on-axis intensity inside the filament, as the HHG process itself is very sensitive to it. The two areas of separated and continuous harmonic generation are interpreted as the formation of two ISs. A modulated harmonic spectrum indicates a multi-cycle IS for short propagation distances. It evolves to a few-cycle IS due to spatial and temporal focusing effects, leading to a continuous spectrum. [Ste11b]

Although the used laser pulses are not stabilised with respect to their CEP, the continuous spectrum shown in figure 3.12 is also visible and stable in single-shot spectra published in [Ste11b], i.e. every laser pulse generates a continuous spectrum. This opens up the possibility of isolated attosecond pulse (IAP) generation with a much simpler setup than used today (see also section 2.6.2). Verification of an IAP emerging from this set-up is pursued by M. KRETSCHMAR within his PhD-thesis at Leibniz Universität Hannover. To shift the harmonic cut-off towards higher energy, we have done similar experiments in neon, which are discussed in Section 3.5.

In air, differences in dispersion and the non-linear index of refraction compared to argon leads to an XUV spectrum presented in figure 3.13. For better readability, the wavelengths axis is recalculated to harmonic orders. HHG is observed for the first time from within an air filament [Voc12c]. In contrast to argon, dynamics do not lead to continuum generation in the high-energy cut-off. Nevertheless, HHG occurs up to order 23 in a modulated manner,
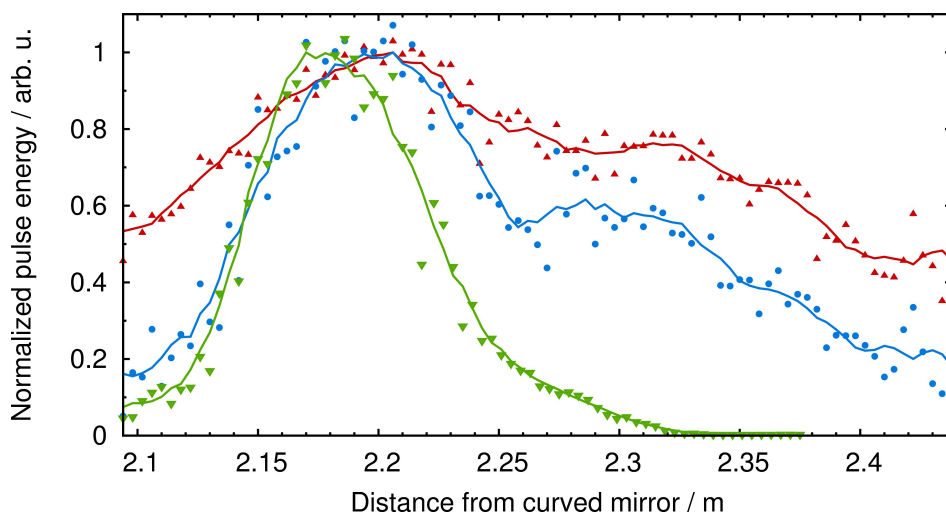

Figure 3.14: Pulse energy after integration of recorded VIS (red), UV (blue) and XUV (green) spectra emerging from a truncated air filament, depending on the point of truncation by means of the distance from the curved mirror. Solid curves are corresponding boxcar average values.
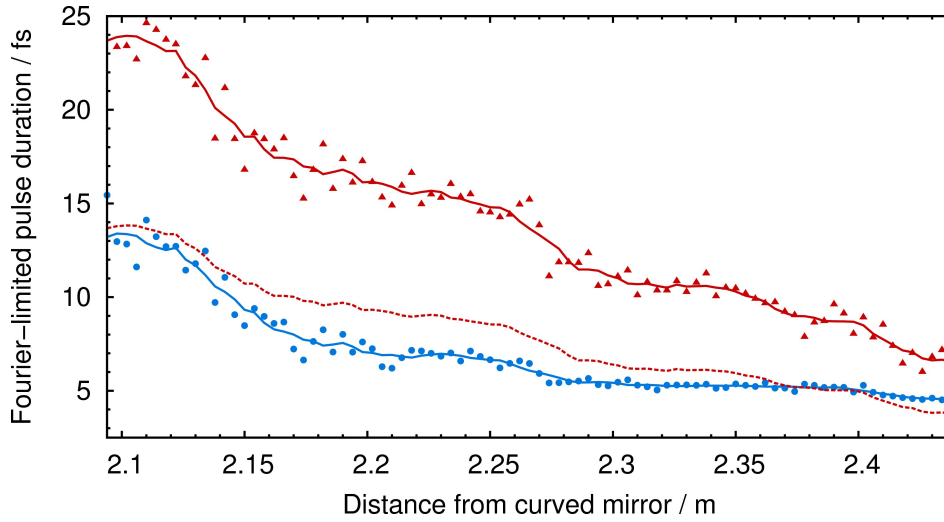
Figure 3.15: Fourier limit of the pulse duration calculated from spectra shown in Section 3.2 and 3.3. The red triangles correspond to the visible spectrum, while the blue dots are calculated from the UV spectrum. Curves represent boxcar average values. The broken red curve is the VIS Fourier limit divided by the square root of the non-linear process' order, $\sqrt{3}$.

indicating a multiple cycle IS near the beginning of the filament. A detailed analysis of this IS requires the combined evaluation of all recorded spectral ranges, as follows in the next section.

3.4.1 Intensity Spikes in an Air Filament

Considering THG and HHG under identical conditions in a filament in 1 bar of air, the integrated pulse energy from recorded spectra gives insight into filamentation dynamics. This is displayed in figure 3.14, calculated from spectral power densities presented in the previous sections. At a propagation distance of 2.21 m the energy of the visible (red curve) and UV (blue curve) radiation reaches its maximum. Both decrease slowly to 50 % and 20 % respectively, at a distance of 2.43 m. In the XUV range, the peak energy integrated over all harmonic orders is found at 2.17 m. From there it undergoes a steep decrease, reaching zero beyond a distance of 2.32 m.

Off-axis contributions are not included in the normalised energy, as they are clipped by the pinhole(s). The initial rising slope is caused by the first pinhole blocking part of the input radiation. With increasing propagation, energy from the reservoir enters the filament and is transmitted through the pinhole, leading to a maximum. Behind the maximum, the visible pulse energy decreases due to plasma absorption and multiphoton absorption [Cou07]. These losses limit the overall length of the filament. XUV radiation is quickly absorbed in
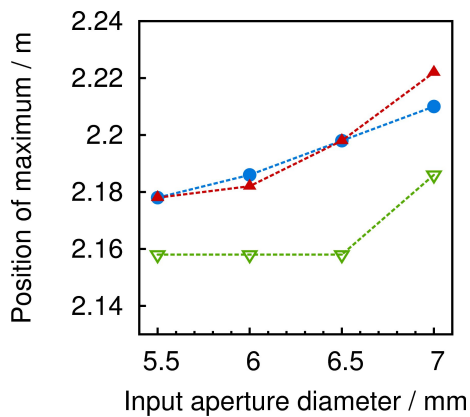
Figure 3.16: Position of the pulse energy maximum after integration of recorded VIS (red), UV (blue) and XUV (green) spectra from an air filament, depending on the input aperture diameter. Broken lines are displayed to support the illustration.

the gas atmosphere of the filament. A typical transmission after $100\,\mu\text{m}$ of propagation is below $1\,\%$ [Hen93]. Hence, the XUV pulse energy (green curve in fig. 3.14) indicates the formation of a single IS well above the clamping intensity. The UV pulse energy (blue curve in fig 3.14) follows qualitatively the visible pulse energy curve, while slopes are steeper due to the third-order non-linear dependence on the VIS pulse energy.

Note, that the absorption length of XUV radiation is not an estimate for resolution of on-axis intensity probing in beam propagation direction. Intensity fluctuations of the input pulses, inevitably present in high power laser systems, lead to a shot-to-shot change of the non-linear focus position. Therefore, the micrometre resolution due to high absorption is blurred by back- and forth shifting of the whole filament.

Figure 3.15 compares the Fourier limit for pulse durations calculated from visible (red curve) and XUV (blue curve) spectra. For comparison, the perturbative estimation (broken red curve) is calculated by dividing the VIS Fourier limit by $\sqrt{3}$. The UV Fourier limit follows this estimation quite well, confirming that the broad UV spectrum originates from the already large bandwidth of the generating pulse. This bandwidth can only contribute to THG if it mainly originates near the truncation point, in vicinity of the pinhole and pressure gradient.

Note that there is a small deviation between the UV Fourier limit and the perturbative estimation. It is most pronounced at the position of the on-axis IS in fundamental intensity. The IS's net energy is too small to observe it in the visible spectrum. Nevertheless, due to high spike intensity, THG occurs with a Fourier limit below the perturbative estimation. In contrast to XUV radiation, UV light is not absorbed and propagates further in the filament. As a result, the Fourier limit saturates at distances behind the on-axis intensity spike. [Voc12c]

3.4.2 Input Aperture Variation

Influence of the input aperture has been briefly discussed in Section 3.2.1 with reference to its impact on multiple-filament formation. The aperture diameter modifies pulse energy and focusing conditions at the same time, both exerting influence on phase-matching. Figure 3.16 shows the positions of pulse energy maxima from figure 3.14 for four different input apertures ranging from 5.5 mm to 7.0 mm. Input pulse energy before the aperture is kept constant and the input power is below the threshold for multiple filaments even for a completely open aperture. In the visible and ultraviolet spectral region (red triangles and blue circles respectively), the maximum shifts towards larger propagation distances with increasing aperture diameter. The XUV maximum position is fairly constant except for a 7 mm aperture opening.

Behaviour of the VIS and UV part is attributed to the earlier onset of plasma defocusing, which is caused by a higher pulse energy behind the aperture for a larger aperture diameter. The influence of aperture-induced focus modification appears to play a minor role for the maximum's position. However, the position of the XUV energy maximum is mainly determined by dynamics of intensity spikes and therefore deviates from the VIS and UV curves.

3.5 High-Pressure Filamentation

In principle, the generation of harmonics directly inside a filament presents an alternative technique for attosecond pulse generation. Current attosecond pulse train (APT) and isolated attosecond pulse (IAP) sources generate XUV radiation in neon and reach a high photon
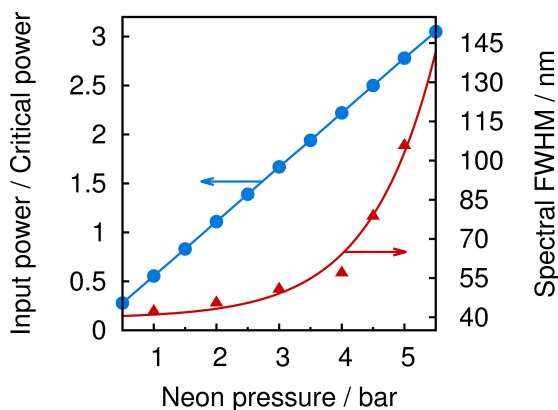

Figure 3.17: Pressure dependence of the spectral broadening in a filament in neon. Red triangles indicate the maximum spectral FWHM generated in a neon filament along the tracked propagation length. Blue dots represent the input power to critical power ratio. The red solid curve is an exponential fit.

energy, as the cut-off scales with the ionisation potential. As a consequence, filamentation and direct HHG is interesting to analyse in a neon atmosphere for photon energy up-scaling.

Unfortunately, the non-linear refractive index of neon,

$$n_2 = 6.78 \cdot 10^{-21}\,\mathrm{cm^2/W} \qquad 1\,\mathrm{bar,\ 293.15\,K,\ 780\,nm} \tag{3.1}$$

is only 7 % of that of argon (calculated according to [Leh85]). Consequently, the critical power P_{cr} is increased by a factor of 13.6, as it scales inversely with n_2. Several steps are taken to compensate for the lower n_2 when switching to neon. Firstly, the laser amplifier repetition rate is lowered from 3 kHz to 1 kHz. This leads to a maximum compressed pulse energy of 2.7 mJ before any aperture. Secondly, neon is used under high pressure conditions up to 5 bar, modifying the effective n_2 and lowering P_{cr}. Both measures are increasing the input power to critical power ratio and, therefore, the ramifications of non-linear propagation. They implicate new technical challenges discussed in Section 3.5.1, but succeed in direct HHG in neon, presented in Section 3.5.2.

3.5.1 Experimental Challenges

Increasing the amplifier system's maximum output pulse energy to 2.7 mJ is technically challenging. Although the system is designed for 1 kHz operation, high pulse power re-
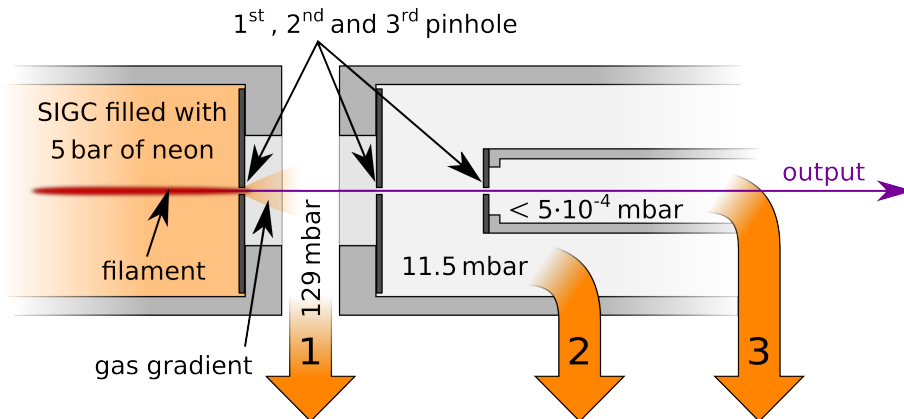

Figure 3.18: Three-pinhole set-up for high-pressure filamentation experiments. Maintaining a pressure below $5 \cdot 10^{-4}$ mbar in the subsequent vacuum chamber, three differential pumping stages are necessary. Stages 1 and 2 are operated with rotating-vane vacuum pumps. The distance between the pinholes is 4.5 mm and 10 mm respectively.

sults in intensities close to the damage threshold of optics used before pulse compression. Nevertheless, stable operation at these output pulse energies is feasible.

With high input energy, visible spectra in neon have been recorded at different pressures. Figure 3.17 shows the maximal achievable spectral FWHM for up to 5 bar (red curve). Clearly, further increase in pressure yields stronger broadening, as no sign of saturation or multiple filament formation is visible at 5 bar. The available pulse energy results in an input power of 77 GW. As a result, the input power to critical power ratio is increased, shown as the blue curve in figure 3.17 versus the gas pressure. A filamentation channel observable by fluorescence perpendicular to the propagation axis emerges at approximately 2 bar, where the power ratio is nearly unity.

In practical use, the high pressure easily results in destruction of a 1 mm thick CaF_2 entrance window. This technical issue can be resolved by an aluminium support, decreasing the effective window diameter to 6 mm, which is slightly more than the beam diameter. However, bending of the window is clearly visible, although its influence on filamentation is not apparent. A double-pinhole set-up is not sufficient to realise a transition to high vacuum
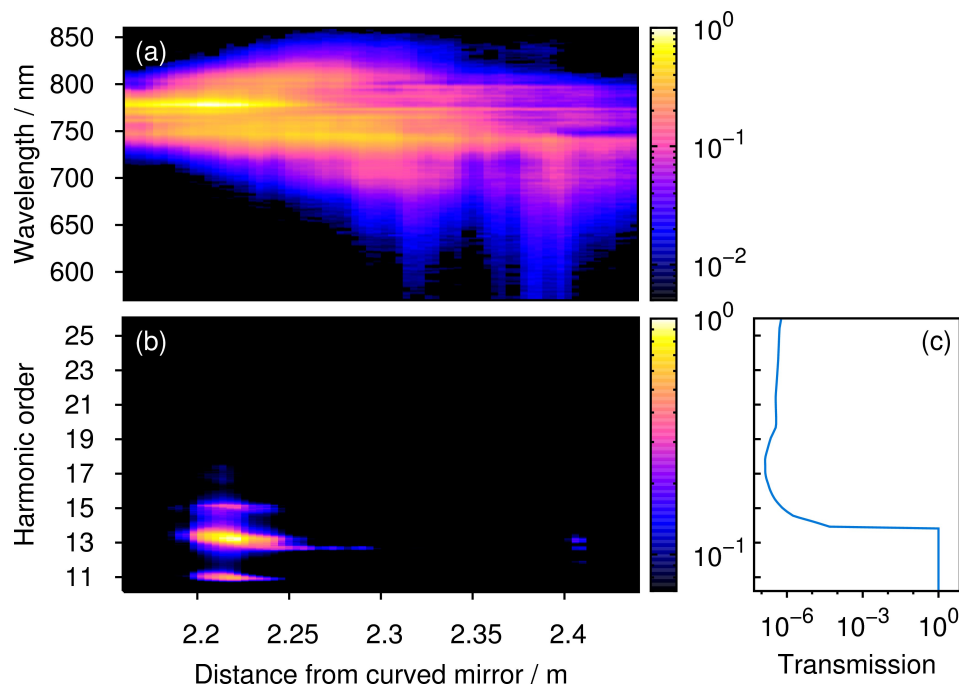

Figure 3.19: Spectra from filamentation in neon under high pressure conditions (5 bar). **(a)** The visible spectrum shows broadening of more than 100 nm FWHM. **(b)** Harmonic orders 11–15 are visible in the XUV spectrum in a limited range of propagation distances. **(c)** Transmission of combined paths in 129 mbar and 11.5 mbar neon between three pinholes; transmission data: [Hen93].

conditions. At 5 bar neon pressure in the SIGC, the first differential pumping stage maintains a pressure of 45 mbar, leaving the turbo-molecular pumps of the second differential stage with a gas load too high for their operation. To be able to operate an XUV spectrometer, a third differential pumping stage was inserted into the set-up, according to figure 3.18.

3.5.2 Results and Discussion

Figure 3.19(a) depicts the visible spectrum evolution of a pulse with 2.3 mJ energy along a filament in 5 bar of neon. Significant broadening is visible, reaching at its maximum a spectral FWHM of 105 nm, which is comparable to the broadening in 1 bar of argon at 0.9 mJ input pulse energy.

Generated XUV radiation is shown in figure 3.19(b). HHG is successfully observed, but limited to a narrow range of propagation distances between 2.19 m and 2.25 m. The maximum harmonic order is 15, several orders below the cut-off observed in air and argon filaments. Calculating from the higher ionisation potential of neon compared to argon and nitrogen, radiation up to 29 nm is expected, corresponding to harmonic order 27.

Due to high pressure and construction of the triple-stage differential pumping, generated radiation has to pass a distance of 4.5 mm in 129 mbar neon, followed by propagation in 10 mm at 11.5 mbar. Absorption of XUV becomes relevant in neon for wavelengths below 57 nm as depicted in figure 3.19(c), which is between harmonic orders 13 and 15. The
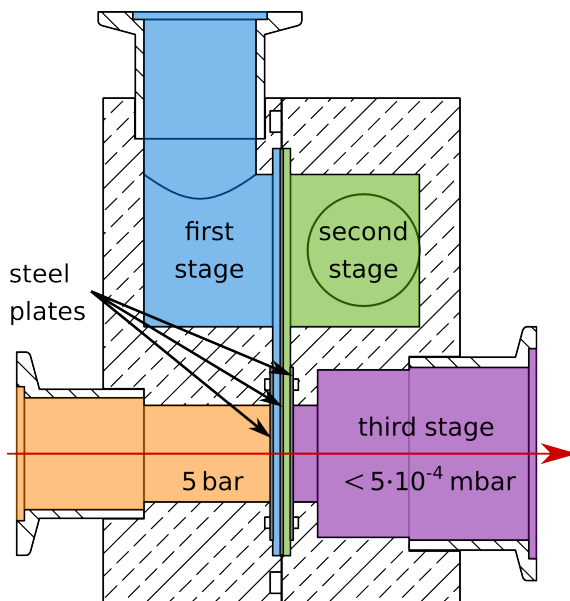

Figure 3.20: Optimised construction of a triple-pinhole set-up. A high-pressure filament propagates in 5 bar of neon (shaded in orange). Differential pumping is realised with rough vacuum pumps in stage one (shaded in blue) and stage two (shaded in green), and turbo-molecular pumps in stage three (shaded in violet). The construction consists of two massive blocks and two spacer, separating three steel plate pinholes by 1.5 mm from each other.

propagation in absorbing gas for several millimetres results in almost complete absorption [Hen93] and causes the limited XUV output in a neon filament.

A solution could be reached by optimising the triple-stage differential pumping design. Minimising the distances beween the pinholes opposes maximising the available space for gas expansion and pumping aperture for fast evacuation. Figure 3.20 shows an optimised design to circumvent the technical limitations of the previously used pinhole arrangement for future experiments. By using an arrangement of three steel plates separated by thin spacer parts, the distance between pinholes is reduced to 1.5 mm for each stage. Transmission is significantly higher for 3 mm propagation length compared to 14.5 mm in the previous set-up. Alternatively, the input energy may be further increased by conducting the experiment with a different laser amplifier system. However, in this case, modulational instabilities are more pronounced and may introduce new challenges.

4

Temporal Characterisation

As described in Section 2.5, many pulse characterisation methods have been developed, each having a unique set of advantages and disadvantages. The characterisation of broadband pulses resulting from filamentation both in the visible and ultraviolet spectral range put strict constraints on the measurement method, namely

- few- or even sub-femtosecond time resolution,

- no frequency up-conversion for absorption reasons,

- optical octave-spanning compatibility,

- minimal amount of induced dispersion.

For this task, we select an implementation of transient grating frequency-resolved optical gating (TG-FROG) which fulfils the requirements and is described below. TG-FROG can be realised in virtually dispersion-free, all-reflective geometries at deep-ultraviolet wavelength, limited only by input wavelength transmission of the non-linear medium. Thin fused silica
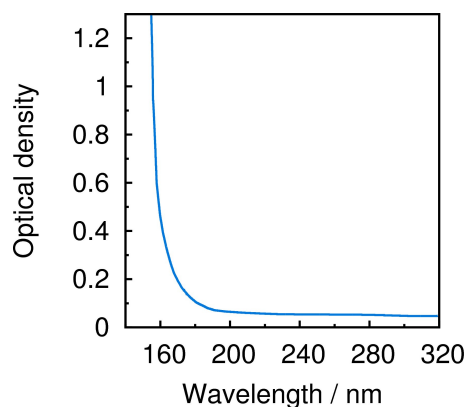
Figure 4.1: Optical density of 1 mm fused silica. Thin fused silica plates adequately transmit UV light above a wavelength of 180 nm. Below 157 nm absorption increases significantly. [Sig71]

plates are well suited as interaction medium and are highly transmissive in the desired spectral range. Figure 4.1 illustrates the corresponding deep-UV absorption edge. Due to a non-collinear geometry, the TG-FROG signal is spatially separated and therefore background-free. However, it is generated in the same spectral range as the input beam, requiring thorough control of stray light.

An overview of the TG-FROG principle of signal and trace generation is given in Section 4.1, describing its spatial chirp and spectral sensitivity. In Section 4.2, an experimental realisation is presented. Results of FROG measurements before and after filamentation are shown in Section 4.3. For future applications, compression of ultraviolet pulses is discussed in Section 4.4.

4.1 Transient Grating FROG

TG-FROG consists of a non-collinear third-order auto-correlation and a subsequent spectrometer, which spectrally resolves the signal. This results in a two-dimensional distribution, also known as a *spectrogram* or FROG-trace. The non-linear process involved is four-wave mixing (FWM), which is an interaction of four photons and their momenta:

$$\omega_{\mathrm{FWM}} = \pm\omega_1 \pm \omega_2 \pm \omega_3 \qquad \mathbf{k}_{\mathrm{FWM}} = \pm\mathbf{k}_1 \pm \mathbf{k}_2 \pm \mathbf{k}_3\,. \qquad (4.1)$$

If all input frequencies ω_i and the output frequency are identical, the process is called degenerated four-wave mixing (DFWM) and transforms to

$$\omega_{\mathrm{DFWM}} = \omega - \omega + \omega = \omega \qquad \mathbf{k}_{\mathrm{DFWM}} = \mathbf{k}_1 - \mathbf{k}_2 + \mathbf{k}_3\,, \qquad (4.2)$$

where one of the electric fields is complex-conjugated, corresponding to a frequency with opposite sign [Trä07]. Consequently, the non-linear polarisation reads

$$\mathscr{P}^{(3)}_{\mathrm{DFWM}} = 6 \cdot \chi^{(3)}_{\mathrm{DFWM}}(\omega;\, \omega,\, -\omega,\, \omega) \cdot E_1(t,r)\, E_2^*(t,r)\, E_3(t,r)\,. \qquad (4.3)$$

Figure 4.2 shows a non-collinear boxcar arrangement of DFWM, in which three incident beams (1–3) located on three corners of a square yield a signal beam emitted in direction of the fourth corner. This process is intrinsically phase-matched due to its geometry and is suitable to generate a FROG-trace. [Li99]
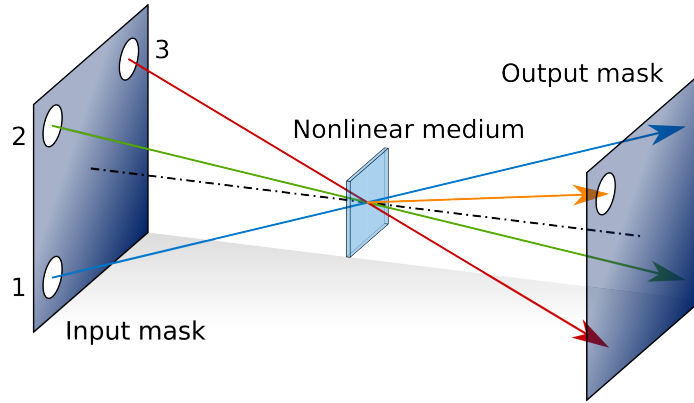
Figure 4.2: DFWM from three input beams (1–3) produces the FROG signal, separated due to momentum conservation in a non-collinear set-up. In dispersion-free TG-FROG configurations, the three beams are generated from one enlarged beam by means of an input mask. A corresponding output mask blocks all input beams and extracts the signal beam.

Moving one of the input beams with respect to the others generates a spectrogram of the form

$$I_{\text{FROG}}^{\text{TG3}}(\omega,\tau) = \left| \int_{-\infty}^{\infty} E_1(t)E_2^*(t)E_3(t-\tau)\,e^{-i\omega t}\,dt \right|^2 , \tag{4.4}$$

where E_i denotes the electric field of input pulses 1–3. In this case, beam no. 3 (see figures 4.2 and 4.3) is delayed by τ. Since all pulses are identical, the expression simplifies to the PG-FROG signal field expression in equation (2.31) in Section 2.5. This requires renaming of variables t to $t-\tau$ and a sign re-definition of τ as $-\tau$ [Tre00]. Experimental FROG-traces in this work are recorded with a time delay in input beam no. 3. The same trace is obtained when delaying beam no. 1. However, when delaying the second beam, the resulting trace is an SD type (see equation (2.30)).

For both SD and PG traces, a phase-retrieval algorithm is readily available, e.g. in Femtosoft Technologies' *Frog3* software. From the reconstructed time-dependent intensity and phase, a pulse duration can be calculated. The retrieved data is used to calculate a FROG-trace, whose comparison to the original trace gives an estimate on the accuracy of the measurement. Additionally, the pulse input spectrum is retrieved and its similarity to an independently measured spectrum serves as a quality criterion for the reconstruction.

However, the described beam geometry allows several other combinations of three photons to form a signal photon. The resulting signal wave-vectors $\mathbf{k}_4$ point in different directions outside the square, as explained in the next section.
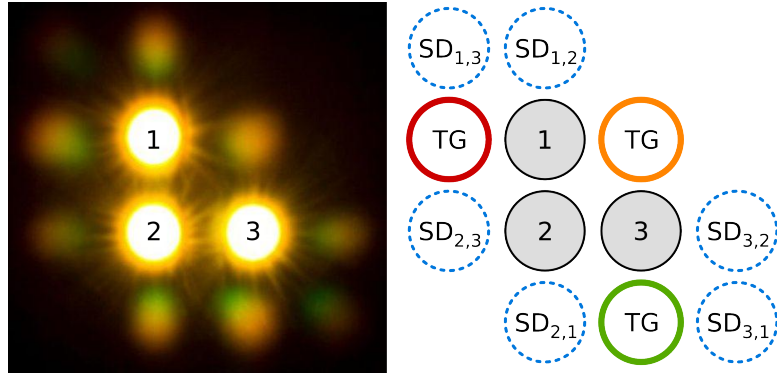
Figure 4.3: Photograph (left) and corresponding diagram (right) of the output beams in non-collinear DFWM, using a pulse with 300 nm bandwidth in the VIS spectral range. The TG signals (orange, red and green circles) are generated by mixing of photons from input beams 1–3 (see text). Mixing between two beams yields SD signals (blue dashed circles) vertically, horizontally and diagonally aligned respectively. Involved input beams are noted as indices. Photo taken at Laser-Laboratorium Göttingen e. V. (LLG).

4.1.1 Self-Diffraction and Transient Gratings

An intuitive picture of the physics behind DFWM is given by the *transient grating* approach. Two beams overlapping in their focal region form an intensity modulation caused by interference. Due to the KERR effect, a diffraction grating is generated by this interference, self-diffracting the two input beams on their own grating. These SD signals are marked with $SD_{a,b}$ in figure 4.3, where a and b denote the two involved input beams. All SD signals are (horizontally, vertically or diagonally) aligned to the corresponding input beams due to momentum addition. For example, the momentum of $SD_{2,3}$ originates from $\mathbf{k}_{SD\,2,3} = \mathbf{k}_2 - \mathbf{k}_2 + \mathbf{k}_3$, using two photons from input beam 2 and one from 3.

If a third beam is involved, the signals marked with TG in figure 4.3 emerge. In the intuitive model, a transient grating from two input beams diffracts the third one. Marked with red and green circled are signals originating from $\mathbf{k}_{TG} = \pm\mathbf{k}_1 + \mathbf{k}_2 \mp \mathbf{k}_3$ respectively. The TG signal marked with an orange circle is used in most experimental approaches, where $\mathbf{k}_{TG} = \mathbf{k}_1 - \mathbf{k}_2 + \mathbf{k}_3$.

4.1.2 Spatial Chirp

Figure 4.3 shows clearly angular dispersion in all signal beams. This is a typical phenomenon of broadband FWM and has its origin in the non-collinear geometry. Strictly observed,
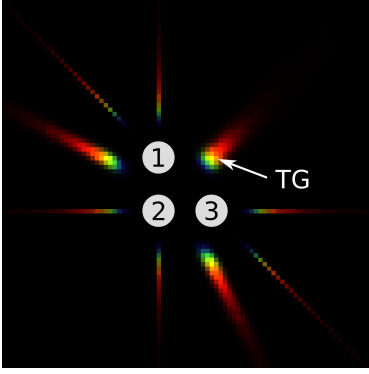
Figure 4.4: Calculation of the resulting signal beams and their spatial chirp on a screen (real colour image, see text). Direction and wavelength of the nine signal beams is calculated via combinations of three input wave-vectors. Wavelength-dependent phase-matching of the third-order non-linear process causes spatial chirp of the signal beams. The image has the same orientation as figure 4.3.

broadband FWM is not frequency-degenerated any more, resulting in imperfect phase-matching. To verify this, a numerical simulation has been used to calculate the wavelength and output k-vector of nine different FWM scenarios possible in this geometry, enumerated by η. The signal wave-vector $\mathbf{k}_4(\eta)$ is calculated according to the coefficients $\xi(\eta,\mathbf{k}_v)$ shown in table 4.1.

$$\mathbf{k}_4(\omega_4, \eta) = \xi(\eta,\mathbf{k}_1) \cdot \mathbf{k}_1 + \xi(\eta,\mathbf{k}_2) \cdot \mathbf{k}_2 + \xi(\eta,\mathbf{k}_3) \cdot \mathbf{k}_3 \tag{4.5}$$

$$\omega_4 = \mathrm{sgn}\big(\xi(\eta,\mathbf{k}_1)\big) \cdot \omega_1 + \mathrm{sgn}\big(\xi(\eta,\mathbf{k}_2)\big) \cdot \omega_2 + \mathrm{sgn}\big(\xi(\eta,\mathbf{k}_3)\big) \cdot \omega_3 \tag{4.6}$$

Here, ω_4 denotes the signal frequency generated by three different input frequencies, and

$$\mathrm{sgn}(x) = \begin{cases} +1 & \text{for } x \geq 0 \\ -1 & \text{for } x < 0 \end{cases} \tag{4.7}$$

is a modified Signum function. The corresponding frequency ω_4 is converted to a real colour according to the CIE_1931 standard [Gui32]. Using three different k-vectors results in a TG signal, while using only two leads to one of the SD-signals.

The calculation reproduces angular dispersion and resulting spatial chirp very accurate, as visible in figure 4.4. Especially the chirp's direction is calculated with excellent agreement to the experimental data. However, focusing of input pulses with a finite circular extent leads to a small range of available input angles, which is not considered by the calculation. As a result, spot sizes are not visible in figure 4.4, which is the reason for SD-signals being thin lines. Spatial spread is only present due to angular dispersion in the signal beams. The grey circles are overlayed indications of the direct beams and do not stem from the calculation. Reproduction of experimental data can be obtained by convolution of the distribution shown in figure 4.4 with an angular spread of the input beams.

Table 4.1: Coefficients $\xi(\eta,\mathbf{k}_i)$ for a signal wave-vector's calculation for nine different FWM scenarios.

η	1	2	3	4	5	6	7	8	9
$\mathbf{k}_1$	-1	1	1	-1	-1	0	2	0	2
$\mathbf{k}_2$	1	-1	1	2	0	-1	-1	2	0
$\mathbf{k}_3$	1	1	-1	0	2	2	0	-1	-1

Recording a complete TG-FROG signal requires to compensate for the angular dispersion of the signal. Otherwise, spectral parts of the signal are omitted and not considered in the measurement, leading to narrower spectra and, in general, to an overestimation of pulse duration. Recent TG-XFROG experiments collimate and recombine the dispersed signal using a lens and a prism pair [Odh12]. However, an exact imaging of the non-linear interaction region onto a spectrometer's input aperture using a curved mirror yields the same result with less effort and losses due to optical surfaces. Keeping track of the signal's centre frequency while scanning the signal beam over the input aperture gives access to remaining spatial chirp, which can be subsequently corrected by altering the imaging distance. The complete signal is now recorded against a temporal delay of one of the input beams, resulting in a spectrogram.
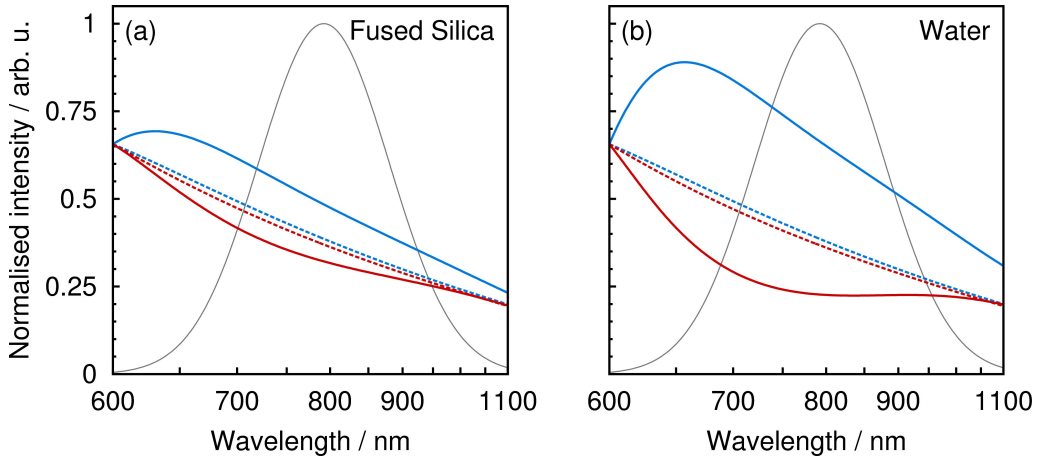

Figure 4.5: Calculation of wavelength dependent spectral sensitivity of TG (blue curves) and SD (red curves) signals in the visible. **(a)** Signals generated 15 μm (broken lines) and 50 μm (solid lines) thick fused silica plates. **(b)** For comparison to [Bal99], generation in a water layer of 20 μm (broken lines) and 100 μm (solid lines) is shown. Grey curves indicate the input spectrum.

4.1.3 Spectral Sensitivity

Although TG-FROG is capable of measuring a signal for a very broad range of input wavelengths, the signal is not completely wavelength-independent, which becomes important for spectra spanning several hundred nanometres. As detailed in [Bal99], the spectral response is dominated by a ω^2-dependence, since the FWM output electric field is given by

$$
\begin{aligned}
\tilde{E}_4(\omega) \propto \quad & \mathrm{i}\frac{c\mu_0\omega L}{2n(\omega)} \cdot \iint \mathrm{d}\omega'\,\mathrm{d}\omega'' \quad \tilde{\chi}^{(3)}(\omega;\omega',\omega'',\omega-\omega''+\omega')\cdot \\
& \tilde{E}_1^*(\omega')\tilde{E}_2(\omega'')\tilde{E}_3(\omega-\omega''+\omega') \cdot \mathrm{sinc}\left(\Delta k_z\frac{L}{2}\right) \cdot \exp\left(\mathrm{i}\Delta k_z\frac{L}{2}\right).
\end{aligned}
\tag{4.8}
$$

Here, ω is the signal frequency, generated by FWM of the input frequencies ω', ω'' and $(\omega-\omega''+\omega')$. The equation expresses the signal electric field $\tilde{E}_4$ and the third-order susceptibility $\tilde{\chi}^{(3)}$ in the frequency domain. Influence of dispersion is incorporated in the refractive index $n(\omega)$ and the crystal length L. Δk_z expresses the phase-mismatch projected onto the z axis. c and μ_0 respectively denote the speed of light in vacuum and magnetic constant.

By taking the absolute square of equation (4.8), the signal intensity $\tilde{I}_4(\omega)$ is calculated. As ω is contained in the pre-factor, the result is depending on ω^2. Other contributions to the spectral response of the TG-FROG process are resulting from phase-mismatch due to dispersion. To obtain a spectral response function, the 'ideal' signal intensity can be calculated according to

$$
\tilde{I}_4^{\mathrm{ideal}}(\omega) \propto \left| \iint \mathrm{d}\omega'\,\mathrm{d}\omega''\tilde{E}_1^*(\omega')\tilde{E}_2(\omega'')\tilde{E}_3(\omega-\omega''+\omega') \right|^2 .
\tag{4.9}
$$

The spectral response is then obtained as the ratio of $\tilde{I}_4(\omega)$ and $\tilde{I}_4^{\mathrm{ideal}}(\omega)$.

Figure 4.5(a) shows the calculated spectral response function for a TG (blue curves) and SD (red curves) process. Dispersion is taken into account for a 15 μm (broken curves) and 50 μm (solid curves) thick fused silica plate. The latter one has been used in experiments. For comparison to [Bal99] results using a thin layer of water are depicted in figure 4.5(b). Solid and broken lines correspond to 100 μm and 20 μm layer thickness respectively. Although results from BALTUŠKA *et al.* seem similar, the layer thickness dependence appears to be off by a factor of five. It is claimed in [Bal99], that the ω^2 dependence is dominant over dispersion influence in the spectral response function, which is a conclusion inconsistent
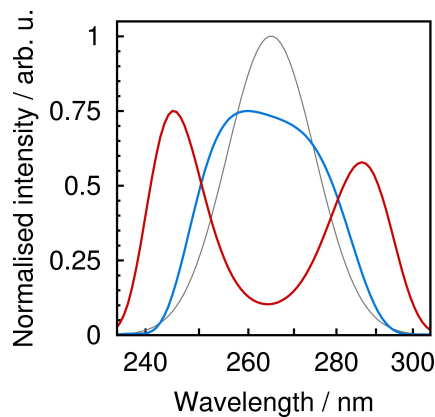
Figure 4.6: Calculation of spectral sensitivity of TG (blue curve) and SD (red curve) signals in case of an UV input spectrum. Signal generation is calculated in a 50 μm thick fused silica plate. The grey curve indicates the input spectrum.

with our results.

Using a UV input spectrum, the spectral response function changes as shown in figure 4.6. While the SD signal (red curve) is pronounced in the spectral wings and weakened in the centre, the TG spectral response follows the spectral shape. This sensitivity should be taken into consideration when reconstructing pulse shapes via TG-FROG, since commercial reconstruction software, such as *Frog3* [Fem12] is implemented for the ideal signal case.

4.2 Experimental Set-Up

Our experimental realisation of a TG-FROG set-up, developed in collaboration with Laser-Laboratorium Göttingen e. V. (LLG) is depicted in figure 4.7. Initially, a copper input mask with three holes of 1.5 mm diameter and 3.0 mm centre distance selects three parts from the
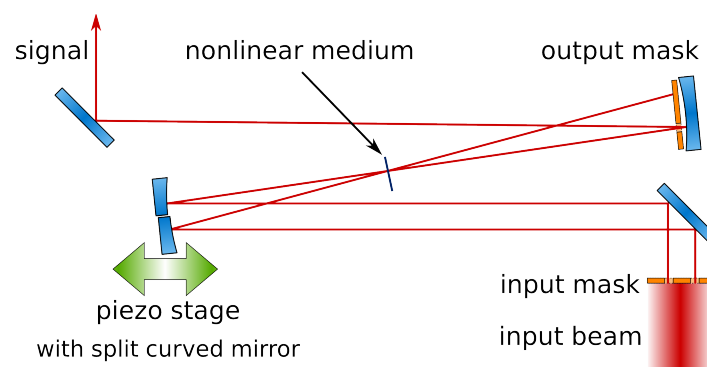

Figure 4.7: Experimental realisation of a TG-FROG device. The input and output masks are manufactured from a 0.5 mm copper plate. To reduce scattering, a layer of black paper is glued to the output mask. The delay is generated via a piezo stage, moving one half of a split focusing mirror. All input beams overlap in the non-linear medium, a 200 μm, 50 μm or 15 μm fused silica plate.
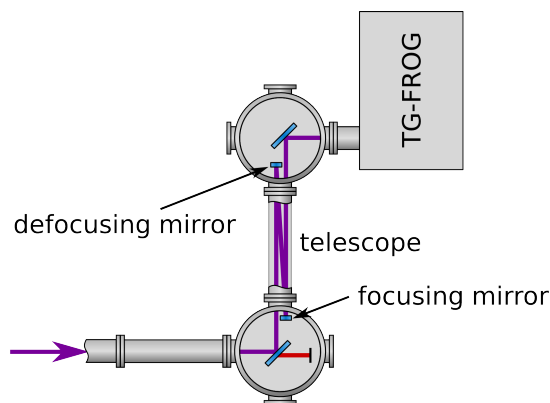
Figure 4.8: TG-FROG set-up behing the filamentation tracking set-up. A homogeneous illumination of the input mask is realised by increase of the beam diameter due to a telescope. It consists of spherical UV-grade aluminium mirrors under small angles.

input beam profile. These are reflected by a flat mirror onto a curved split mirror of 100 mm focal length, focusing all beams into a thin fused silica plate. The separation between input mask and focusing mirror is 245 mm. While one half of the split mirror is mounted on a manual translation stage, the other one is placed on a piezo stage (piezosystems jena, PX 100 CAP), movable by 80 μm. Entering twice in the optical path length, this results in a delay of 534 fs. Depending on the input mask's orientation, one or two of the beams are delayed by the piezo stage with respect to the other(s).

At focus, fused silica plates of diverse thickness (usually 50 μm) can be mounted in a U-shaped holder, slightly tilted downwards to minimise stray light due to back-reflections. The medium's position is variable through a piezo motor-driven linear translation stage (Newport Agilis™ series) in beam propagation direction, in order to adjust for the actual focal length, which is influenced by residual divergence of the input beam.

Behind the focus, a second curved mirror with equal focal length is placed in the beam. The signal beam is selected by an output mask with a square opening of 2 mm × 2 mm. Its size and alignment is critical for the signal-to-noise ratio of the FROG-trace. The optimal position of this mask is at the second focusing mirror, where the spot size and separation is at its maximum. Furthermore, the input mask's beam pattern on the split mirror is directly imaged onto the output mask, minimising diffraction effects. Placing the two curved mirrors at a distance of 220 mm to each other leads to a focus in the signal beam, since the sum of focal lengths is 200 mm. As a result, the second curved mirror images the non-linear interaction region into an appropriate spectrometer.

Throughout the set-up, the mirrors are UV-grade aluminium-coated, i.e. using a magnesium fluoride (MgF_2) protective layer. To avoid deformation due to thermal stress, the split curved mirror is manufactured from two separate plane parts, polished together with identical curvature and coated afterwards. Astigmatic errors caused by spherical curved mirrors are

negligible by virtue of a small angle between incident and reflected beams (4.5° and 6.0° for the first and second curved mirror respectively).

The complete set-up is simple, compact on a 165 mm × 325 mm footprint and virtually dispersion-free. Evacuation of the complete arrangement, fitted into a vacuum chamber, is used to remove dispersion imposed by air. A direct connection to the existing vacuum chamber, origin of the radiation under investigation, is established and depicted in figure 4.8. Transmission windows become unnecessary in this arrangement except for a single output window before the spectrometer. However, this last uncoated fused silica window transmits the low-power TG-FROG signal after its generation and thus does not influence the measurement in any way.

4.3 Results

To verify, that the newly built pulse characterisation set-up is working reliably, FROG-traces of the fundamental pulse at 780 nm centre wavelength are measured. At an optimal compressor setting we obtain a reconstructed pulse duration FWHM of 33 fs. Using a commercial SPIDER set-up (VENTEON Laser Technologies GmbH), we obtain the same result within a tolerance of ±3 %.

TG-FROG-traces of the fundamental pulse are shown in figure 4.9. Different compressor settings were used for these measurements. Figure 4.9(a) shows a negatively chirped pulse, intuitively visible by a tilt of the FROG trace. Positive chirp results in a tilt to the opposite
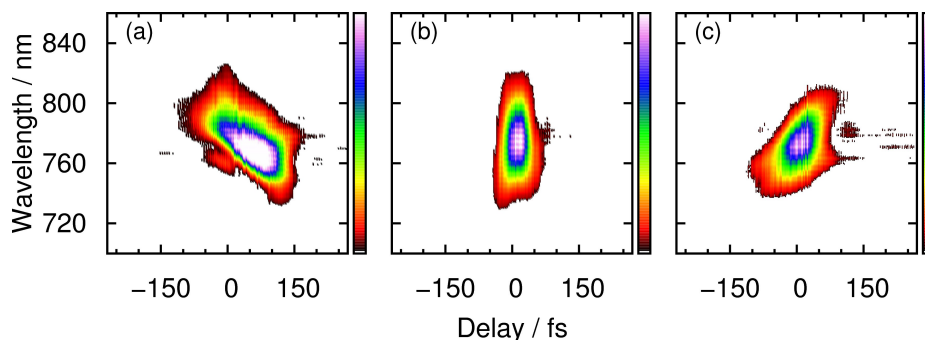

Figure 4.9: TG-FROG-traces of the fundamental pulse with different compressor settings: **(a)** negatively chirped, **(b)** compressed and **(c)** positively chirped pulse. The false colour display encodes the signal intensity, using white for a signal level below 1 %. In all three traces, a residual linear signal can be seen (black horizontal lines) which is removed before reconstruction.
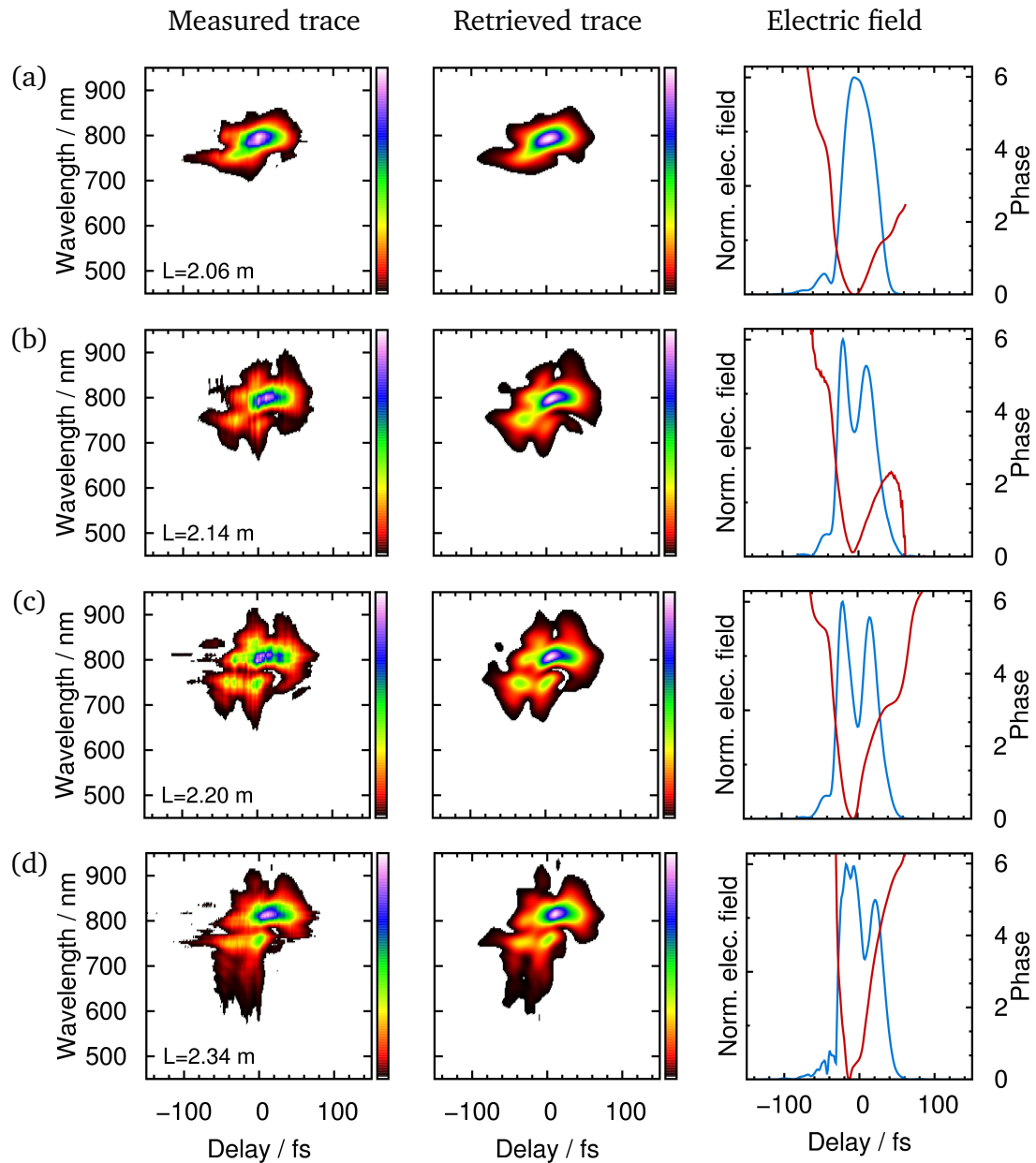
Figure 4.10: TG-FROG-traces of pulses from a filament in air truncated at different positions. The left and centre column respectively show measured and retrieved spectrograms. In the right column, the retrieved electric field strength and its phase are shown. Truncation of the filament is done at position $L = 2.06\,\mathrm{m}$ (a) shortly behind the non-linear focus position, at $L = 2.14\,\mathrm{m}$ (b), at $L = 2.20\,\mathrm{m}$ (c) and after 280 mm filament propagation at $L = 2.34\,\mathrm{m}$ (d). L denotes the distance between the focusing mirror and the pinhole.

direction, displayed in figure 4.9(c). A compressed pulse yields a tilt-free spectrogram, shown in figure 4.9(b).

In figure 4.9, a small signal independent of delay is visible at the centre of the pulse spectrum. This linear signal is removed before phase-retrieval and field reconstruction by various filter techniques, leaving only a signal isolated with respect to the recorded temporal and spectral window.

Pulse Reconstruction after Filamentation

Using a laser pulse of 36 fs duration and 1 mJ pulse energy, a filament is generated in air at 1 bar. The used set-up is displayed in figure 4.8. By removing air from the complete optical set-up and dispensing with any vacuum windows we minimise dispersion for the measured pulse. Recorded spectrograms after truncation of the filament at different positions are displayed in figure 4.10. Figure 4.10(a) shows the measured and reconstructed FROG-trace at an early truncation point, immediately behind the non-linear focus at a distance of 2.06 m from the focusing mirror. The trace is similar to that of the input pulse and results in a pulse duration of 48 fs. In the rightmost graph, the reconstructed electric field envelope and its phase is displayed. Although the temporal profile represents a single pulse with a small pre-pulse, the corresponding phase contains a sharp bend.

Propagating 80 mm inside a filament results in a richer spectrogram, shown in figure 4.10(b). A successful phase-retrieval is achieved and a pulse duration of 54 fs is calculated. Even more complex FROG-traces are generated from filament pulses truncated at 2.20 m (140 mm propagation relative to the first truncation position, fig. 4.10(c)) and 2.34 m (280 mm propagation, fig. 4.10(d)). Reconstruction yields only slightly longer pulses with 57 fs and
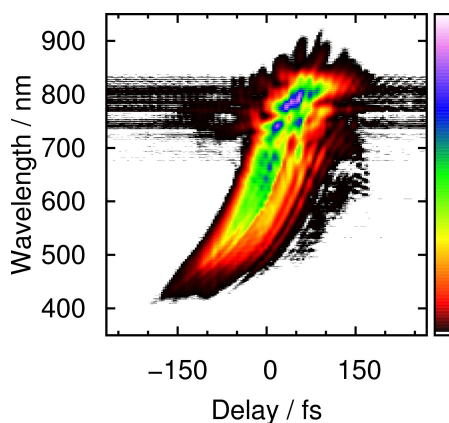

Figure 4.11: TG-FROG-trace of a pulse from a fully propagated filament in 1 bar air. Around 800 nm, a small signal (black) is persistent independently of the delay, i.e. a linear signal. Tilting of the signal shape signifies a linear chirp on the measured pulse. There is also a slight bend in the spectral tail, indicating a small non-linear chirp.

61 fs respectively. Although the FROG error during reconstruction is increasing with pulse complexity, it remains at 0.53 % after 120 iterations.

The temporal structures of pulses from different filamentation lengths clearly show temporal splitting into two pulses, visible in the right-hand graphs in figure 4.10(b), (c). Figure 4.10(d) shows a more complex structured pulse, although the reconstruction is less robust due to the complex trace.

A fully propagated filament is analysed under identical conditions by venting the set-up with air and leaving the pinholes in place. Due to the large interaction length of a full filament, a broad visible spectrum is generated as previously described in Section 3.2. The corresponding FROG-trace is shown in figure 4.11 and contains a short-wavelength tail, representing the generated super-continuum. As a result of the increased propagation length in air, a pulse chirp is clearly visible, delaying the tail of the pulse spectrum. Note, that the bent tail indicates a minor part of additional non-linear chirp.

Ultraviolet Pulse Reconstruction

In Section 3.3, we have shown THG inside filaments with a bright and clean beam profile and a broad spectrum. The TG-FROG set-up is ideally suited to measure these pulses. However, residual fundamental light influences the FWM process. To separate the VIS spectral part from generated UV, we use dichroic mirrors designed for high ultraviolet reflectivity. Nevertheless, the fundamental part is still more intense than THG after two reflections and does not allow to generate a FROG-trace exclusively from the ultraviolet pulse. In future experiments, this issue will be resolved by blocking spectral components in the Fourier plane of a compressor set-up. A suitable compression scheme is presented in the next session.

4.4 Ultraviolet Pulse Compression

The TG-FROG device provides pulse characterisation for pulses that are short and intense enough to generate a signal in a FWM interaction. However, originating from a filament, strong non-linear propagation, filamentation dynamics and gas dispersion are involved in UV pulse generation, likely leading to temporal pulse distortion and chirp. As seen in the previous chapter, the Fourier-limited pulse duration can approach one femtosecond,
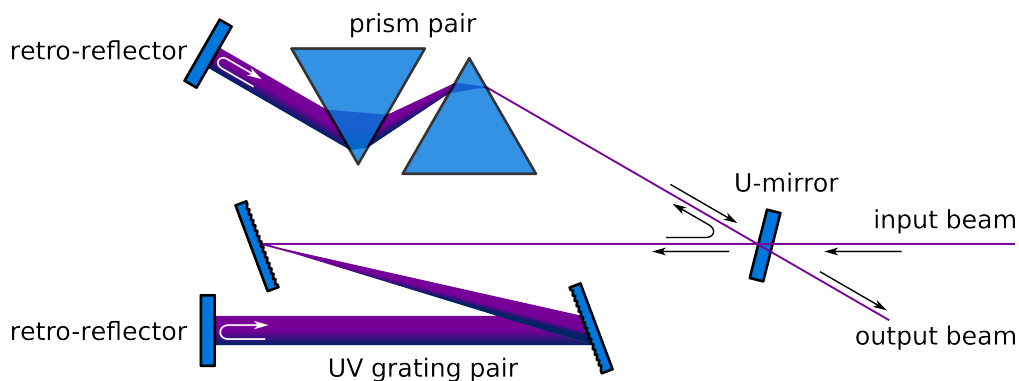
Figure 4.12: Compression scheme for UV pulses. A combination of prisms and gratings permits the compensation of higher order dispersion. For higher transmission, the arrangement can be modified for use with transmission gratings, available for UV radiation.

prospecting high photon-flux generation of sub-femtosecond pulses with a simple scheme. Nevertheless, compression of these pulses is a critical task.

Simple compression schemes using one grating have been realised for ultraviolet broadband pulses down to 8 fs [Dur99; Fuj07]. To be able to compensate for higher order dispersion, it is advisable to add a prism sequence as well, since the sign of its induced third-order dispersion is opposite to that of a grating compressor. Proper configuration of such a hybrid compressor can effectively compensate for both chirp and third-order dispersion of a laser pulse. A combined prism and grating compressor scheme is depicted in figure 4.12. After the input beam is dispersed by a grating pair, it encounters a small change in beam height by a retro-reflecting mirror. The same optical path leads through the grating pair back to a U-shaped mirror. It sends the beam into a prism pair arrangement, levelling the beam back to its original height at the second retro-reflector.

Such a set-up is ideally suited to compensate for the dispersion of a 5 fs ultraviolet pulse (centred at 265 nm) propagating in atmospheric air for several metres. After one metre, such a pulse is already dispersed to more than 50 fs duration. Grating and prism distances remain in the range of 200 mm for a dispersion of $-200\,\mathrm{fs}^2$, qualifying the arrangement to fit in a vacuum chamber. At two positions, the spectral domain is accessible to select parts of the spectrum, e.g. removing the fundamental light or forming an M-shaped spectrum with a part of the visible super-continuum (see also Section 3.3). This resolves the current limitation for UV pulse measurement from filaments.

5

Coherent Diffraction Imaging

The diffraction image of coherent light diffracted by a nanometre-sized object contains considerable information. Coherent diffraction imaging (CDI) is an imaging method to access these information and use them to reconstruct a real image based on an iterative phase-retrieval [Mia03]. Limiting factors on the resolution are, in principle, only the wavelength and largest scattering angles recorded [Cha06a]. Therefore, it is an interesting application for high-order harmonic generation as a source of coherent XUV and soft x-ray radiation.

CDI in the XUV domain requires a high photon flux which is why it has been initially tested at a free-electron laser facility [Cha06b]. The method of image reconstruction via phase-retrieval is described in Section 5.1. Unlike single-shot experiments with intense free-electron laser pulses, illumination of a sample with a laser-based XUV source does not destroy the sample [San07; San08], opening the way for multi-shot and three-dimensional imaging, detailed in Section 5.2. To explore this imaging technique and show its capabilities, we have fabricated several types of samples, specified in Section 5.3.

The required photon flux at a narowband imaging wavelength and a sensitive detection system with high resolution to accomplish spatial oversampling is readily available in the Laserlab Europe collaboration. Therefore, CDI experiments have been conducted in cooperation with the Commissariat à l'énergie atomique et aux énergies alternatives (CEA), Saclay, France, at the Service des Photons, Atomes et Molécules (SPAM) institute in the Ultrafast Coherent Imaging Laboratory. The experimental set-up is described in Section 5.4. Measured diffraction patterns and the reconstruction of real images is discussed in Section 5.5.

5.1 Diffraction Microscopy and Phase Retrieval

A recorded FRAUNHOFER (i.e. far-field) diffraction pattern of the density $f(\mathbf{x})$ of a real sample contains the magnitude of the sample's Fourier transform $F(\mathbf{k})$

$$F(\mathbf{k}) = \int\limits_{-\infty}^{\infty} \mathrm{d}\mathbf{x}\, f(\mathbf{x})\, \mathrm{e}^{2\pi\mathrm{i}\mathbf{k}\cdot\mathbf{x}} \quad . \tag{5.1}$$

In an experiment $F(\mathbf{k})$ is discretely sampled via the pixels of a detector, leading to the discrete form

$$|F(\mathbf{k})| = \left| \sum_{\mathbf{x}=0}^{N-1} f(\mathbf{x})\, \mathrm{e}^{2\pi\mathrm{i}\mathbf{k}\cdot\mathbf{x}/N} \right| . \tag{5.2}$$

We take the absolute values in the above equation, as the phase information is lost in case of a phase-insensitive detection method (which is usually the case). This set of equations needs to be solved for $f(\mathbf{x})$ at each pixel, which is commonly called the *phase problem*. In any case, ambiguities are implicated by a loss of phase in the recording process by means of the following indistinguishable quantities:

$$f(\mathbf{x}), \quad f(\mathbf{x}+\mathbf{x}_0)\, \mathrm{e}^{i\theta_c} \quad \text{and} \quad f^*(-\mathbf{x}+\mathbf{x}_0)\, \mathrm{e}^{i\theta_c} ,$$

where $\mathbf{x}_0$, θ_c are real constants and * donates complex conjugation. These are called the trivial characteristics of $f(\mathbf{x})$ and originate from translation by absolute values and addition of absolute phases. To solve the phase problem, the non-trivial characteristics have to be retrieved [Mia98].

The total number of equations in (5.2) is N^d (where d is the sample dimension), while the number of unknowns is $2N^d$ due to the fact, that each pixel has two variables, namely an amplitude and phase. Solving of this underdetermined set of equations is only possible by adding *a priori* information in form of constraints on equation (5.2).

To have a constraint on the real image, part of the sample needs to be known. Usually, a sample is mounted on a *finite support*, determining the pixel value in this area as zero and effectively reducing the number of unknown pixels. Alternatively, the sample may be free-standing, surrounded by a non-diffracting area. A non-periodic structure has a
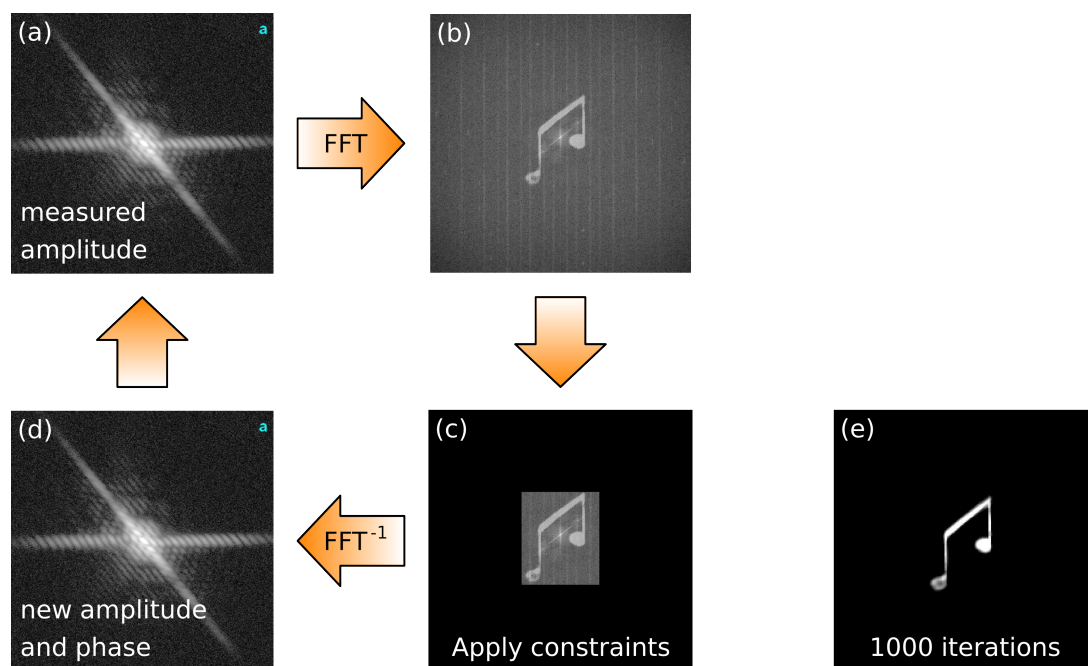
Figure 5.1: Schematic sketch of the 'shrinkwrap' algorithm. **(a)** The measured diffraction image is combined with a random phase. **(b)** A real image is calculated via FFT. **(c)** Constraints on the real image are applied, e.g. a finite support. **(d)** Inverse FFT results in a new phase and amplitude. For the next iteration, constraints in the Fourier domain are applied, e.g. the new amplitude is replaced by the measured one. **(e)** Real image after 1000 iterations. Musical note diffraction and reconstruction by courtesy of CEA SPAM and [Rav09].

continuous diffraction pattern, which can be sampled finer than the corresponding BRAGG peak frequency (i.e. the frequency of a BRAGG pattern emerging if the diffracting structure was crystalline). This leads to another constraint, named *oversampling*, which requires a sufficiently high resolution when recording a diffraction pattern. The real image can be recovered, if the magnitude of a Fourier transform is sampled with a frequency $\sqrt[3]{2}$ times the BRAGG peak frequency and the finite support constraint is sufficiently fulfilled. [Mia98; Mia03]

A first set of algorithms for phase retrieval was suggested by FIENUP, called hybrid input-output (HIO) algorithm [Fie80]. Subsequent development [Fie82; Mia99; Bau02; Fau04] led to a guided hybrid input-output (GHIO) algorithm, also called the 'shrinkwrap' algorithm [Che07], sketched in figure 5.1. Starting from a diffraction pattern (a) with a random phase, a real image (b) is obtained via fast fourier transform (FFT). In real space, constraints are applied to the image, e.g. the 'finite support' constraint is used to set the amplitude of pixels outside the sample area to zero in fig. 5.1(c). Inverse FFT results in a new phase and amplitude diffraction image (d). Now, constraints in the Fourier domain are applied,

where the main constraint is the known diffraction image amplitude. With the old amplitude and new phase, a new iteration is started. In case of sufficient constraints, the algorithm converges towards the reconstruction of a real image. Figure 5.1(e) shows the image reconstruction after 1000 iterations.

Further development of commonly used phase-retrieval algorithms lead to the possibility of three-dimensional image reconstruction from a single or set of two-dimensional diffraction patterns, as detailed in the next section.

5.2 Three-Dimensional Image Reconstruction

Since CDI was first done using an x-ray free-electron laser, only one shot per sample can be used for image reconstruction [Cha06b]. Therefore, obtaining a three-dimensional view of a sample is difficult, necessitating several identical samples. We pursued two aspects in developing of CDI that are of particular scientific interest. Firstly, transfer of the imaging method to laboratory based laser systems enables access for a broader community, removing the limit of free-electron laser availability. Secondly, recording multiple diffraction images of the same object yields an increased signal-to-noise ratio and the possibility of multiple viewing angles. The latter one improves the reconstruction of three-dimensional real images, as I will explain below.

For two-dimensional diffraction patterns, phase-retrieval and reconstruction routinely lead to a two-dimensional real image of the diffracting object. RAINES *et al.* propose a method for reconstructing a three-dimensional structure of an object from a single diffraction pattern, introduced by the name of *ankylography* [Rai10]. It is based on back-projecting the flat recorded diffraction pattern onto the EWALD sphere from where it originates [Cha06a]. Embedding this sphere in a three-dimensional array enables the reconstruction of all elements of the array.

However, there is ongoing discussion on the broad applicability of ankylography, as additional requirements arise [Wei11; Wan11]. In general, it appears to be limited to small objects when reconstructing a three-dimensional image from a single view. The method is greatly improved in its convergence speed and accuracy, if several diffraction patterns from different angles are taken into account, which can be included directly into the reconstruction algorithm [Rai10]. Experiments within this work and sample designs target this special case.

5.3 Sample Design

To create a three-dimensional sample that is well defined, we closely cooperated with
the Laser Zentrum Hannover e. V. (LZH), using two-photon polymerisation (2PP) to write
structures with 200 nm structure size on a glass substrate and coating them afterwards with
a 50 nm layer of gold. Five pillars of 200 nm and 300 nm diameter are placed on top of a
60 μm high pedestal and a pyramidal base according to figure 5.2(a) and (b). Base and
pedestal are necessary to elevate a sample from the surface so a focused Gaussian beam can
pass through the sample without clipping on surface edges of the substrate. This creates a
free-standing sample as can be seen in figure 5.2(c).

Two major problems arise with this sample. While 2PP is in principle capable of 200 nm
structures and less [Lee08], aberrations in the optical manufacturing process and imper-
fections in the photo-chemical excavation of the structure are critical. In particular, high
resolution is only reached with a small overall volume of the manufactured object and a
flexible polymer. As the pedestal is essential for the usability of a sample, a compromise
is made with respect to the resolution. Figures 5.2(d) and (e) show the sample structure
imaged from different angles. The pillars are visibly tilted and not separated from each
other, forming a micrometre-sized structure.

In contrast to previous CDI experiments with opaque samples [Cha06b; San07; Rav09;
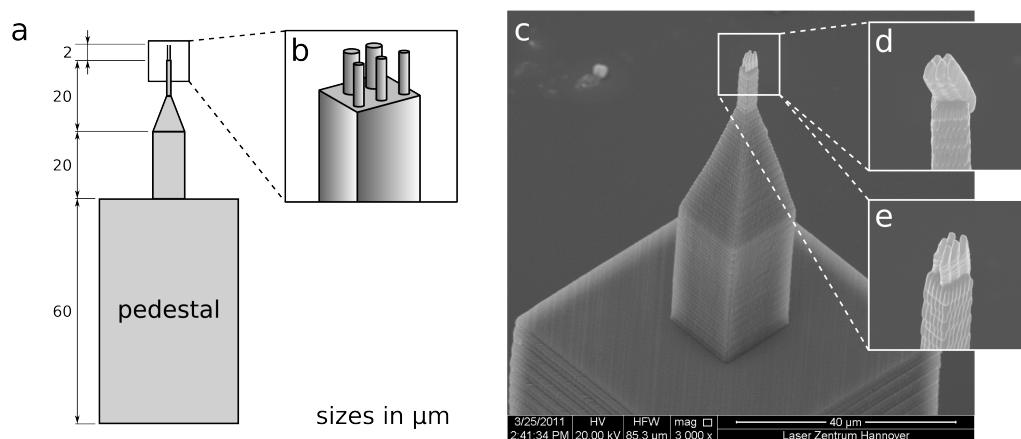Gau10], a free-standing sample transmits most of the direct beam, while only a small part is

Figure 5.2: Nanometer-sized free-standing samples for CDI created by 2PP: **(a)** on a 60 μm
high pedestal, the sample is located on a pyramidal structure. **(b)** the sample itself consists
of five pillars with 200 and 300 nm diameter. **(c)** scanning electron microscopy image of the
real structure. **(d)** and **(e)** show the pillars from different angles. Imperfections due to limited
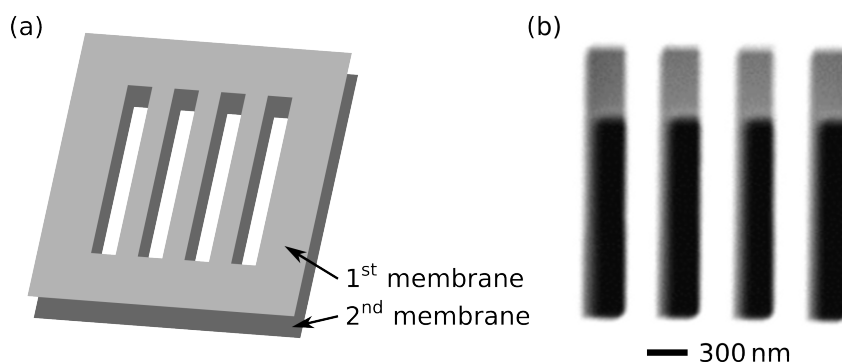resolution and aberrations in the 2PP process are visible.

Figure 5.3: Creating a three-dimensional structure out of two Si_3N_4 membranes. **(a)** Four lines of 300 nm width are milled into two membranes, stacked on top of each other. The FIB process is able to penetrate both layers in one production step. **(b)** Scanning electron microscopy image of the double-membrane sample. A substrate tilt makes the second membrane visible.

blocked. It turned out to be very demanding to record the diffraction pattern with an almost non-attenuated direct beam, even if a wire is used to block the central part. The amount of stray light is significantly increased compared to the use of opaque samples, making a successful reconstruction virtually impossible. A diffraction pattern is shown in Section 5.5, figure 5.8(a).

An alternative to free-standing samples are gold-coated Si_3N_4 membranes, in which nanometre-sized structures are created via focussed ion beam (FIB) milling. Our first attempt to manufacture a three-dimensional sample consist of two membranes stacked on top of each other, separated by a small space. This sample is visible in an electron microscopy image in figure 5.3. Corresponding diffraction patterns and reconstructions are displayed in Section 5.5, figure 5.8(b).

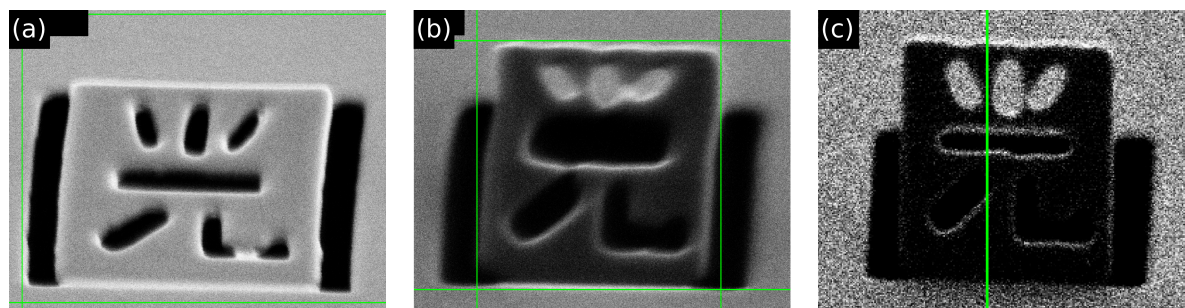By delicate control of the FIB process it is possible to create a three-dimensional structure

Figure 5.4: The chinese symbol for light, etched on a single Si_3N_4 membrane using FIB. Three loose edges enable out-of-plane tilting of the sample. Processing with different FIB intensities yields control of the tilting angle, increasing from (a) to (c).

out of a plane membrane. This is realised e.g. by cutting a rectangular shape where one edge is not completely milled, but the thickness only slightly reduced. Induced surface tension will rise the rectangular shape out of plane, as visible in figure 5.4. Such samples are easy to manufacture and flexible in their size and opacity.

For all kind of samples, special sample holders are integrated into the imaging set-up presented in the next section.

5.4 Experimental Set-Up

CDI experiments at CEA SPAM are conducted at one beamline of the 'LUCA' chirped-pulse amplifier system. It delivers pulses with 30 mJ of energy and a pulse duration of 60 fs from a classical multi-pass amplifier. Before compression in a grating compressor, the chirped pulses are transmitted through an evacuated hollow-core fibre, used as a transversal mode cleaner.

The beamline set-up is sketched in figure 5.6. Compressed pulses are weakly focused by a $f = 5.5$ m lens (L) into a finite gas cell after passing a variable aperture (AP). Length of the cell, gas pressure and gas type can be varied to achieve phase-matching for different harmonic orders. The input power and aperture opening are used to further optimise the generation. Separation of the XUV radiation from fundamental laser light is done by a fused
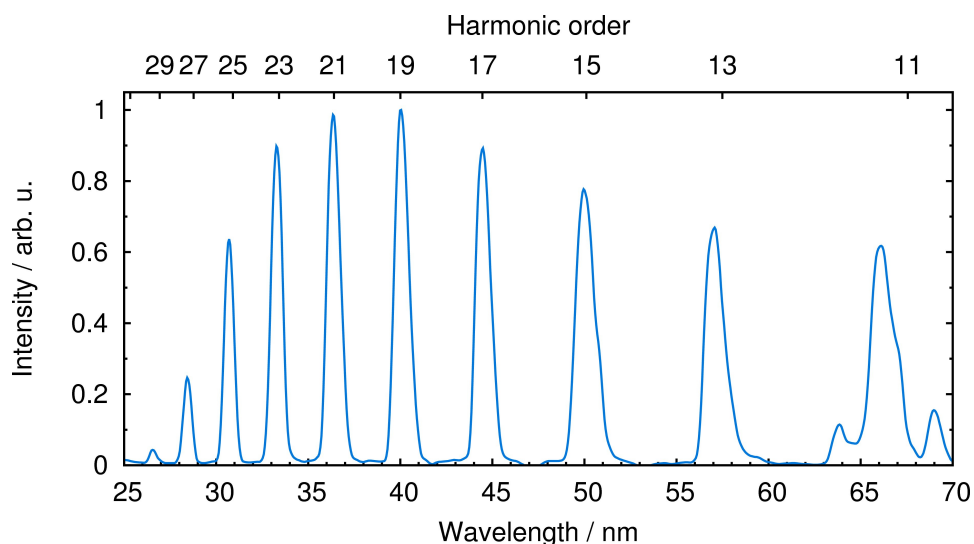

Figure 5.5: HHG spectrum obtained at CEA SPAM in a finite gas cell filled with argon. Harmonic 25 is used for CDI experiments.
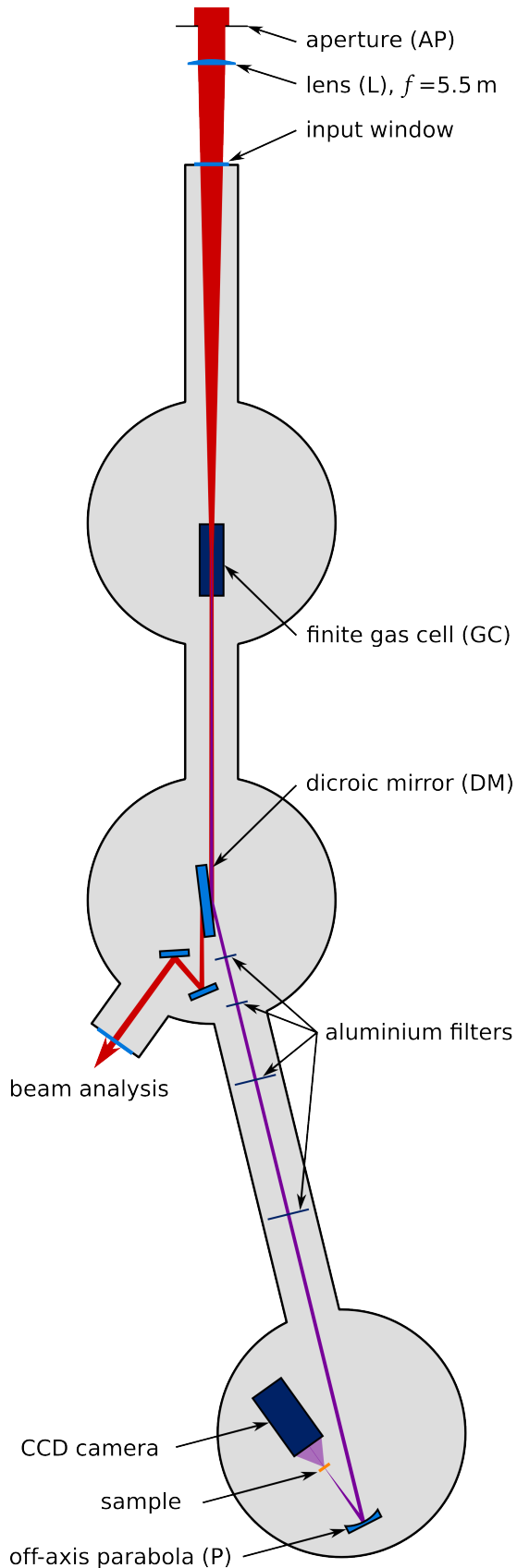
Figure 5.6: Beamline set-up at CEA SPAM. Ti:Sa laser pulses of 60 fs duration and 30 mJ pulse energy are focused into a finite gas cell (GC) using a $f = 5.5$ m lens (L). Inside the gas cell of variable length, argon or neon is used for HHG. The generated radiation is then separated from the driving laser field by a dichroic mirror (DM), transmitting the laser wavelength of 795 nm. Harmonic radiation is reflected due to a small angle of incidence (grazing incidence). Residual laser light is blocked by up to four aluminium filters.

From the harmonic spectrum, harmonic order 25 ($5 \cdot 10^8$ photons/pulse at 32 nm in argon) or harmonic order 39 ($1 \cdot 10^7$ photons/pulse at 20 nm in neon) is focused with an off-axis parabola (P) with a focal length of 22 cm onto the sample. A dielectric coating spectrally selects radiation at the harmonic order of interest. The diffraction pattern is recorded by a CCD camera, located about 15 mm behind the sample.
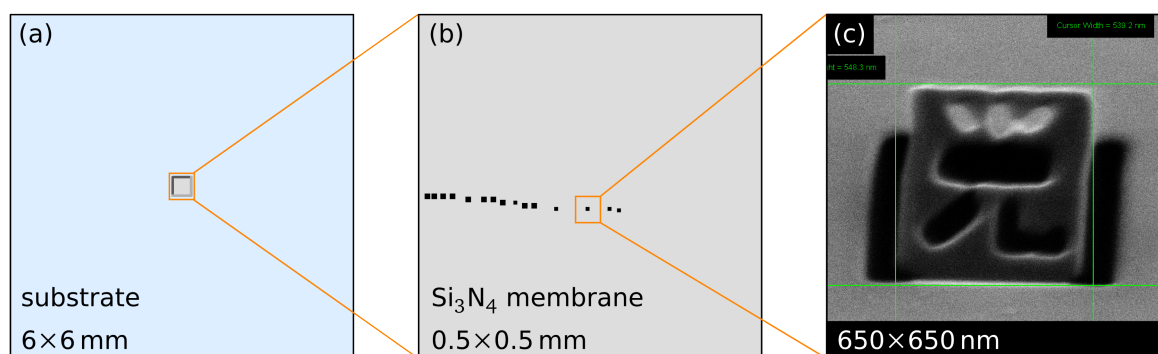
Figure 5.7: Size of a single membrane sample. **(a)** The macroscopic support (the substrate) contains a small area, containing a Si_3N_4 membrane. **(b)** Several sample structures are written into the membrane using FIB milling. **(c)** Scanning microscopy image of a nanometre-sized chinese symbol for *light*. The length of one edge is about 500 nm, the smallest structure is 100 nm wide.

silica plate provided with a dielectric anti-reflex coating. While the input laser wavelength is transmitted, harmonic radiation is reflected in a grazing incidence angle. Up to four carbon-coated aluminium filters (with thicknesses of 100 nm to 300 nm) are used to block residual laser light.

In first experiments, argon is used to efficiently generate 25th harmonic radiation at 32 nm wavelength (39 eV photon energy). A typical harmonic spectrum is displayed in figure 5.5. An off-axis parabola spectrally selects this harmonic order due to a wavelength-selective dielectric coating and focuses it down to a diameter of 5 µm. At focus, $5 \cdot 10^8$ photons/pulse are available for imaging. Later on, radiation at harmonic order 39 is optimised in neon, shifting the imaging wavelength to 20 nm (61 eV) and reducing the available number of photons to $1 \cdot 10^7$ photons/pulse. The spot size is reduced to 3 µm with a parabola of the same focal length, designed for the new wavelength.

For a diffraction pattern of good quality to emerge, it is necessary to position the sample with high precision in the exact focal distance and to centre the focal spot on the sample structure. Additionally, the sample region is small compared to the substrate size, as illustrated in figure 5.7. Therefore, the substrate is mounted on a movable holder, facilitating one axis rotation and three axis translation over a range of centimetres, maintaining a precision and reproducibility of nanometres. Slightly different types of holders are used for free-standing and membrane samples.

Recording a diffraction pattern suitable for real-image reconstruction requires a high-sensitivity, high-resolution detection system. A windowless CCD camera with 2048×2048 pixel (13.7 µm pixel size) at a distance of 15 mm to 20 mm behind the focus detects diffracted
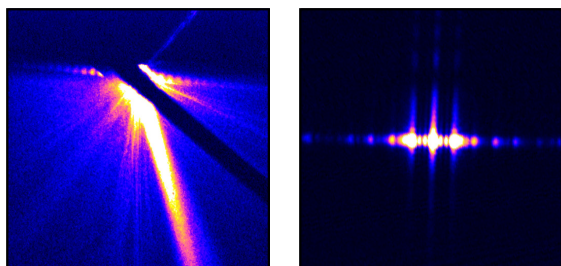
Figure 5.8: Diffraction patterns recorded at 32 nm. **(a)** Free-standing sample with direct beam blocked by a thin wire (diagonal shadow). The striking, almost vertical feature originates from stray light. **(b)** Double-membrane sample. Colour encodes intensity on a logarithmic scale.

radiation. The chip size of 27 mm×27 mm results in a theoretical numerical aperture of $A_N = 0.82$, although a diffraction pattern does not necessarily extend over the full chip.

5.5 Diffraction and Reconstruction

Figure 5.8(a) shows the diffraction image of a free-standing sample. The used sample's scanning electron microscopy image is presented in figure 5.2(c). A thin wire is strained at 45° across the CCD chip to block the direct beam, visible as a diagonal shadow in the top center of the image. As mentioned above, stray light passes the wire and causes an intense feature, tilted 15° from the vertical axis, protruding in the lower half of the image. Containing no information of the sample, this bright feature makes reconstruction of a real image by iterative phase-retrieval virtually impossible.

Using a double-membrane sample, reconstruction is successful. Figure 5.8(b) shows a
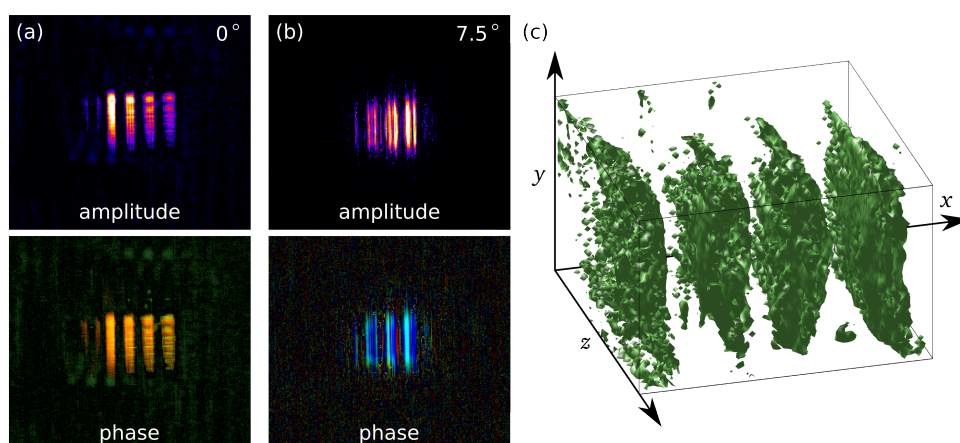

Figure 5.9: Reconstructed images from a double-membrane three-dimensional sample (see fig. 5.3). **(a)** Amplitude and Phase reconstructed via iterative phase retrieval. **(b)** Rotation of 7.5° with respect to the sample angle at which diffraction data for (a) has been taken. **(c)** Ankylographic reconstruction based on diffraction data from two orientations. Reconstructed data by courtesy of F. Wang *et al.*, CEA SPAM.

diffraction pattern from the sample depicted in figure 5.3. Two-dimensional reconstructions of amplitude and phase are shown in Figure 5.9(a) and (b). In case (a), the sample is oriented perpendicular to the beam, so that the rectangular openings of the two membranes overlap. Although the rectangles are well resolved in the retrieved phase, their amplitude is unevenly distributed due to imperfect illumination. The three-dimensional nature of the sample comes into effect at a 7.5° rotation. Due to the rotated view, the patterns on the first and second membrane overlap. Several vertical lines are visible in the corresponding reconstructed image 5.9(b).

Taking both orientations into account, a three-dimensional image can be reconstructed with the help of ankylograhy, which is displayed in figure 5.9(c). The reconstruction represents an inverse image of the source of diffracted radiation. Therefore, green spots are calculated at those points in space where radiation propagates undisturbed, resulting in four cuboids. From the two-dimensional shapes of the membranes, these cuboids can be constructed by connecting the corners of opposing rectangular openings. Projection of figure 5.9(c) to the x-y plane results again in a two-dimensional equivalent under zero degree (as shown in the upper part of figure 5.9(a)).

6

Conclusion

In this work we have shown the spectral properties of filamentation and their evolution along the propagation direction. A new method of truncating a filament has been used to access this previously unavailable evolution, ensuring linear propagation from the point of truncation to the detector. Analysing emission in the visible, ultraviolet (UV) and extreme ultraviolet (XUV) spectral region, a wavelength range of 10 nm to 1000 nm is covered.

Filaments in air and argon induce a high amount of spectral broadening in the visible domain. While the spectral width increases almost linearly during propagation in air, argon results in a more dynamic spectral evolution. Fourier limits of the full width at half maximum (FWHM) pulse duration reach down to 6 fs and 3.5 fs respectively.

Looking at third harmonic generation (THG), a strong influence of the truncation method is visible. A clean, almost Gaussian beam profile is emitted. Compared to the full propagated filament, an on-axis THG signal enhancement of 28 dB (three orders of magnitude) is reached, taking advantage of transient phase-matching in a steep pressure gradient.

THG occurs with a large spectral width, resulting in a monotonic decrease of the pulse duration's Fourier limit during propagation and a final value below 5 fs in an air filament. Using argon, the visible super-continuum extends into UV and creates an M-shaped spectrum consisting of third-order harmonic and the short-wavelengths wing of the fundamental, spanning one octave of optical frequencies. As a consequence, a Fourier limit of 1 fs is calculated from such a spectrum.

We have shown, that high-order harmonic generation (HHG) occurs inside filaments in argon, air and neon at specific points of truncation. Due to a strong non-linearity, HHG can be used as a probe for on-axis intensity. Evolution along the propagation axis is accessible,

since XUV radiation is quickly absorbed in a filament and does only propagate after the point of truncation. A very dynamic evolution in argon is observed, resulting in several spikes in intensity, one of them short enough to produce a continuous harmonic cut-off. In an air filament, an intensity spike is also found and identified as the cause of strong broadening in THG.

Neon has the lowest non-linear refractive index of the used gases, requiring a high pressure and high input power to form a filament at all. At a pressure of 5 bar, HHG is observed for the first time in a neon filament. However, harmonic orders are limited to a narrow spatial and spectral region due to absorption after the point of truncation. A device has been developed to circumvent this technical limitation.

For temporal analysis, a transient grating frequency-resolved optical gating (TG-FROG) device has been developed. The set-up is all-reflective and can be evacuated to remove air dispersion, offering few-femtosecond pulse measurement for wavelengths from near infrared to ultraviolet. Beam splitters have been replaced by masks, cutting parts of the input beam to generate three equal beams. To investigate the spectral response of the transient grating process, simulations of four-wave mixing have been conducted, revealing spectral response functions for the visible and UV spectral region.

An application of HHG is coherent diffraction imaging (CDI), a lensless microscopy technique based on reconstruction of a real image from diffracted radiation. Experiments have been conducted in an international cooperation within the *Laserlab Europe* network, using different types of samples with sub-micrometre sizes. Sample design was aimed at reconstruction of three-dimensional images, therefore creating free-standing samples with two-photon polymerisation (2PP) technology in cooperation with Laser Zentrum Hannover e. V. (LZH). However, these largely transmissive samples result in diffraction patterns containing disturbances due to stray light. Successful reconstruction is prevented by this effect, requiring additional control measures for imaging of free-standing samples, e.g. an imaging aperture. Membrane-based three-dimensional samples have been developed as an alternative in two different designs, a stack of two membranes and an out-of-plane structure on one membrane. With these samples, a newly proposed reconstruction method has been successfully used to obtain three-dimensional information from several diffraction patterns recorded under different angles.

7

Outlook

Several interesting ideas emerged from the research carried out. However, due to limited time, some of them could not be pursued in the scope of this work. In this chapter I give an overview on work currently in progress and future projects.

Filamentation in Neon

As spectral broadening and dynamic intensity spiking in neon depend on P_{cr}, the pressure and input power has been increased in the scope of this work. However, an issue of absorption due to large distances between the pinholes is already technically solved. An immediate step is to conduct measurements with a new triple-stage differential pumping setup presented in Section 3.5.2.

Alternatively, another chirped-pulse amplification system is available, producing up to 50 mJ pulse energy at 10 Hz and 100 fs pulse duration. This scales the input power to critical power ratio further up and may lead to rich dynamics within the filament. Prospects of such an experiment are continuous HHG spectra at a higher frequency cut-off compared to argon and possibly attosecond pulse generation directly from a filament.

Sub-femtosecond Pulse generation

In Section 3.4, a stable continuous XUV spectrum is obtained from an argon filament independent of the non-stabilised input carrier-envelope offset phase (CEP). From our current observation there is no indication that contradict the assumption of an isolated attosecond pulse (IAP) forming inside the filament, caused by a short on-axis intensity spike. Using an electron time-of-flight spectrometer to demonstrate a single sub-femtosecond pulse is work in progress, currently pursued by Martin Kretschmar.

Additionally, THG inside a filament represents an alternative approach to sub-femtosecond pulse generation, since the single optical field cycle at 256 nm is less than one femtosecond. Only low-order frequency conversion processes are involved, resulting in a much higher conversion efficiency compared to conventional IAP. After developing a compression scheme and a TG-FROG pulse characterisation device, both are ready to be applied to visible and UV pulses emerging from the truncated filament, prospecting the generation of a sub-femtosecond pulse of unprecedented pulse energy. Furthermore, a study using these tools yields direct tracking of the temporal evolution of pulses and opens an even deeper insight into the dynamics of filaments. Indication of temporal pulse splitting within a filament has already been seen, and its correlation to spatial pulse splitting and multiple-filament formation could be analysed.

Kerr-Lifetime Measurement

Inspired by the TG-FROG device and the underlying physical process, four-wave mixing (FWM), access to the Kerr effect's lifetime is feasible, i.e. the sustain of the index modification after an excitation pulse has passed. In the UV spectral region, the lifetime is solely defined by the spectral distance of an exciting pulse to the material's band-gap. The filament's broadband UV emission is fixed in its centre wavelength. However, a cooperation with the *Laser Zentrum Hannover* enables us to modify the band-gap of material mixtures by rugate coating technology. With a modified TG-FROG set-up we plan to measure lifetime, magnitude and saturation of the Kerr index modification as a function of the band-gap. This project has already been accepted by DFG as a research grant.

Three-Dimensional Coherent Diffraction Imaging

Since experimental results in CDI have already produced promising three-dimensional reconstructions, a follow-up project is planned in the near future. With the experience gained, useful diffraction image generation and successful reconstruction of real images from a free-standing sample appears feasible. This is a major step in developing HHG-based CDI towards imaging of biological structures, i.e. nannoplankton [And06].

Bibliography

[Akö02]   N. Aközbek, A. Iwasaki, A. Becker, M. Scalora, S. L. Chin, and C. M. Bow-
           den: *Third-Harmonic Generation and Self-Channeling in Air Using High-Power
           Femtosecond Laser Pulses*. Phys. Rev. Lett. **89** (2002), p. 143901.

[Akö03]   N. Aközbek, A. Becker, M. Scalora, S. Chin, and C. Bowden: *Continuum genera-
           tion of the third-harmonic pulse generated by an intense femtosecond IR laser pulse
           in air*. Applied Physics B: Lasers and Optics **77** (2003), pp. 177–183.

[Ale05]   I. Alexeev, A. C. Ting, D. F. Gordon, E. Briscoe, B. Hafizi, and P. Sprangle:
           *Characterization of the third-harmonic radiation generated by intense laser self-
           formed filaments propagating in air*. Opt. Lett. **30**, 12 (2005), pp. 1503–1505.

[Amm86]   M. V. Ammosov, N. B. Delone, and V. P. Krainov: *Tunnel ionization of complex
           atoms and of atomic ions in an alternating electromagnetic field*. Sov. Phys. JETP
           64, 6 (1986), pp. 1191–1194.

[And06]   H. Andruleit, M. Geisen, and S. Stäger: *Stereo-microscopy of coccolithophores-
           modern applications for imaging and morphological analysis*. Journal of Nanno-
           plankton Research **28**, 1 (2006), pp. 1–16.

[Ash76]   N. W. Ashcroft and D. N. Mermin: *Solid state physics*. 1st ed. Brooks Cole, 1976.

[Bal03]   A. Baltuška, T. Udem, M. Uiberacker, M. Hentschel, E. Goulielmakis, C. Gohle,
           R. Holzwarth, V. Yakovlev, A. Scrinzi, T. Hänsch, et al.: *Attosecond control of
           electronic processes by intense light fields*. Nature **421**, 6923 (2003), pp. 611–615.

[Bal97]   P. Balcou, P. Salières, A. L'Huillier, and M. Lewenstein: *Generalized phase-
           matching conditions for high harmonics: The role of field-gradient forces*. Phys.
           Rev. A **55**, 4 (1997), pp. 3204–3210.

[Bal99]   A. Baltuška, M. F. Emde, M. S. Pshenichnikov, and D. A. Wiersma: *Early-Time Dy-
           namics of the Photoexcited Hydrated Electron*. The Journal of Physical Chemistry
           A **103**, 49 (1999), pp. 10065–10082.

[Bau02]   H. H. Bauschke, P. L. Combettes, and D. R. Luke: *Phase retrieval, error reduction
           algorithm, and Fienup variants: a view from convex optimization*. J. Opt. Soc. Am.
           A **19**, 7 (2002), pp. 1334–1345.

[Béj10]   P. Béjot, J. Kasparian, S. Henin, V. Loriot, T. Vieillard, E. Hertz, O. Faucher, B.
           Lavorel, and J. Wolf: *Higher-order Kerr terms allow ionization-free filamentation
           in gases*. Phys. Rev. Lett. **104**, 10 (2010), p. 103903.

[Béj11a]   P. Béjot, E. Hertz, J. Kasparian, B. Lavorel, J. Wolf, and O. Faucher: *Transition
           from Plasma-Driven to Kerr-Driven Laser Filamentation*. Phys. Rev. Lett. **106**, 24
           (2011), p. 243902.

[Béj11b]   P. Béjot, E. Hertz, B. Lavorel, J. Kasparian, J. Wolf, and O. Faucher: *From higher-order Kerr nonlinearities to quantitative modeling of third and fifth harmonic generation in argon*. Opt. Lett. **36**, 6 (2011), pp. 828–830.

[Ber04]   M. Bergh, N. Tîmneanu, and D. van der Spoel: *Model for the dynamics of a water cluster in an x-ray free electron laser beam*. Phys. Rev. E **70** (2004), p. 051904.

[Ber05]   L. Bergé, S. Skupin, G. Méjean, J. Kasparian, J. Yu, S. Frey, E. Salmon, and J. P. Wolf: *Supercontinuum emission and enhanced self-guiding of infrared femtosecond filaments sustained by third-harmonic generation in air*. Phys. Rev. E **71** (2005), p. 016602.

[Ber08]   L. Bergé: *Self-compression of 2 µm laser filaments*. Opt. Express **16**, 26 (2008), pp. 21529–21543.

[Beu10]   M. Beutler, M. Ghotbi, F. Noack, and I. V. Hertel: *Generation of sub-50-fs vacuum ultraviolet pulses by four-wave mixing in argon*. Opt. Lett. **35**, 9 (2010), pp. 1491–1493.

[Bor12]   B. Borchers, C. Brée, S. Birkholz, A. Demircan, and G. Steinmeyer: *Saturation of the all-optical Kerr effect in solids*. Opt. Lett. **37**, 9 (2012), pp. 1541–1543.

[Bra00]   T. Brabec and F. Krausz: *Intense few-cycle laser fields: Frontiers of nonlinear optics*. Rev. Mod. Phys. **72** (2000), pp. 545–591.

[Bra95]   A. Braun, G. Korn, X. Liu, D. Du, J. Squier, and G. Mourou: *Self-channeling of high-peak-power femtosecond laser pulses in air*. Opt. Lett. **20**, 1 (1995), pp. 73–75.

[Bré10]   C. Brée, J. Bethge, S. Skupin, L. Bergé, A. Demircan, and G. Steinmeyer: *Cascaded self-compression of femtosecond pulses in filaments*. New Journal of Physics **12**, 9 (2010), p. 093046.

[Bré11]   C. Brée, A. Demircan, and G. Steinmeyer: *Saturation of the All-Optical Kerr Effect*. Phys. Rev. Lett. **106** (2011), p. 183902.

[Cha06a]   H. N. Chapman, A. Barty, S. Marchesini, A. Noy, S. P. Hau-Riege, C. Cui, M. R. Howells, R. Rosen, H. He, J. C. H. Spence, U. Weierstall, T. Beetz, C. Jacobsen, and D. Shapiro: *High-resolution ab initio three-dimensional x-ray diffraction microscopy*. J. Opt. Soc. Am. A **23**, 5 (2006), pp. 1179–1200.

[Cha06b]   H. N. Chapman, A. Barty, M. J. Bogan, S. Boutet, M. Frank, S. P. Hau-Riege, S. Marchesini, B. W. Woods, S. Bajt, W. H. Benner, et al.: *Femtosecond diffractive imaging with a soft-X-ray free-electron laser*. Nature Physics **2**, 12 (2006), pp. 839–843.

[Cha97]   Z. Chang, A. Rundquist, H. Wang, M. Murnane, and H. Kapteyn: *Generation of coherent soft X rays at 2.7 nm using high harmonics*. Phys. Rev. Lett. **79**, 16 (1997), pp. 2967–2970.

[Che07]   C.-C. Chen, J. Miao, C. W. Wang, and T. K. Lee: *Application of optimization technique to noncrystalline x-ray diffraction microscopy: Guided hybrid input-output method*. Phys. Rev. B **76** (2007), p. 064113.

[Che10]   Y.-H. Chen, S. Varma, T. M. Antonsen, and H. M. Milchberg: *Direct Measurement of the Electron Density of Extended Femtosecond Laser Pulse-Induced Filaments*. Phys. Rev. Lett. **105** (2010), p. 215005.

[Chi64]   R. Y. Chiao, E. Garmire, and C. H. Townes: *Self-Trapping of Optical Beams*. Phys. Rev. Lett. **13**, 15 (1964), pp. 479–482.

[Cor07]   P. B. Corkum and F. Krausz: *Attosecond science*. Nature Physics **3**, 6 (2007), pp. 381–387.

[Cor93]   P. B. Corkum: *Plasma perspective on strong field multiphoton ionization*. Phys. Rev. Lett. **71** (1993), pp. 1994–1997.

[Cor94]   P. B. Corkum, N. H. Burnett, and M. Y. Ivanov: *Subfemtosecond pulses*. Opt. Lett. **19**, 22 (1994), pp. 1870–1872.

[Cou05]   A. Couairon, M. Franco, A. Mysyrowicz, J. Biegert, and U. Keller: *Pulse self-compression to the single-cycle limit by filamentation in a gas with a pressure gradient*. Opt. Lett. **30**, 19 (2005), pp. 2657–2659.

[Cou06]   A. Couairon, J. Biegert, C. P. Hauri, W. Kornelis, F. W. Helbing, U. Keller, and A. Mysyrowicz: *Self-compression of ultra-short laser pulses down to one optical cycle by filamentation*. Journal of Modern Optics **53**, 1-2 (2006), pp. 75–85.

[Cou07]   A. Couairon and A. Mysyrowicz: *Femtosecond filamentation in transparent media*. Physics reports **441**, 2-4 (2007), pp. 47–189.

[Daw69]   E. Dawes and J. Marburger: *Computer studies in self-focusing*. Physical Review **179** (1969), pp. 862–868.

[Dur93]   C. G. Durfee and H. M. Milchberg: *Light pipe for high intensity laser pulses*. Phys. Rev. Lett. **71** (1993), pp. 2409–2412.

[Dur99]   C. G. Durfee III, S. Backus, H. C. Kapteyn, and M. M. Murnane: *Intense 8-fs pulse generation in the deep ultraviolet*. Opt. Lett. **24**, 10 (1999), pp. 697–699.

[Ebe91]   J. Eberly, J. Javanainen, and K. Rzążewski: *Above-threshold ionization*. Physics Reports **204**, 5 (1991), pp. 331 –383.

[Eck08]   P. Eckle, M. Smolarski, P. Schlup, J. Biegert, A. Staudte, M. Schöffler, H. Muller, R. Dörner, and U. Keller: *Attosecond angular streaking*. Nature Physics **4**, 7 (2008), pp. 565–570.

[Fau04]   H. M. L. Faulkner and J. M. Rodenburg: *Movable Aperture Lensless Transmission Microscopy: A Novel Phase Retrieval Algorithm*. Phys. Rev. Lett. **93** (2004), p. 023903.

[Fem12]   Femtosoft Technologies: *Frog3*. http://www.femtosoft.biz/. 2012.

[Fer88]   M. Ferray, A. L'Huillier, X. F. Li, L. A. Lompre, G. Mainfray, and C. Manus: *Multiple-harmonic conversion of 1064 nm radiation in rare gases*. Journal of Physics B: Atomic, Molecular and Optical Physics **21**, 3 (1988), p. L31.

[Fib00]   G. Fibich and A. Gaeta: *Critical power for self-focusing in bulk media and in hollow waveguides*. Optics Letters **25**, 5 (2000), pp. 335–337.

[Fie80]   J. Fienup: *Iterative method applied to image reconstruction and to computer-generated holograms*. Opt. Eng. **19**, 3 (1980), pp. 297–305.

[Fie82]   J. R. Fienup: *Phase retrieval algorithms: a comparison*. Appl. Opt. **21**, 15 (1982), pp. 2758–2769.

[Fra61]   P. A. Franken, A. E. Hill, C. W. Peters, and G. Weinreich: *Generation of Optical Harmonics*. Phys. Rev. Lett. **7**, 4 (1961), pp. 118–119.

[Fre91]   R. R. Freeman and P. H. Bucksbaum: *Investigations of above-threshold ionization using subpicosecond laser pulses*. Journal of Physics B: Atomic, Molecular and Optical Physics **24**, 2 (1991), p. 325.

[Fuj07]   T. Fuji, T. Horio, and T. Suzuki: *Generation of 12 fs deep-ultraviolet pulses by four-wave mixing through filamentation in neon gas*. Opt. Lett. **32**, 17 (2007), pp. 2481–2483.

[Gaa09]   M. B. Gaarde and A. Couairon: *Intensity Spikes in Laser Filamentation: Diagnostics and Application*. Phys. Rev. Lett. **103** (2009), p. 043901.

[Gau10]   D. Gauthier, M. Guizar-Sicairos, X. Ge, W. Boutu, B. Carré, J. R. Fienup, and H. Merdji: *Single-shot Femtosecond X-Ray Holography Using Extended References*. Phys. Rev. Lett. **105** (2010), p. 093901.

[Gho11]   M. Ghotbi, P. Trabs, and M. Beutler: *Generation of high-energy, sub-20-fs pulses in the deep ultraviolet by using spectral broadening during filamentation in argon*. Opt. Lett. **36**, 4 (2011), pp. 463–465.

[Gou08]   E. Goulielmakis, M. Schultze, M. Hofstetter, V. S. Yakovlev, J. Gagnon, M. Uiberacker, A. L. Aquila, E. M. Gullikson, D. T. Attwood, R. Kienberger, F. Krausz, and U. Kleineberg: *Single-Cycle Nonlinear Optics*. Science **320**, 5883 (2008), pp. 1614–1617.

[Gui32]   J. Guild: *The Colorimetric Properties of the Spectrum*. English. Philosophical Transactions of the Royal Society of London, Series A **230** (1932), pp. 149–187.

[Hau04]   S. P. Hau-Riege, R. A. London, and A. Szoke: *Dynamics of biological molecules irradiated by short x-ray pulses*. Phys. Rev. E **69** (2004), p. 051906.

[Hen01]   M. Hentschel, R. Kienberger, C. Spielmann, G. A. Reider, N. Milosevic, T. Brabec, P. Corkum, U. Heinzmann, M. Drescher, and F. Krausz: *Attosecond metrology*. Nature **414**, 6863 (2001), pp. 509–513.

[Hen93]   B. Henke, E. Gullikson, and J. Davis: *X-ray interactions: photoabsorption, scattering, transmission, and reflection at E= 50-30,000 eV, Z= 1-92*. Atomic data and nuclear data tables **54**, 2 (1993), pp. 181–342.

[Iac98]   C. Iaconis and I. Walmsley: *Spectral phase interferometry for direct electric-field reconstruction of ultrashort optical pulses*. Opt. Lett. **23**, 10 (1998), pp. 792–794.

[Jur04]   Z. Jurek, G. Faigel, and M. Tegze: *Dynamics in a cluster under the influence of intense femtosecond hard X-ray pulses*. The European Physical Journal D-Atomic, Molecular, Optical and Plasma Physics **29**, 2 (2004), pp. 217–229.

[Kan93]   D. Kane and R. Trebino: *Characterization of arbitrary femtosecond pulses using frequency-resolved optical gating*. Quantum Electronics, IEEE Journal of **29**, 2 (1993), pp. 571–579.

[Kas00]   J. Kasparian, R. Sauerbrey, and S. Chin: *The critical laser intensity of self-guided light filaments in air*. Applied Physics B: Lasers and Optics **71** (2000), pp. 877–879.

[Kel65]   L. V. Keldysh: *Ionization in the field of a strong electromagnetic wave*. Sov. Phys. JETP **20** (1965), pp. 1307–1314.

[Kid10]   Y. Kida, J. Liu, T. Teramoto, and T. Kobayashi: *Sub-10 fs deep-ultraviolet pulses generated by chirped-pulse four-wave mixing*. Opt. Lett. **35**, 11 (2010), pp. 1807–1809.

[Köh12]   C. Köhler, R. Guichard, E. Lorin, S. Chelkowski, A. D. Bandrauk, L. Bergé, and S. Skupin: *Higher order Kerr terms vs. plasma: Saturation of the nonlinear refractive*. DPG Frühjahrstagung Stuttgart. 2012.

[Kol04]   M. Kolesik and J. V. Moloney: *Nonlinear optical pulse propagation simulation: From Maxwell's to unidirectional equations*. Phys. Rev. E **70** (2004), p. 036604.

[Kol10a]   M. Kolesik, D. Mirell, J.-C. Diels, and J. V. Moloney: *On the higher-order Kerr effect in femtosecond filaments*. Opt. Lett. **35**, 21 (2010), pp. 3685–3687.

[Kol10b]   M. Kolesik, E. Wright, and J. Moloney: *Femtosecond filamentation in air and higher-order nonlinearities*. Optics letters **35**, 15 (2010), pp. 2550–2552.

[Kol12]   M. Kolesik, J. Brown, E. Wright, and J. Moloney: *On the relative roles of higher-order nonlinearity and ionization in ultrafast light-matter interactions*. Opt. Lett. **accepted** (2012),

[Kos08a]   K. Kosma, S. Trushin, W. Schmid, and W. Fuß: *Vacuum ultraviolet pulses of 11 fs from fifth-harmonic generation of a Ti: sapphire laser*. Optics letters **33**, 7 (2008), pp. 723–725.

[Kos08b]   K. Kosma, S. A. Trushin, W. Fuß, and W. E. Schmid: *Characterization of the supercontinuum radiation generated by self-focusing of few-cycle 800 nm pulses in argon*. Journal of Modern Optics **55**, 13 (2008), pp. 2141–2177.

[Kos11]   O. Kosareva, J.-F. Daigle, N. Panov, T. Wang, S. Hosseini, S. Yuan, G. Roy, V. Makarov, and S. L. Chin: *Arrest of self-focusing collapse in femtosecond air filaments: higher order Kerr or plasma defocusing?* Opt. Lett. **36**, 7 (2011), pp. 1035–1037.

[LaF00]   B. La Fontaine, D. Comtois, C. Chien, A. Desparois, F. Génin, G. Jarry, T. Johnston, J. Kieffer, F. Martin, R. Mawassi, et al.: *Guiding large-scale spark discharges with ultrashort pulse laser filaments*. Journal of Applied Physics **88** (2000), p. 610.

[Lan98]   H. R. Lange, A. Chiron, J.-F. Ripoche, A. Mysyrowicz, P. Breger, and P. Agostini: *High-Order Harmonic Generation and Quasiphase Matching in Xenon Using Self-Guided Femtosecond Pulses*. Phys. Rev. Lett. **81** (1998), pp. 1611–1613.

[Lar98]   S. Larochelle, A. Talebpour, and S. Chin: *Coulomb effect in multiphoton ionization of rare-gas atoms*. Journal of Physics B: Atomic, Molecular and Optical Physics **31** (1998), p. 1215.

[Lee08]   K.-S. Lee, R. H. Kim, D.-Y. Yang, and S. H. Park: *Advances in 3D nano/microfabrication using two-photon initiated polymerization*. Progress in Polymer Science **33**, 6 (2008), pp. 631 –681.

[Leh85]   H. Lehmeier, W. Leupacher, and A. Penzkofer: *Nonresonant third order hyperpolarizability of rare gases and N2 determined by third harmonic generation*. Optics Communications **56**, 1 (1985), pp. 67–72.

[Lew94]   M. Lewenstein, P. Balcou, M. Y. Ivanov, A. L'Huillier, and P. B. Corkum: *Theory of high-harmonic generation by low-frequency laser fields*. Phys. Rev. A **49** (1994), pp. 2117–2132.

[LHu91]   A. L'Huillier, K. H. Schafer, and K. C. Kulander: *Theoretical aspects of intense field harmonic generation*. J. Phys. B: At. Mol. Opt. Phys. **24** (1991), pp. 3315–3341.

[Li99]   M. Li, J. P. Nibarger, C. Guo, and G. N. Gibson: *Dispersion-free Transient-grating Frequency-resolved Optical Gating*. Appl. Opt. **38**, 24 (1999), pp. 5250–5253.

[Liu11]   Y. Liu, M. Durand, A. Houard, B. Forestier, A. Couairon, and A. Mysyrowicz: *Efficient generation of third harmonic radiation in air filaments: A revisit*. Optics Communications **284**, 19 (2011), pp. 4706 –4713.

[Liu12]   Z. Liu, P. Ding, Y. Shi, X. Lu, S. Sun, X. Liu, Q. Liu, B. Ding, and B. Hu: *Control of third harmonic generation by plasma grating generated by two noncollinear IR femtosecond filaments*. Opt. Express **20**, 8 (2012), pp. 8837–8847.

[Loc09]   R. A. Loch: *High harmonic generation and ion acceleration with high-intensity laser pulses*. PhD thesis. Enschede: University of Twente, 2009.

[Lor09]   V. Loriot, E. Hertz, O. Faucher, and B. Lavorel: *Measurement of high order Kerr refractive index of major air components*. Opt. Express **17**, 16 (2009), pp. 13429–13434.

[Lor10]   V. Loriot, E. Hertz, O. Faucher, and B. Lavorel: *Measurement of high order Kerr refractive index of major air components: erratum*. Opt. Express **18**, 3 (2010), pp. 3011–3012.

[Lor11]   V. Loriot, P. Béjot, W. Ettoumi, Y. Petit, J. Kasparian, S. Henin, E. Hertz, B. Lavorel, O. Faucher, and J. Wolf: *On negative higher-order Kerr effect and filamentation*. Laser Physics **21** (2011), pp. 1319–1328.

[Lor12]   E. Lorin and A. Bandrauk: *Efficient and Accurate Numerical Modeling of a Micro-Macro Nonlinear Optics Model for Intense and Short Laser Pulses*. Journal of Computational Science (2012).

[Mac93]   J. Macklin, J. Kmetec, and C. Gordon III: *High-order harmonic generation using intense femtosecond pulses*. Phys. Rev. Lett. **70**, 6 (1993), pp. 766–769.

[Mai60]   T. H. Maiman: *Stimulated Optical Radiation in Ruby*. Nature **187**, 4736 (1960), pp. 493–494.

[Mar75]   J. H. Marburger: *Self-focusing: Theory*. Prog. Quant. Electr. **4**, Part 1 (1975), pp. 35 –110.

[May12]   H. C. Mayer and R. Krechetnikov: *Walking with coffee: Why does it spill?* Phys. Rev. E **85** (2012), p. 046117.

[McP87]   A. McPherson, G. Gibson, H. Jara, U. Johann, T. S. Luk, I. A. McIntyre, K. Boyer, and C. K. Rhodes: *Studies of multiphoton production of vacuum-ultraviolet radiation in the rare gases*. J. Opt. Soc. Am. B **4**, 4 (1987), pp. 595–601.

[Méc04]   G. Méchain, A. Couairon, Y. André, C. D'amico, M. Franco, B. Prade, S. Tzortzakis, A. Mysyrowicz, and R. Sauerbrey: *Long-range self-channeling of infrared laser pulses in air: a new propagation regime without ionization*. Applied Physics B: Lasers and Optics **79**, 3 (2004), pp. 379–382.

[Méc05]   G. Méchain, C. D'Amico, Y. B. André, S. Tzortzakis, M. Franco, B. Prade, A. Mysyrowicz, A. Couairon, E. Salmon, and R. Sauerbrey: *Range of plasma filaments created in air by a multi-terawatt femtosecond laser*. Optics Communications **247**, 1-3 (2005), pp. 171–180.

[Méj04]   G. Méjean, J. Kasparian, J. Yu, S. Frey, E. Salmon, and J. Wolf: *Remote detection and identification of biological aerosols using a femtosecond terawatt lidar system*. Applied Physics B: Lasers and Optics **78**, 5 (2004), pp. 535–537.

[Méj06]   G. Méjean, J. Kasparian, J. Yu, S. Frey, E. Salmon, R. Ackermann, J. Wolf, L. Bergé, and S. Skupin: *UV–Supercontinuum generated by femtosecond pulse filamentation in air: Meter-range experiments versus numerical simulations*. Applied Physics B: Lasers and Optics **82**, 3 (2006), pp. 341–345.

[Mia03]   J. Miao, T. Ishikawa, E. H. Anderson, and K. O. Hodgson: *Phase retrieval of diffraction patterns from noncrystalline samples using the oversampling method*. Phys. Rev. B **67** (2003), p. 174104.

[Mia98]   J. Miao, D. Sayre, and H. N. Chapman: *Phase retrieval from the magnitude of the Fourier transforms of nonperiodic objects*. J. Opt. Soc. Am. A **15**, 6 (1998), pp. 1662–1669.

[Mia99]   J. Miao, P. Charalambous, J. Kirz, and D. Sayre: *Extending the methodology of X-ray crystallography to allow imaging of micrometre-sized non-crystalline specimens*. Nature **400**, 6742 (1999), pp. 342–344.

[Min08]   S. Minardi, A. Gopal, M. Tatarakis, A. Couairon, G. Tamošauskas, R. Piskarskas, A. Dubietis, and P. D. Trapani: *Time-resolved refractive index and absorption mapping of light-plasma filaments in water*. Opt. Lett. **33**, 1 (2008), pp. 86–88.

[Min09]   S. Minardi, A. Gopal, A. Couairon, G. Tamoašuskas, R. Piskarskas, A. Dubietis, and P. D. Trapani: *Accurate retrieval of pulse-splitting dynamics of a femtosecond filament in water by time-resolved shadowgraphy*. Opt. Lett. **34**, 19 (2009), pp. 3020–3022.

[Mle98]   M. Mlejnek, E. Wright, and J. Moloney: *Dynamic spatial replenishment of fem-
           tosecond pulses propagating in air*. Opt. Lett. **23**, 5 (1998), pp. 382–384.

[Mys08]   A. Mysyrowicz, A. Couairon, and U. Keller: *Self-compression of optical laser pulses
           by filamentation*. New Journal of Physics **10**, 2 (2008), p. 025023.

[Neu00]   R. Neutze, R. Wouts, D. van der Spoel, E. Weckert, and J. Hajdu: *Potential for
           biomolecular imaging with femtosecond X-ray pulses*. Nature **406**, 6797 (2000),
           pp. 752–757.

[Nib96]   E. Nibbering, P. Curley, G. Grillon, B. Prade, M. Franco, F. Salin, and A. Mysy-
           rowicz: *Conical emission from self-guided femtosecond pulses in air*. Opt. Lett. **21**,
           1 (1996), pp. 62–65.

[Nib97]   E. T. J. Nibbering, G. Grillon, M. A. Franco, B. S. Prade, and A. Mysyrowicz:
           *Determination of the inertial contribution to the nonlinear refractive index of air,
           N2, and O2 by use of unfocused high-intensity femtosecond laser pulses*. J. Opt.
           Soc. Am. B **14**, 3 (1997), pp. 650–660.

[Odh10]   J. H. Odhner, D. A. Romanov, and R. J. Levis: *Self-Shortening Dynamics Mea-
           sured along a Femtosecond Laser Filament in Air*. Phys. Rev. Lett. **105** (2010),
           p. 125001.

[Odh12]   J. Odhner and R. J. Levis: *Direct Phase and Amplitude Characterization of
           Femtosecond Laser Pulses Undergoing Filamentation in Air*. Opt. Lett. **accepted**
           (2012),

[Pap01]   N. Papadogiannis, C. Kalpouzos, E. Goulielmakis, G. Nersisyan, D. Charalambidis,
           F. Augé, F. Weihe, and P. Balcou: *Kilohertz extreme-ultraviolet light source based
           on femtosecond high-order harmonic generation from noble gases*. Applied Physics
           B: Lasers and Optics **73** (2001), pp. 687–692.

[Pap08]   D. G. Papazoglou and S. Tzortzakis: *In-line holography for the characterization of
           ultrafast laser filamentation in transparent media*. Appl. Phys. Lett. **93**, 4 (2008),
           p. 041120.

[Pap99]   N. A. Papadogiannis, B. Witzel, C. Kalpouzos, and D. Charalambidis: *Observation
           of Attosecond Light Localization in Higher Order Harmonic Generation*. Phys. Rev.
           Lett. **83** (1999), pp. 4289–4292.

[Pau01]   P. Paul, E. Toma, P. Breger, G. Mullot, F. Augé, P. Balcou, H. Muller, and P. Agostini:
           Observation of a train of attosecond pulses from high harmonic generation. Science
           292, 5522 (2001), p. 1689.

[Pea98]   J. Peatross, S. Backus, J. Zhou, M. M. Murnane, and H. C. Kapteyn: *Spectral-
           spatial measurements of fundamental and third-harmonic light of intense 25-fs
           laser pulses focused in a gas cell*. J. Opt. Soc. Am. B **15**, 1 (1998), pp. 186–192.

[Per66]   A. M. Perelomov, V. S. Popov, and M. V. Terent'ev: *Ionization of Atoms in an
           Alternating Electric Field*. Sov. Phys. JETP **23** (1966), p. 924.

[Per67]   A. M. Perelomov, V. S. Popov, and M. V. Terent'ev: *Ionization of Atoms in an
           Alternating Electric Field: II*. Sov. Phys. JETP **24** (1967), p. 207.

[Pop08]   S. V. Popruzhenko, V. D. Mur, V. S. Popov, and D. Bauer: *Strong Field Ionization Rate for Arbitrary Laser Frequencies*. Phys. Rev. Lett. **101** (2008), p. 193003.

[Pre96]   S. G. Preston, A. Sanpera, M. Zepf, W. J. Blyth, C. G. Smith, J. S. Wark, M. H. Key, K. Burnett, M. Nakai, D. Neely, and A. A. Offenberger: *High-order harmonics of 248.6-nm KrF laser from helium and neon ions*. Phys. Rev. A **53** (1996), R31–R34.

[Pro97]   M. Protopapas, C. H. Keitel, and P. L. Knight: *Atomic physics with super-high intensity lasers*. Reports on Progress in Physics **60**, 4 (1997), p. 389.

[Rai00]   P. Rairoux, H. Schillinger, S. Niedermeier, M. Rodriguez, F. Ronneberger, R. Sauerbrey, B. Stein, D. Waite, C. Wedekind, H. Wille, L. Wöste, and C. Ziener: *Remote sensing of the atmosphere using ultrashort laser pulses*. Applied Physics B: Lasers and Optics **71** (2000), pp. 573–580.

[Rai10]   K. S. Raines, S. Salha, R. L. Sandberg, H. Jiang, J. A. Rodriguez, Fahimian, B. P., H. C. Kapteyn, J. Du, and J. Miao: *Three-dimensional structure determination from a single view*. Nature **463**, 7278 (2010), pp. 214–217.

[Rav09]   A. Ravasio, D. Gauthier, F. R. N. C. Maia, M. Billon, J.-P. Caumes, D. Garzella, M. Géléoc, O. Gobert, J.-F. Hergott, A.-M. Pena, H. Perez, B. Carré, E. Bourhis, J. Gierak, A. Madouri, D. Mailly, B. Schiedt, M. Fajardo, J. Gautier, P. Zeitoun, P. H. Bucksbaum, J. Hajdu, and H. Merdji: *Single-Shot Diffractive Imaging with a Table-Top Femtosecond Soft X-Ray Laser-Harmonics Source*. Phys. Rev. Lett. **103** (2009), p. 028104.

[Rei10]   F. Reiter, U. Graf, M. Schultze, W. Schweinberger, H. Schröder, N. Karpowicz, A. M. Azzeer, R. Kienberger, F. Krausz, and E. Goulielmakis: *Generation of sub-3 fs pulses in the deep ultraviolet*. Opt. Lett. **35**, 13 (2010), pp. 2248–2250.

[Rob06]   J. S. Robinson: *The generation and application of intense, few-cycle laser pulses*. PhD thesis. Prince Consort Road, London, UK: Quantum Optics and Laser Science Group, Imperial College, 2006.

[Rod04]   M. Rodriguez, R. Bourayou, G. Méjean, J. Kasparian, J. Yu, E. Salmon, A. Scholz, B. Stecklum, J. Eislöffel, U. Laux, et al.: *Kilometer-range nonlinear propagation of femtosecond laser pulses*. Physical Review E **69**, 3 (2004), p. 036607.

[San06]   G. Sansone, E. Benedetti, F. Calegari, C. Vozzi, L. Avaldi, R. Flammini, L. Poletto, P. Villoresi, C. Altucci, R. Velotta, S. Stagira, S. De Silvestri, and M. Nisoli: *Isolated Single-Cycle Attosecond Pulses*. Science **314**, 5798 (2006), pp. 443–446.

[San07]   R. L. Sandberg, A. Paul, D. A. Raymondson, S. Hädrich, D. M. Gaudiosi, J. Holtsnider, R. I. Tobey, O. Cohen, M. M. Murnane, H. C. Kapteyn, C. Song, J. Miao, Y. Liu, and F. Salmassi: *Lensless Diffractive Imaging Using Tabletop Coherent High-Harmonic Soft-X-Ray Beams*. Phys. Rev. Lett. **99** (2007), p. 098103.

[San08]   R. L. Sandberg, C. Song, P. W. Wachulak, D. A. Raymondson, A. Paul, B. Amir-
           bekian, E. Lee, A. E. Sakdinawat, C. La-O-Vorakiat, M. C. Marconi, C. S. Menoni,
           M. M. Murnane, J. J. Rocca, H. C. Kapteyn, and J. Miao: *High numerical aperture
           tabletop soft x-ray diffraction microscopy with 70-nm resolution*. Proceedings of
           the National Academy of Sciences **105**, 1 (2008), pp. 24–27.

[Sch11a]   E. Schulz, D. S. Steingrube, T. Binhammer, M. B. Gaarde, A. Couairon, U.
           Morgner, and M. Kovačev: *Tracking spectral shapes and temporal dynamics along
           a femtosecond filament*. Opt. Express **19**, 20 (2011), pp. 19495–19507.

[Sch11d]   E. Schulz, D. S. Steingrube, T. Vockerodt, T. Binhammer, U. Morgner, and M.
           Kovačev: *Gradient enhanced third harmonic generation in a femtosecond filament*.
           Opt. Lett. **36**, 22 (2011), pp. 4389–4391.

[Sig71]   G. Sigel Jr.: *Vacuum ultraviolet absorption in alkali doped fused silica and silicate
           glasses*. Journal of Physics and Chemistry of Solids **32**, 10 (1971), pp. 2373
           –2383.

[Sku06]   S. Skupin, G. Stibenz, L. Bergé, F. Lederer, T. Sokollik, M. Schnürer, N. Zha-
           voronkov, and G. Steinmeyer: *Self-compression by femtosecond pulse filamenta-
           tion: Experiments versus numerical simulations*. Phys. Rev. E **74** (2006), p. 056604.

[Spi97]   C. Spielmann, N. Burnett, S. Sartania, R. Koppitsch, M. Schnürer, C. Kan, M.
           Lenzner, P. Wobrauschek, and F. Krausz: *Generation of coherent X-rays in the
           water window using 5-femtosecond laser pulses*. Science **278**, 5338 (1997), p. 661.

[Ste04]   K. Stelmaszczyk, P. Rohwetter, G. Méjean, J. Yu, E. Salmon, J. Kasparian, R.
           Ackermann, J. Wolf, and L. Woste: *Long-distance remote laser-induced breakdown
           spectroscopy using filamentation in air*. Appl. Phys. Lett. **85**, 18 (2004), pp. 3977–
           3979.

[Ste09a]   D. S. Steingrube, E. Schulz, T. Binhammer, T. Vockerodt, U. Morgner, and
           M. Kovačev: *Generation of high-order harmonics with ultra-short pulses from
           filamentation*. Opt. Express **17**, 18 (2009), pp. 16177–16182.

[Ste09c]   D. S. Steingrube, T. Vockerodt, E. Schulz, U. Morgner, and M. Kovačev: *Phase
           matching of high-order harmonics in a semi-infinite gas cell*. Phys. Rev. A **80**
           (2009), p. 043819.

[Ste11a]   D. S. Steingrube: *High-order harmonic generation with ultra-short pulses from
           filamentation*. PhD thesis. Welfengarten 1, 30167 Hannover, Germany: Leibniz
           Universität Hannover, Faculty of Mathematics and Physics, Institute of Quantum
           Optics, 2011.

[Ste11b]   D. S. Steingrube, E. Schulz, T. Binhammer, M. B. Gaarde, A. Couairon, U.
           Morgner, and M. Kovačev: *High-order harmonic generation directly from a fila-
           ment*. New Journal of Physics **13**, 4 (2011), p. 043022.

[Sti06]   G. Stibenz, N. Zhavoronkov, and G. Steinmeyer: *Self-compression of millijoule
           pulses to 7.8 fs duration in a white-light filament*. Opt. Lett. **31**, 2 (2006), pp. 274–
           276.

[Suc08]   H. Suchowski, D. Oron, A. Arie, and Y. Silberberg: *Geometrical representation of sum frequency generation and adiabatic frequency conversion*. Phys. Rev. A **78** (2008), p. 063821.

[Suc09]   H. Suchowski, V. Prabhudesai, D. Oron, A. Arie, and Y. Silberberg: *Robust adiabatic sum frequency conversion*. Opt. Express **17**, 15 (2009), pp. 12731–12740.

[Sun09]   S. Suntsov, D. Abdollahpour, D. G. Papazoglou, and S. Tzortzakis: *Efficient third-harmonic generation through tailored IR femtosecond laser pulse filamentation in air*. Opt. Express **17**, 5 (2009), pp. 3190–3195.

[Sun10]   S. Suntsov, D. Abdollahpour, D. G. Papazoglou, and S. Tzortzakis: *Filamentation-induced third-harmonic generation in air via plasma-enhanced third-order susceptibility*. Phys. Rev. A **81**, 3 (2010), p. 033817.

[Thé05a]   F. Théberge, N. Aközbek, W. Liu, J.-F. Gravel, and S. Chin: *Third harmonic beam profile generated in atmospheric air using femtosecond laser pulses*. Optics Communications **245**, 1-6 (2005), pp. 399 –405.

[Thé05b]   F. Théberge, W. Liu, Q. Luo, and S. Chin: *Ultrabroadband continuum generated in air (down to 230 nm) using ultrashort and intense laser pulses*. Applied Physics B: Lasers and Optics **80** (2005), pp. 221–225.

[Thé07a]   F. Théberge, N. Aközbek, W. Liu, J. Filion, and S. Chin: *Conical emission and induced frequency shift of third-harmonic generation during ultrashort laser filamentation in air*. Optics Communications **276**, 2 (2007), pp. 298 –304.

[Thé07b]   F. Théberge, J. Filion, N. Aközbek, Y. Chen, A. Becker, and S. Chin: *Self-stabilization of third-harmonic pulse during two-color filamentation in gases*. Applied Physics B: Lasers and Optics **87** (2007), pp. 207–210.

[Trä07]   F. Träger: *Springer handbook of lasers and optics*. Springer Verlag, 2007.

[Tre00]   R. Trebino: *Frequency-Resolved Optical Gating: The Measurement of Ultrashort Laser Pulses*. Kluwer Academic, 2000.

[Ury10]   D. Uryupina, M. Kurilova, A. Mazhorova, N. Panov, R. Volkov, S. Gorgutsa, O. Kosareva, A. Savel'ev, and S. L. Chin: *Few-cycle optical pulse production from collimated femtosecond laser beam filamentation*. J. Opt. Soc. Am. B **27**, 4 (2010), pp. 667–674.

[Voc12c]   T. Vockerodt, D. S. Steingrube, E. Schulz, M. Kretschmar, U. Morgner, and M. Kovačev: *Low- and high-order harmonic generation inside an air filament*. Appl. Phys. B **106**, 3 (2012), pp. 529–532.

[Wan11]   G. Wang, H. Yu, W. Cong, and A. Katsevich: *Non-uniqueness and instability of 'ankylography'*. Nature **480** (2011), p. 7375.

[War69]   J. F. Ward and G. H. C. New: *Optical Third Harmonic Generation in Gases by a Focused Laser Beam*. Phys. Rev. **185**, 1 (1969), pp. 57–72.

[Wei11]   H. Wei: *Fundamental limits of 'ankylography' due to dimensional deficiency*. Nature **480** (2011), p. 7375.

[Wös97]   L. Wöste, C. Wedekind, H. Wille, P. Rairoux, B. Stein, S. Nikolov, C. Werner, S. Niedermeier, F. Ronneberger, H. Schillinger, et al.: *Femtosecond atmospheric lamp*. Laser und Optoelektronik **29**, 5 (1997), pp. 51–53.

[Xi09]   T.-T. Xi, X. Lu, and J. Zhang: *Enhancement of third harmonic emission by interaction of two colored filament with droplet in air*. Optics Communications **282**, 15 (2009), pp. 3140 –3143.

[Xu12]   S. Xu, X. Sun, B. Zeng, W. Chu, J. Zhao, W. Liu, Y. Cheng, Z. Xu, and S. L. Chin: *Simple method of measuring laser peak intensity inside femtosecond laser filament in air*. Opt. Express **20**, 1 (2012), pp. 299–307.

[Yan03]   H. Yang, J. Zhang, J. Zhang, L. Z. Zhao, Y. J. Li, H. Teng, Y. T. Li, Z. H. Wang, Z. L. Chen, Z. Y. Wei, J. X. Ma, W. Yu, and Z. M. Sheng: *Third-order harmonic generation by self-guided femtosecond pulses in air*. Phys. Rev. E **67** (2003), p. 015401.

[Yan09]   X. Yang, J. Wu, Y. Peng, Y. Tong, S. Yuan, L. Ding, Z. Xu, and H. Zeng: *Noncollinear interaction of femtosecond filaments with enhanced third harmonic generation in air*. Appl. Phys. Lett. **95**, 11 (2009), p. 111103.

[Yud01]   G. L. Yudin and M. Y. Ivanov: *Nonadiabatic tunnel ionization: Looking inside a laser cycle*. Phys. Rev. A **64** (2001), p. 013409.

[Zha10]   Z. Zhang, X. Lu, Y. Zhang, M. Zhou, T. Xi, Z. Wang, and J. Zhang: *Enhancement of third-harmonic emission from femtosecond laser filament screened partially by a thin fiber*. Opt. Lett. **35**, 7 (2010), pp. 974–976.

List of Figures

List of Tables

A

Theory of Non-linear Ionisation

A.1 Keldysh Theory

A well known theory of photo-ionisation in strong fields is the general KELDYSH theory [Kel65]. Given that the tunnelling time τ of an electron through the barrier of a coulomb potential is small compared to the changing of the electric field, the tunnel effect is determined by the instantaneous electric field value. This statement holds for frequencies $\omega_t = \tau^{-1}$ on the order of

$$\omega_t = \frac{e \cdot E}{\sqrt{2m_e \ell}} , \qquad (A.1)$$

where e denotes the elementary charge, E the electric field strength, m_e the electron mass, $\ell = I_P/eE$ the barrier width and I_P the atomic ionisation potential.

KELDYSH introduces an adiabaticity parameter γ, called the KELDYSH parameter, which is the ratio of the electric field oscillation period to the electron tunnelling time. It has a major relevance in calculation of the ionisation rate and is defined as

$$\gamma = \frac{\omega}{\omega_t} = \omega \cdot \frac{\sqrt{2m_e I_P}}{e \cdot E} = \sqrt{\frac{I_P}{2U_P}} , \qquad (A.2)$$

where ω is the electric field frequency and U_P is the *ponderomotive potential*, which is the average kinetic energy of a free electron in an alternating electric field:

$$U_P = \frac{1}{2} \frac{e^2}{m_e \omega^2} \left\langle E^2(t) \right\rangle \qquad (A.3)$$

Here, brackets indicate the time average for one oscillation period. The ionisation rate w is

then expressed as

$$
w = A\omega \cdot \left(\frac{I_{\mathrm{P}}}{\hbar\omega}\right)^{3/2} \cdot \left(\frac{\gamma}{\sqrt{1+\gamma^2}}\right)^{5/2} S\left(\gamma, \frac{I_\omega}{\hbar\omega}\right)
$$
$$
\cdot \exp\left(-\frac{2I_\omega}{\hbar\omega}\left(\operatorname{arsinh}(\gamma) - \gamma \cdot \frac{\sqrt{1+\gamma^2}}{1+2\gamma^2}\right)\right). \quad \text{(A.4)}
$$

A is a numerical coefficient of the order of unity. $I_\omega = I_{\mathrm{P}}\left(1 + 1/\left(2\gamma^2\right)\right)$ is the effective ionisation potential at a field oscillation frequency ω.

Using $\operatorname{int}(x)$ to denote the integer part of the value x, the function $S\left(\gamma, I_\omega/\hbar\omega\right)$ describes the spectrum's structure connected with the discreteness of the number of absorbed photons:

$$
S(\gamma, x) = \sum_{n=0}^{\infty} \exp\left[-2\left(\operatorname{int}(x+1) - x + n\right) \cdot \left(\operatorname{arsinh}(\gamma) - \gamma\left(1+\gamma^2\right)^{-1/2}\right)\right.
$$
$$
\left. \cdot \Phi\left(\left(2\gamma\left(1+\gamma^2\right)^{-1/2}\left(\operatorname{int}(x+1) - x + n\right)\right)^{1/2}\right)\right] \quad \text{(A.5)}
$$

Here, the probability function $\Phi(z)$ is the *Dawson integral*:

$$
\Phi(z) = \int_0^{\infty} \mathrm{e}^{y^2 - z^2}\, \mathrm{d}y \quad\quad\quad\quad\quad\quad\quad\quad\quad\quad\quad \text{(A.6)}
$$

In the general KELDYSH theory, details of the atomic species are incorporated in the numerical factor A in equation (A.4), which often serves as a fitting parameter. To account for the long range Coulomb interaction between the released electron and the ion, KELDYSH used a 'quasi-classical analysis' not further detailed in [Kel65]. For a high field strength at low frequencies, $\gamma \ll 1$, the KELDYSH formula changes over to pure tunnel ionisation. The high frequency limit with a low field strength, $\gamma \gg 1$, yields a description of multi-photon absorption. Thus, the KELDYSH parameter is often used to discriminate between dominating ionisation channels. Such an interpretation needs to be tested carefully, as the physical process in both cases is essentially the same, and typical properties for experiments, e.g. high-order harmonic generation, often lead to values for γ in the order of one.

A.2　PPT Theory

PERELOMOV, POPOV and TERENT'EV (PPT) improved the general KELDYSH theory by taking atomic details [Per66] and Coulomb interaction [Per67] into account. To begin with, the ionisation probability w_{SR} for a short range Coulomb interaction alone is calculated. For a

bound state with quantum numbers n, ℓ and m, it is

$$w_{\mathrm{SR}}(E,\omega) = \frac{I_{\mathrm{P}}}{\hbar}\left|C_{n^*,\ell^*}\right|^2\sqrt{\frac{6}{\pi}} \cdot f(\ell,m)\left(\frac{E}{2E_0}\sqrt{1+\gamma^2}\right)^{|m|+3/2}$$

$$\cdot A_m(\omega,\gamma) \cdot \exp\left(-\frac{2E_0}{3E} \cdot g(\gamma)\right), \quad (\text{A.7})$$

with effective quantum numbers n^*, ℓ^*, coefficients C_{n^*,ℓ^*} and the following notations:

$$f(\ell,m) = \frac{(2\ell+1)(\ell+|m|)!}{2^{|m|}|m|!(\ell-|m|)!} \quad (\text{A.8})$$

$$A_m(\omega,\gamma) = \frac{4}{\sqrt{3\pi}}\frac{1}{|m|!}\frac{\gamma^2}{1+\gamma^2}\sum_{n\geq v}\exp(-\alpha(n-v))w_m\left(\sqrt{\beta(n-v)}\right) \quad (\text{A.9})$$

$$w_m(x) = e^{-x^2}\int_0^x e^{y^2}\left(x^2-y^2\right)^{|m|}\,\mathrm{d}y \quad (\text{A.10})$$

$$v = \frac{I_{\mathrm{P}}}{\hbar\omega}\left(1+\frac{1}{2\gamma^2}\right) \quad (\text{A.11})$$

$$g(\gamma) = \frac{3}{2\gamma}\left[\left(1+\frac{1}{2\gamma^2}\right)\cdot\operatorname{arsinh}(\gamma)-\frac{\sqrt{1+\gamma^2}}{2\gamma}\right] \quad (\text{A.12})$$

The parameters α and β are functions of the KELDYSH parameter (see equation (A.2)) and, therefore, depend on the frequency ω and the field strength E.

$$\alpha(\gamma) = 2\left(\operatorname{arsinh}(\gamma)-\frac{\gamma}{\sqrt{1+\gamma^2}}\right) \quad (\text{A.13})$$

$$\beta(\gamma) = \frac{2\gamma}{\sqrt{1+\gamma^2}} \quad (\text{A.14})$$

Taking long-ranged Coulomb interaction in equation (A.7) into account leads to an additional factor [Per67]:

$$w_{\mathrm{PPT}}(E,\omega) = \left(\frac{2E_0}{E}\right)^{2n^*}\cdot w_{\mathrm{SR}}(E,\omega) \quad (\text{A.15})$$

By including (A.7) into (A.15), the overall ionisation rate according to the PPT theory is

written as follows:

$$w_{\mathrm{PPT}}(E,\omega) = \frac{I_{\mathrm{P}}}{\hbar}\left|C_{n^*,\ell^*}\right|^2\sqrt{\frac{6}{\pi}}\cdot f(\ell,m)\left(1+\gamma^2\right)^{n^*}\left(\frac{2E_0}{E}\sqrt{1+\gamma^2}\right)^{2n^*-|m|-3/2}$$
$$\cdot A_m(\omega,\gamma)\cdot\exp\left(-\frac{2E_0}{3E}\cdot g(\gamma)\right) \qquad \text{(A.16)}$$

Ionisation rates calculated numerically by equation (A.16) show a very good agreement with experimental data [Lar98].

A.3 ADK Theory

In contrast to KELDYSH and PPT theories, the approach developed by AMMOSOV, DELONE and KRAINOV (ADK) [Amm86] concentrates on tunnel ionisation of a complex atom in an arbitrary state. An explicit form of the coefficient $C_{n^*\ell^*}$ is given, therefore eliminating the remaining free parameter from the expressions of photo-ionisation.

$$C_{n^*\ell^*}^2 = \frac{2^{2n^*}}{n^*\cdot\Gamma(n^*+\ell^*+1)\cdot\Gamma(n^*-\ell^*)} \approx \frac{1}{2\pi n^*}\left(\frac{4\exp(2)}{n^{*2}}-\ell^{*2}\right)^{n^*}\left(\frac{n^*-\ell^*}{n^*+\ell^*}\right)^{\ell^*+1/2} \quad \text{(A.17)}$$

Here, $\Gamma(x)$ is the Euler gamma function and n^*, $\ell^* = n_0^* - 1$ are the effective values of the principal and orbital quantum numbers (for details see equation (5) in ref. [Per66]),

$$n^* = Z\left(I_{\mathrm{P}}/I_{0H}\right)^{-1/2} = \frac{e^2\sqrt{m_e}}{4\pi\varepsilon_0\hbar}\cdot\frac{Z}{\sqrt{2I_{\mathrm{P}}}}, \qquad \text{(A.18)}$$

where Z is the charge number of the residual ion and n_0^* denotes the principal quantum number of the ground state. Considering the special case of tunnel ionisation ($\gamma \ll 1$) the ionisation rate simplifies to

$$w_{\mathrm{ADK}}(E) = \frac{I_{\mathrm{P}}}{\hbar}\left|C_{n^*\ell^*}\right|^2\sqrt{\frac{6}{\pi}}f(\ell,m)\left(\frac{2E_0}{E}\right)^{2n^*-|m|-3/2}\exp\left(-\frac{2E_0}{3E}\right), \qquad \text{(A.19)}$$

which is easily calculated numerically.

Curriculum Vitae

Personal details

Name   Tobias Vockerodt
                        born October 14th, 1982 in Hannover, Germany
                        unmarried, German

Education

12/2008 - 7/2012   Grant of a PhD-fellowship in the programme *Excellence in QUEST*

11/2008   Diploma thesis, *Generation of high-harmonic radiation in rare gas mixtures*
                        Ultrafast Laser Optics group, Prof. Dr. U. Morgner
                        Institute of Quantum Optics, Leibniz Universität Hannover
                        overall grade: with distinction (*mit Auszeichnung*)

9/2003 - 11/2008   Leibniz Universität Hannover
                        Studies in technical physics, major subject 'optics and photonics'

2002 - 2003   Civilian service at Heidekreis-Klinikum Walsrode
                        medical engineering

1995 - 2002   Gymnasium Walsrode
                        Abitur

Professional experience

5/2006 - 9/2007   Solid State Photonics Group, Laser Zentrum Hannover
                        Development of a high power continuous wave laser for next generation
                        gravitational wave detectors

7/2006 - 10/2006   Industrial placement at LINOS Photonics GmbH & Co. KG
                        Research and development department

10/2005 - present   Institute of Quantum Optics, Leibniz Universität Hannover
                        Teaching assistant at the physics beginners' practical laboratory
                        Supervision of first and second year students

7/2005 - 10/2005   Institute of Quantum Optics, Leibniz Universität Hannover
                        Design and maintenance of experiments for the physics beginners'
                        practical laboratory

10/2004 - 2/2005	Institut für Simulation und Modelierung, Leibniz Universität Hannover Teaching assistant at the *Programming 1* lecture Supervision of first year students

Awards

2011	*Best Poster Award* at the SASQC11 Symposium on Attosecond Science and Quantum Control, awarded for organisation, presentation and scientific relevance of the presented poster
2002	Fellowship in the Deutsche Physikalische Gesellschaft, awarded for excellent achievements in the school subject physics

Activities

2010	Expert certificate as laser protection designate
2008 - 2010	Institute of Quantum Optics, Leibniz Universität Hannover Collegiate member of the board of directors
2008	Foundation of the Hannover regional group of the German Physical Society's young division (jDPG)
2006 - 2008	Weihnachtsvorlesung Department of Physics, Leibniz Universität Hannover Collegiate organised physics show for the general public Design and build-up of experiments, presentation of the show in 2008

Publications

The following publications have resulted from work I have been involved in.

Scientific publications

[Sch11b]   E. Schulz, D. S. Steingrube, T. Vockerodt, T. Binhammer, U. Morgner, and M. Kovačev: *Efficient on-axis third harmonic generation in a light filament*. CLEO/Europe and EQEC 2011 Conference. Optical Society of America, 2011, CG2_4.

[Sch11d]   E. Schulz, D. S. Steingrube, T. Vockerodt, T. Binhammer, U. Morgner, and M. Kovačev: *Gradient enhanced third harmonic generation in a femtosecond filament*. Opt. Lett. **36**, 22 (2011), pp. 4389–4391.

[Ste09a]   D. S. Steingrube, E. Schulz, T. Binhammer, T. Vockerodt, U. Morgner, and M. Kovačev: *Generation of high-order harmonics with ultra-short pulses from filamentation*. Opt. Express **17**, 18 (2009), pp. 16177–16182.

[Ste09b]   D. S. Steingrube, T. Vockerodt, U. Morgner, and M. Kovačev: *Phase-matching high-order harmonics in a semi-infinite gas cell geometry*. CLEO/Europe and EQEC 2009 Conference Digest. Optical Society of America, 2009, CG_P11.

[Ste09c]   D. S. Steingrube, T. Vockerodt, E. Schulz, U. Morgner, and M. Kovačev: *Phase matching of high-order harmonics in a semi-infinite gas cell*. Phys. Rev. A **80** (2009), p. 043819.

[Ste10a]   D. S. Steingrube, E. Schulz, T. Binhammer, T. Vockerodt, U. Morgner, and M. Kovačev: *High-Order Harmonic Generation by Few-Cycle Pulses from Filamentation*. International Conference on Ultrafast Phenomena, OSA Technical Digest (CD). Optical Society of America, 2010, ThE26.

[Voc12c]   T. Vockerodt, D. S. Steingrube, E. Schulz, M. Kretschmar, U. Morgner, and M. Kovačev: *Low- and high-order harmonic generation inside an air filament*. Appl. Phys. B **106**, 3 (2012), pp. 529–532.

Contributions to international conferences

[Sch09]   E. Schulz, D. Steingrube, T. Binhammer, T. Vockerodt, U. Morgner, and M. Kovačev: *Generation of high-order harmonics with ultra-short pulses from filamentation*. International Conference on Attosecond Physics (ATTO2). Kansas, USA, 2009.

[Sch11c] E. Schulz, D. S. Steingrube, T. Vockerodt, T. Binhammer, U. Morgner, and M. Kovačev: *Efficient on-axis third harmonic generation in a light filament*. CLEO/Europe and EQEC 2011 Conference. Optical Society of America, 2011, CG2_4.

[Ste09d] D. S. Steingrube, T. Vockerodt, U. Morgner, and M. Kovačev: *Phase-matching high-order harmonics in a semi-infinite gas cell geometry*. CLEO/Europe and EQEC 2009 Conference. Optical Society of America, 2009, CG_P11.

[Ste10b] D. S. Steingrube, E. Schulz, T. Binhammer, T. Vockerodt, U. Morgner, and M. Kovačev: *High-Order Harmonic Generation by Few-Cycle Pulses from Filamentation*. International Conference on Ultrafast Phenomena (UP10). Optical Society of America, 2010, ThE26.

[Voc11a] T. Vockerodt, D. S. Steingrube, E. Schulz, M. Kretschmar, U. Morgner, and M. Kovačev: *Ultra broadband UV generation from femtosecond filamentation*. International Conference on Attosecond Physics (ATTO3). 2011.

[Voc11b] T. Vockerodt, D. S. Steingrube, E. Schulz, M. Kretschmar, U. Morgner, and M. Kovačev: *Ultra broadband UV generation from femtosecond filamentation*. ATTOFEL Summer School, Greece. 2011.

[Voc12a] T. Vockerodt, M. Kretschmar, E. Schulz, D. S. Steingrube, T. Nagy, U. Morgner, and M. Kovačev: *Broadband UV Generation and High-order Harmonics inside a Femtosecond Filament*. 4th International Symposium on Filamentation (COFIL). 2012.

[Voc12b] T. Vockerodt, D. Steingrube, E. Schulz, M. Kretschmar, U. Morgner, and M. Kovacev: *Low- and high-order harmonic generation inside an air filament*. High-Intensity Lasers and High-Field Phenomena (HILAS). Optical Society of America, 2012, HM3C.6.

Acknowledgement

The offices of *Institut für Quantenoptik* and QUEST, namely Elke Hünitzsch, Birgit Ohlendorf and Barbara Thiele-Bode, who really know how to run a scientific institute.

The IQO's precision mechanics workshop, who always found a way to produce mechanical parts precise and – even in busy times – incredibly fast.

My family, who provided support, the lectorate, enjoyment and distraction.

My love, Chris. Thank you.